Combining electronic and nuclear structures of gas-phase species: theoretical and experimental approaches to understanding novel materials

Eleanor Michi Burrow

Doctor of Philosophy

University of York

Department of Chemistry

December 2023

Abstract

Gas-phase multiphoton spectroscopy has been used in conjunction with theoretical calculations to examine the geometry changes that occur in two molecules, anethole and benzocaine, upon excitation to their S_1 electronic state, and then once more upon the removal of an electron. Anethole was found to have two rotational conformers, *anti* and *syn*, differentiated by the relative direction the para-substituted ring substituents faced. The *syn* conformer was found to change geometry more substantially upon excitation than did the *anti* conformer, and this was interpreted using the RICC2 calculated electronic configuration. Ionisation energies of 60615 cm^{-1} and 60624 cm^{-1} were found for the *syn* and *anti* conformers, respectively.

The complexation of anethole with argon was further investigated, showing the stabilising effect the argon atom has on the cation, seen in a lowering of ionisation energy by 69 cm^{-1} for the *syn* conformer and 58 cm^{-1} for the *anti*. The argon atom was found to attach to anethole in a π-bonding arrangement above the ring, and binding energy was found to increase upon excitation, and then again upon ionisation.

Benzocaine was shown to undergo a dramatic geometry change upon excitation to the S_1 state. Significant distortion along the NH_2 inversion coordinate was found, but an exact geometry of the excited state remains elusive. ZEKE spectra measured from multiple intermediate S_1 vibronic states showed complex vibrational structure. Of particular interest is one spectrum showed a splitting of peaks due to quantum tunnelling of the hydrogen atoms through the NH_2 inversion coordinate. Elsewhere, many vibrations were significantly shifted in frequency as the electronic configuration changed.

I declare that this thesis is a presentation of original work and that I am the sole author, with the exception of the work performed by Dr Cate Anstöter, detailed in chapter four and reported here with her permission as part of a collaborative effort. This work has not previously been presented for a degree or other qualification at this University or elsewhere. All sources are acknowledged as references.

Acknowledgements

I first must thank my supervisor, Martin, for his years of patience, encouragement and advice whilst I was his student. I thank him sincerely for the introduction he gave me to the wonderful world of gas spectroscopy, and apologise for just how long it took me to finally finish this project! I had the time of my life working away in the lab, please give the experiment the occasional hug from me.

Next, I would thank the many, many members of the Physchem group at York who have made my time here the joy it has been. There are too many to name from the six years I have sat at the corner desk, but through the turbulence of a pandemic, the joys of Friday cake sessions and the frustrations of all the times experiments go wrong, it's always been wonderful to have these people to talk to. A special mention goes to Cate, for the advice on computational chemistry, and the talks on everything else.

I will always owe this thesis to the support of my partner, Callam, who has encouraged me every step of the way, and (almost) never complained about taking on all the responsibilities that come with family life when I was stuck in the throes of writing. Thank you for all the coffees, I promise I'll be more fun to be around from now on.

Finally, I thank my daughter, who has taught me to never, ever, stop asking the question "why?" as only a two year old could. Tilda, you make me want to learn the answers to all of your questions, this thesis is for you.

"You step onto the road, and if you don't keep your feet, there is no knowing where you might be swept off to." **— J.R.R. Tolkien**

Contents

List of Tables

List of Figures

Chapter 1. Introduction

1.1 Background

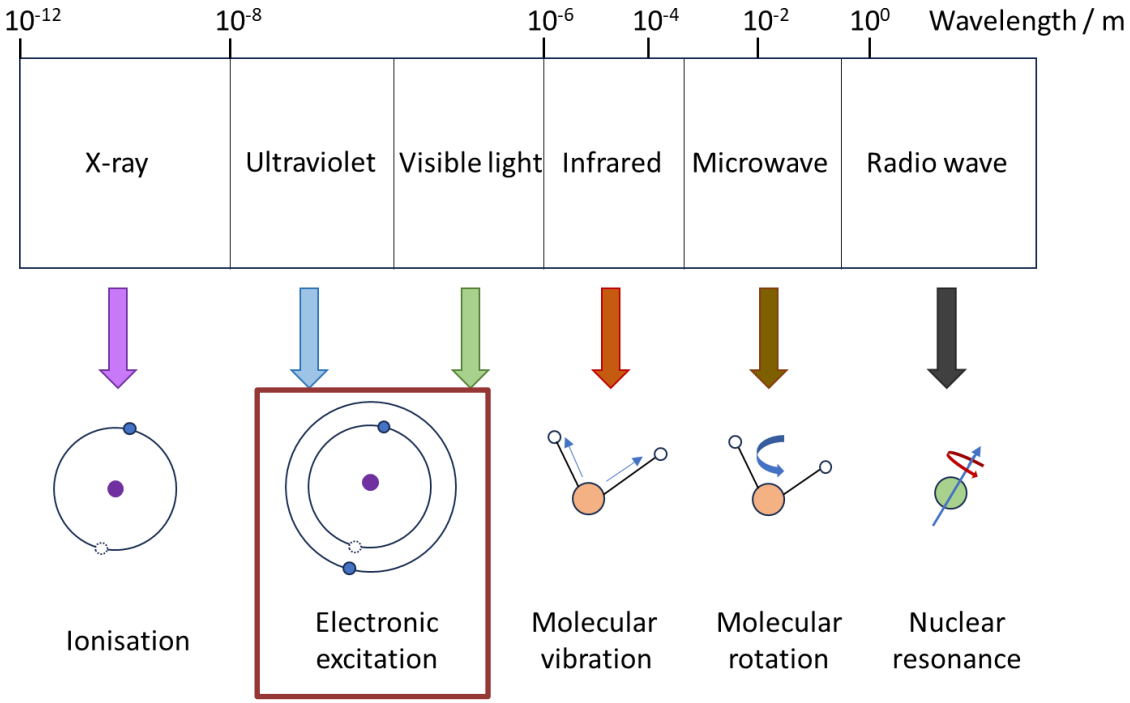

Figure 1-1: The electromagnetic spectrum and its interaction with matter.

1.1.1 Light

Spectroscopy gives information about the interaction of electromagnetic radiation with matter. Figure 1-1 shows how choice of the energy of light being introduced, or measured being expelled, provides results on different ranges of states: lower energy radiation, such as that in the infrared range, corresponds to the energy changes of vibrations, whereas, in the study of electronic transitions, ultraviolet (UV) light is often a more complementary choice. To better understand the large energy change processes that occur in excitation or removal of a core electron, X-rays might be the most appropriate energy range - these are very loose approximations, but they illustrate the different energies with which varieties of transitions may occur. This work will focus on the absorption of photons in the UV range. A range corresponding to the energy gaps between the ground and first excited states of many aromatic molecules.[1] This is a critical range of electromagnetic radiation to study, because it comes from the sun in vast quantities, making up 3-5% of the electromagnetic radiation that reaches the surface of the planet, and interacts with

molecules on Earth.[2] Understanding how natural products, amongst others, react to this radiation is very important.[3]

Classical ideas of dynamic properties allow a continuous increase of energy, whereby a particular state can lie in any region. This has been overruled for the most part by the advent of quantum theory, which shows that states can only be found at discrete intervals, with the energies in between these intervals forbidden. The first time this was detected was in the observation of spectral lines coming from the sun.[4] These were first observed in the 19th century, and then rationalised by Neils Bohr in 1913 as part of his model of the atom.[5] The energy values of the spectral lines of hydrogen were then explained through the development of quantum mechanics by Schrödinger and Heisenberg.[6]

This led to the understanding that the energies of electronic, vibrational, rotational and translational states are quantized. To excite or relax from a state, a fixed amount of energy will have to be absorbed or emitted. By measuring the emission (via a laser-induced fluorescence (LIF) detector for instance) or intake (via UV-VIS spectroscopy, or measurement of a photoproduct such as an ion, or photoelectron) of light we can determine the exact energy of light corresponding to the energy levels we are navigating. Of course, there are limitations to this, such as the ambiguity of a laser wavelength, or lifetime broadening of spectral lines due to a fast-decaying state.

Following the monitoring of light absorbed or emitted we can try to understand what effect the absorption of a discrete packet of energy has on a molecule. We can use an input of a fixed amount of energy, a photon of known wavelength, to probe the energy gaps between electronic and vibrational states. And here we arrive at the area of laser spectroscopy.

1.1.2 Multiphoton Spectroscopy

The birth of the laser in 1960 gave an opportunity to more deeply study the interaction of light with matter.[7] Intense light of a known wavelength allows probing of the vibrational and electronic states. Koopman's theorem states that the first ionisation energy of an atom or molecule is equivalent to the negative value of the orbital energy of the highest occupied molecular orbital (HOMO). Sequential ionisation energies are equal to the second highest occupied orbital, then the third highest and so on. Photoelectron spectroscopy uses Koopman's theorem to estimate the energy of molecular orbitals, by finding the inverse energy of a photoelectron emitted after stimulation with light. This technique has been very useful in the study of gas phase species.[8] The disadvantage, is that measuring the kinetic energy of an electron can be challenging, which leads to a low resolution spectrum. Additionally, very high energy photons are often needed to ionise a molecule. Finding a laser

capable of producing such high energy photons over the scanning range is somewhat difficult.

An alternative, but related technique, is to divide the total photon energy needed for ionisation into separate absorptions of multiple photons, whose cumulative energy is sufficient to ionise it, whilst being easier to produce from a laser. Several multiphoton absorption techniques exist and in this work we shall use two: resonance enhanced multiphoton ionisation spectroscopy (REMPI) and zero energy kinetic electron (ZEKE) spectroscopy. These techniques give (ro)vibrationally resolved spectra of the excited neutral and ground cationic states respectively.[9] The key features in a REMPI spectrum are the vertical electronic transition which shows the energy gap between the singlet electronic ground state, S_0, and, most often, the first singlet electronically excited state, S_1, and the fine structure related to other vibronic transitions. Additionally, under some circumstances rotational fine structure within vibronic levels can also be observed, particularly in smaller systems. Most importantly, REMPI gives mass-resolved spectra, allowing monomers, clusters, or fragments to be distinguished and separately studied. ZEKE spectra give the ionisation energy of a molecule and demonstrate how the vibrational structure of the ion varies when accessed through different vibronic intermediate states.

1.1.3 Vibrations, excitations and Duschinsky mixing

The intensity of an allowed vibrational transition is described by the Franck-Condon factor, which is the squared integral of the degree of overlap between the wavefunctions of the ground and excited vibrational states. This represents the probability of a transition occurring and is reflected in the strengths of spectral features. Molecular vibrations are very sensitive to changes in geometry, which is in turn based on the localisation of electron density across a molecule. Therefore, exciting or removing an electron can alter the vibrational fingerprint of a molecule, and if we understand well the character of the vibrations, we can deduce how the geometry may have changed following the change in electronic configuration. UV spectroscopy can reveal vibrational information about electronically excited states and, through multiphoton absorption, ionised states, and for which Franck-Condon factors provide the connection between changes in internal coordinates and the extent of the vibrational activity in the spectrum.

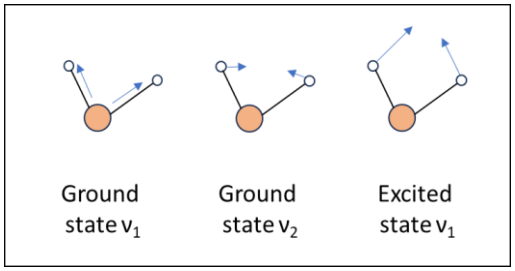

Figure 1-2: Mixing of ground state vibrational character upon excitation.

Vibrations do not necessarily retain the same normal coordinate description when the molecule changes electronic state. We usually assign modes based on the ground state normal modes, but different vibrational modes can mix following electronic excitation, as depicted in Figure 1-2. The term used for such mixing is Duschinsky mixing.[10, 11] The prevalence of this mixing is dependent on the similarity of the geometries between any pair of states, those with more significant differences will usually undergo stronger Duschinsky mixing. The effects that this phenomenon has on experimental spectra are wide-ranging. The asymmetry of emission and absorption bands in UV spectra can be explained by the Duschinsky mixing, as can the presence of intense transitions to optically forbidden vibronic states.[12] This work will investigate how mixing might present between closely related systems, such as between conformers, or in a solvated system, as well as analysing how the mixing is represented in vibronic spectra.

1.1.4 Conformational differences

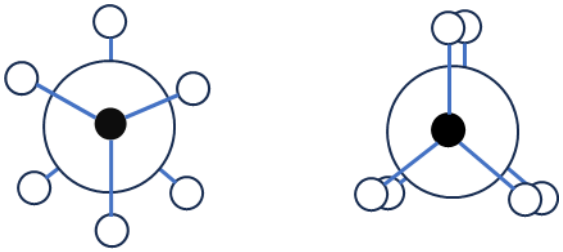

Figure 1-3: Staggered (left) and eclipsed (right) conformers.

Conformational isomerism is the variation in arrangements of atoms in space, due to rotation about single bonds, as seen in the Newman projections in Figure 1-3. When there is a low barrier to rotation, these conformers will be constantly interconverting between the various energy minima via different pathways and through various higher energy transition states. The energetic barriers to interconversion vary widely, depending on substituents, bond order, intramolecular bonding, etc, but many carbon single bond chains have a barrier in the 1-100 kJ mol^{-1} range, which is easily reached through heat energy present in a room temperature/pressure system.

Gas phase spectroscopy allows us to separate out conformers by collisionally cooling them in a supersonic free-jet expansion. This produces an isolated molecule in a vacuum to allow a single conformer to be studied for a short space of time in a fixed conformation.

Gas spectroscopy is also the perfect medium to study the simplest forms of non-covalent interactions, that is, bonding that does not fall under the umbrellas of covalent, ionic, or metallic bonding. Weakly bound complexes are important for two reasons: the weak interactions are interesting in and of themselves as a concept and they also are useful for their application of studying the mostly solvated systems that are found in nature.

1.1.5 Non-covalent interactions

Non-covalent interactions can be broken down into several categories, of varying strengths and occurrences.

Dispersion interactions, also known as instantaneous dipole-induced dipole effects, or van der Waals forces, are constantly adjusting electrostatic forces that build up an attractive force between two atoms or molecules, as one randomly fluctuating dipole induces a dipole in a neighbouring species.

Inductive effects are electrostatic attractions that are induced by one permanent dipole creating a dipole on a neighbour. The strength of these increase with the polarizability of a substance, as a stronger induced dipole can be created. Argon, a large noble gas, is highly polarizable, and therefore often binds strongly to polar molecules, as a large dipole can be induced across it.

Other non-covalent interactions are even stronger. Dipole-dipole bonding, and its particularly strong subset, hydrogen bonding, can form macromolecular structures, such as solvent cages around a solute, and this has been extensively studied for years, both experimentally and computationally.[13, 14]

The importance of weak interactions cannot be overstated. Hydrogen bonding is the reason we have liquid water on earth, the reason DNA forms a double-stranded helix and the reason proteins fold into the correct shape for enzymatic activity.[15-17] The importance of this type of interaction has led to a vast amount of research being undertaken, but with no sign of the number of papers published on this topic decreasing, it is clear there is still much to learn.[18] The application of supersonic free-jet expansions gives opportunity to study these interactions *in situ.*

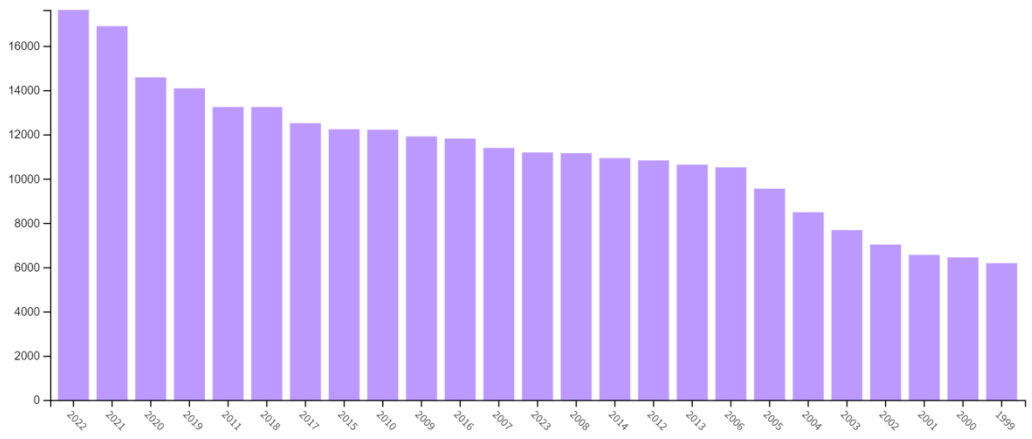

Figure 1-4: Web of Science articles with "hydrogen bonding" in the title by publication year.

The simplest weakly bound class of clusters is the attachment of a single atom to a target molecule. The most commonly studied atoms to bind non covalently to, in particular, aromatic molecules, are noble gases. The increasingly high polarizability of neon, argon, krypton etc, allows a relatively stable dimer to form. The non-reactivity of these gases also leads to low rates of chemical reaction of the resultant complex.

A limitation in gas phase spectroscopy is the difficulty in extrapolating results to a bulk material. One method of exploring the real-world behaviour of an isolated species is to form water complexes. If large enough clusters can be created and studied, they can act as a bridge between gas and solution phase chemistry. The middle ground could be in the development of droplet gas phase spectroscopy.[19] However, the properties of a target can change significantly with the addition of only a single water molecule, so it is there that we can start considering solvation. As well as seeing changes in vibrational signatures of a molecule, we can also use "solvents" as a probe to detect the most favourable binding sites for cluster formation.

Additionally, the strength of a van der Waals attraction can change dramatically upon excitation. "Seeing" an increase in intermolecular bonding can be straightforward spectroscopically, and is a useful marker of the types of excitation taking place.[20] For example, $\pi\pi^*$ excitations can often draw a weakly bound species closer, such as in the example of the argon dichlorobenzene complex,[21, 22] where the argon is bound above the plane of the ring. Counter to that, sometimes an in-plane binding mode such as in the ammonia fluorobenzene complex, can show a characteristic blue shift, showing the weakening in binding energy upon $\pi\pi^*$ excitation.[23] The choice of solvent can therefore be used to examine how different areas of the target molecule change upon excitation.

Simultaneously, many computational techniques have been developed specifically to address weak interactions.[24, 25] This area has been particularly focussed on the development of new density functional theory (DFT) functionals to model van der Waals forces,[26] but other work has been undertaken benchmarking the role of coupled cluster and other perturbative methods in the study of weakly-bound complexes, which show remarkable accuracy but at an increased computational cost compared to empirical methods.[27, 28]

1.2 This work

1.2.1 Method of study

REMPI spectroscopy is an excellent technique for the study of weak interactions, as the mass resolution it affords can distinguish between monomer and clusters, whilst the highly resolved vibrational spectra allow a variety of vibronic states to be used as an intermediate state for the further ZEKE analysis. The ZEKE technique gives a detailed understanding of how the various vibrations change upon ionisation and how the ionisation energies vary from conformer to conformer and from monomer to cluster.

Vibrational assignments of the S_1 state are often based on ground state frequency calculations in the literature, as they are usually simpler and less computationally intensive to run.[29] Of particular relevance to this work, the computational vibrational studies of benzocaine have been entirely focussed on the ground state.[30-32] These calculations are often sufficient to make basic assignments, when coupled with general knowledge of other similar systems. However, sometimes vibrational frequencies can change substantially between different excited states,[33] so it is beneficial to have frequencies calculated at the S_1 level to relate to experimental data. This is also true of newly investigated systems, where there is no reference data to build upon.

The reason many works don't use excited state frequencies is that it is inherently a more difficult result to achieve. The most widely-used method for addressing this challenge is time-dependent density functional theory (TDDFT), due to its cheap cost and its ability to study large-sized systems.[34] However, wavefunction-based techniques are generally superior to DFT in terms of their accuracy, when they are used for systems small enough for them to be cost-efficient.[35] The vibrational analysis of this work is supported by a variety of *ab initio* methods, lending greater credibility to the assignments.[36]

The vibrational assignments for this work are also based on more than just predicted frequencies. Franck-Condon simulations using FCLAB-II,[37] a software package developed by a historical group member, Dr Igor Pugliesi, give a more complete prediction of both REMPI and ZEKE spectra, including ZEKE spectra obtained by photoexciting different vibronic S_1 levels as intermediates. This software uses the results of geometry optimisations for each state of interest produced from other quantum chemical packages to map the geometry change that occurs upon electronic excitation, and gives a simulated REMPI or ZEKE spectrum as an output. Intensities of spectral features are calculated based on the wavefunction overlap, whilst also accounting for Duschinsky mixing, allowing more accurate vibrational assignments than previous works.

1.2.2 Motivation and target molecules

Aromatic molecules are often very good candidates to study in gas phase spectroscopy due to many of their properties.

Firstly, their ubiquity: aromatic molecules exist in almost all areas of chemistry, from the nucleobases that make up our DNA, to the polyaniline conductive polymer in solar cells.[38] The aromaticity inherently stabilise the molecules, giving them great prevalence in many natural products and synthetic areas of study.

Most natural chromophores contain an aromatic moiety. It is this region of a molecule that is responsible for its colour, as the energy gap between the ground and excited state, due to excitation of an often delocalised electron, absorbs light in the ultraviolet or visible region.[39] These chromophores have a tunable band gap, depending on the nearby substituents, lending many thousands of molecules the ability to be studied with light.

Specific to their ability to be studied in our setup, the overlapping system of π orbitals lends rigidity to their structures. This makes them good candidates for study with both REMPI and ZEKE, where very flexible molecules are hard to observe, due to their weak Franck-Condon factors upon excitation or ionisation.

Another key reason to study aromatic molecules is their ability to form weak interactions through bonding to their π system.[40] The ring of delocalised electrons is a highly attractive region for electrophiles, and can lead to self-assembling π-π stacked systems, hydrogen bond-like arrangements with polar solvents, and weakly bound complexes to polarisable species.

The aim of the work presented in this thesis is to use gas-phase spectroscopy and computational techniques to explore the changes in vibrational structure of gas-phase aromatic molecules upon excitation and ionisation. In doing so I will explore how changes in electronic structure can have a large effect on geometry and bonding. In addition, I will focus on how conformational differences can have an impact on otherwise identical systems. Finally, the impact that a weakly bound solvent atom or molecule has on the behaviour in each state was studied.

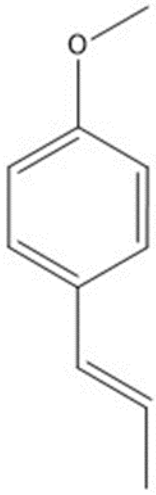

Figure 1-5: Anethole

The first molecule studied was anethole, a natural product used primarily as a flavouring agent. It is extracted from the anise family of plants and is currently being studied for its abilities as a co-polymer, as well as its applications in medicinal chemistry. Recently it has been found to have positive anti-inflammatory[41-43] and anti-carcinogenic[44, 45] effects, amongst other health benefits, and is thought to work at least partially through interference with cell communication, in particular in ion pathways.[46-56]

Ion channel mechanisms are *in situ* solvated systems. It therefore might not seem intuitive to study them with a gas-phase approach. However, if the target molecules we are studying seem to interact with the channels in a weakly-bound manner, gas-phase spectroscopy suddenly becomes an excellent tool for the investigation into the reaction pathways happening in the body. Gas-phase spectroscopy gives the first clues towards what might occur in a solvated environment. Therefore, the second experimental results section will look at the anethole-argon van der Waals complex, as a probe to begin understanding the solvent-molecule interactions with an inert gas.

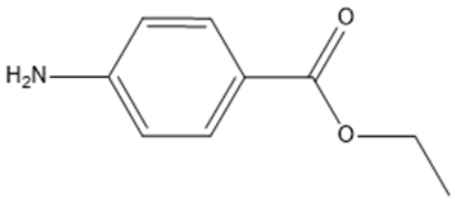

Figure 1-6: Benzocaine

The second molecule of interest is benzocaine, a medicinal molecule used in both therapeutic and clandestine drug use. For the former, as an anaesthetic and in the latter as a bulking agent in the production of illegal drugs, particularly cocaine.[31, 57-59]

The delivery of its medicinal qualities is thought to be via disruption of the ion channels in pain receptors, possibly through non-covalent bonding.[59] For this reason, it was chosen to follow the anethole work. Although well-studied in the past[31, 57, 58, 60], I used it as a benchmarking molecule to test the capabilities of our experimental set up. The work surpassed my expectations by unveiling new vibrational features, including the presence of quantum tunnelling of the amino group that previous ZEKE work had not discovered and led to an extensive REMPI and ZEKE study, tied together with new *ab initio* work.

Chapter 2. Background theory and experimental setup

2.1 Experimental theory

The aims discussed in the preceding chapter are to study the changes in aromatic molecules upon multiphoton absorption, rationalise their vibrational structure in regard to their electronic state, and see how weakly bound complexes behave differently compared to their monomer hosts. To this end we will use gas-phase multiphoton ionisation spectroscopy to produce vibrational spectra of the first electronically excited singlet (S_1) and ground cationic (D_0^+) states.

Gas-phase spectroscopy gives vibrationally and even rotationally resolved spectra, which would be overly complicated to analyse if a sample of molecules displayed a Boltzmann distribution of vibrational states normally found at room temperature. To this end, target molecules are studied by sampling a portion of a molecular beam that is a skimmed section of a supersonic free-jet expansion. This reduces the band width seen in typical gas-phase spectra, to give sharp lines that can lead to finely detailed assignments.

2.1.1 Supersonic free-jet expansion

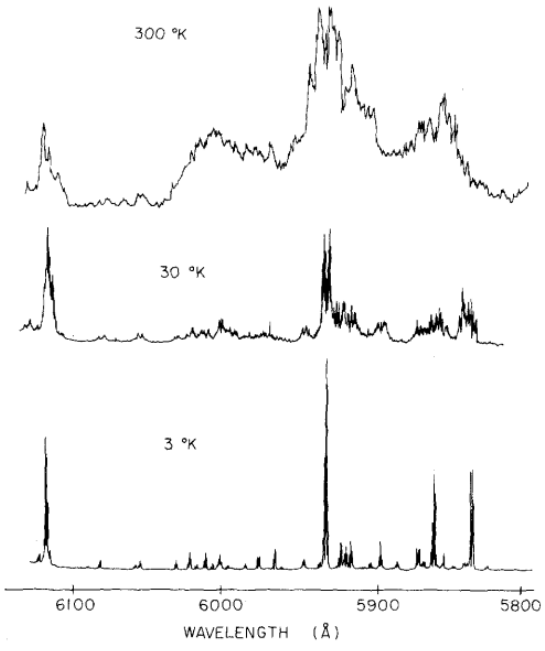

Species that behave as an ideal gas, for instance noble gases, have a mean free path, λ, that can be calculated using Equation 2-1, where k is the Boltzmann constant, T is the temperature, d is the diameter of the molecule and P is the pressure of the gas before it enters the vacuum chamber.

$$\lambda = \frac{kT}{\sqrt{2}\pi d^2 P} \qquad \text{Equation 2-1}$$

Figure 2-1: Reproduced from Wharton et al. showing the increased spectral quality of the LIF spectrum of NO_2 in a supersonic free-jet expansion.[61]

In a relatively high-pressure system such as within a nozzle, there will be many collisions between the atoms. If the diameter of the nozzle orifice that opens to a lower pressure area is much larger than the mean free path, these collisions result in a jet emitted with strong directionality in the outward direction, and a low velocity distribution.[62] If a polyatomic sample molecule is seeded into the noble gas at relatively low concentrations, the small number of sample molecules present in the initial region of the jet will mostly collide with the cold, directional atoms moving the same way, giving directionality to the sample molecule also. Once all particles are moving in mostly the same direction, further low-energy collisions serve to cool the vibrationally and rotationally hot sample molecule, at the cost of a slight rise in translational temperature. This results in an expansion of a uniformly cold gas, where isolated samples are often well below their normal freezing point, making them ideal for spectroscopic study.[63] Figure 2-1 shows the effect of an increasingly cooled jet on the vibronic spectroscopy of NO_2, where large bands are present at higher beam temperatures that then resolve into sharply defined peaks upon cooling. The use of a skimmer downstream from the nozzle removes the portions of the jet with significant translational motion perpendicular to the average direction of flow, and produces a collimated molecular beam, as seen in Figure 2-2. Using a pulsed nozzle gives discrete bursts of jet, and by varying the delay and duration of opening the nozzle we can intersect different regions of the molecular beam with a laser for spectroscopic analysis. At the time that the skimmed molecular beam is intersected by a laser the majority of the molecules will be "frozen" into their lowest vibrational states, which will act as the start point for transitions that occur upon photoabsorption.

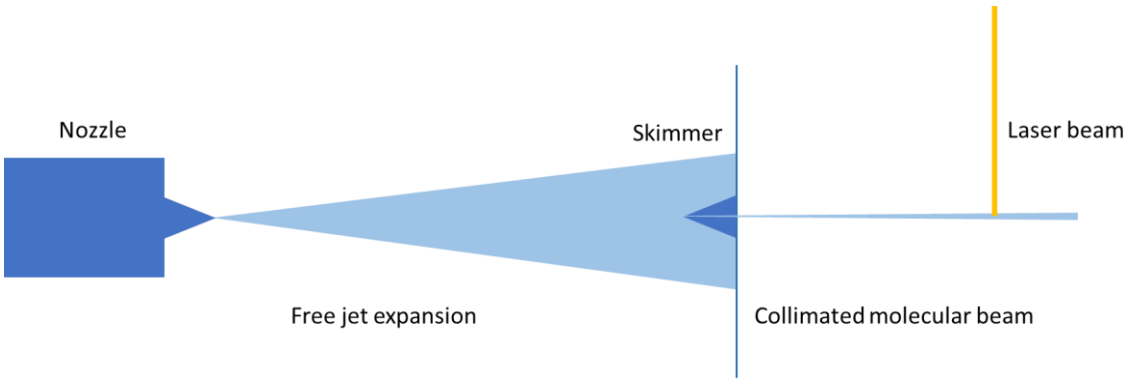

Figure 2-2: Jet expansion in a vacuum.

Within the jet the formation of clusters is possible, as two or more molecules condense together. Due to the isolated nature of the sample in the molecular beam this is a relatively rare occurrence, compared to the presence of monomers. By manipulating the nozzle conditions, such as the backing pressure and concentration of the sample in the carrier gas, the formation of clusters can be encouraged. This gives the opportunity to study weakly bound complexes, held together by as little as

8 cm^{-1} binding energy, which would be extremely difficult to make and isolate under non-cooled conditions.[64] These clusters can be multiples of the sample molecule, combinations of multiple samples introduced into the free-jet expansion or complexations of the sample with the backing gas itself.

2.1.2 REMPI background

Resonance enhanced multiphoton ionisation spectroscopy is an electronic spectroscopy technique that gives a vibrationally resolved spectrum of an excited state by excitation with a photon and the use of a second simultaneous probe photon to ionise the excited molecule. The cation passes along a flight tube and is detected via mass spectrometry. A time-of-flight detection system makes a target molecule distinguishable from photofragments, clusters or impurities in the free-jet expansion, which will arrive at separate delays after ionisation. The mass resolution in our experiment is not small enough to allow separation beyond one mass unit, for instance the difference between a carbon monoxide molecule and a nitrogen molecule, but usually a protonated cation is distinguishable from its monomer equivalent. On a similar note, structural conformers will appear within the same mass channel, despite having different spectra, and thus can cause difficulty when it comes to spectral assignment, as will be seen in the following chapters.

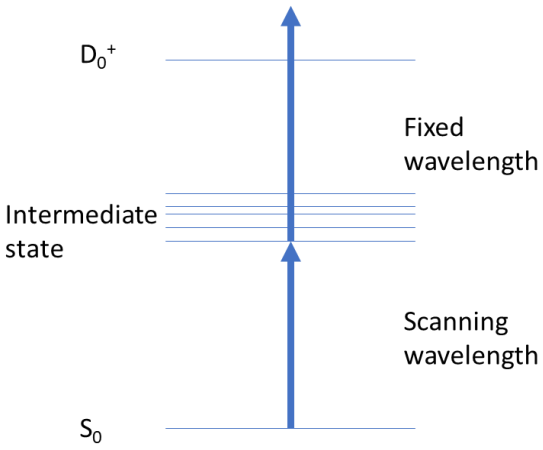

Figure 2-3: Energy levels in a two-colour REMPI experiment.

In REMPI spectroscopy the first photon energy is scanned across the excited state region. The vibronic states reached are dependent on the wavelength of the absorbed photon and the energy gap between the ground and excited state. By varying the incoming photon energy, a variety of vibrationally excited states can be sequentially achieved. The second photon energy is fixed, its only requirement being that it is of

sufficient energy to promote the molecule from the intermediate excited state up to the cation.

A vibrational spectrum of the excited state is collected, where the peak intensity depends on how strong the wavefunction overlap is between the ground and excited states. This gives a spectrum in which we see intensities of vibrational transitions related to the Franck-Condon factor, from which we can extract information about geometry changes upon excitation. The resulting spectrum is comparable to that of a laser-induced fluorescence (LIF) excitation spectrum, whilst the benefits of REMPI over LIF lie in the mass selectivity of photoproducts that a time-of-flight detector provides.

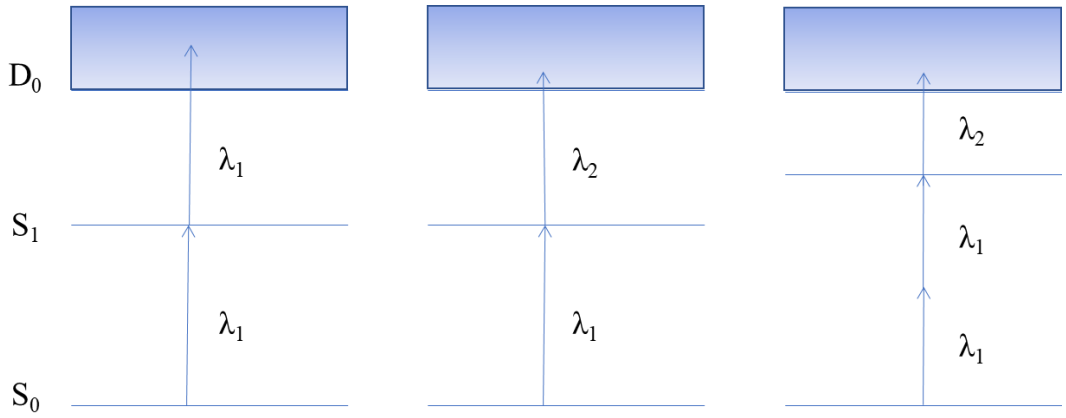

Figure 2-4: Possible photoionisation pathways: (a) 1+1 (left), (b) 1+1' (middle) and (c) 2+1 (right).

When more than one photon is absorbed, there are several possible pathways available, as shown in Figure 2-4. (a) One-colour REMPI uses two or more photons of the same wavelength to achieve photoionisation. (b). Two-colour REMPI uses different wavelength photons. (c) Sometimes, more than one photon is needed to reach the excited state of interest, due to a large S_0-S_1 energy gap, in which case two photons are absorbed simultaneously and then a third is used to ionise (c).

To conduct these three schemes different set ups are required: in one colour REMPI a single laser focuses onto the molecular beam. In two-colour REMPI, two different lasers are focused on the same point in the molecular beam in space and time. This requires laser alignment that superimposes both laser beams onto the same path, so that the molecule is able to absorb photons from both lasers simultaneously. Despite the more complex setup, and the necessity to use two lasers, there are multiple benefits to producing a two-colour spectrum over the one-colour system:

Firstly, whilst acquiring a one-colour spectrum, as you increase the photon energy you are increasing the energy absorbed two-fold, as both photons absorbed are moving to a shorter wavelength. As a molecule absorbs more energy the potential for

it to fragment increases, particularly for weakly bound clusters, where low energy barriers to fragmentation are present. The fragmentation of monomer-containing clusters into the monomer and another species upon photoabsorption will produce a monomer that will then register on the mass spectrometer with the same time of flight as an unaffiliated monomer. This artificially enhances the signal of the target ion and will appear on the spectrum as a rising baseline of signal intensity with increasing photon energy, as a greater proportion of the ion signal derives from fragmentation of higher order clusters. There may also appear features in the spectra that seem to be vibronic transitions in the monomer which are actually resonant with a vibronic state in the cluster.

Conversely, if a two-colour spectrum is being taken, only the first photon absorbed will be increasing in energy across the scan. This means that there should be less excess energy that could lead to fragmentation upon absorption of two photons, and consequently fewer fragments created. Thereby giving a less congested spectrum where most features correspond to ion formation from multiphoton absorption of the monomer.

Secondly, there are some systems that are impossible to study with one-colour REMPI spectroscopy, based on the relative energies of their excited and ionised states. If the energy gap between the ground and excited state is smaller than the gap between the excited state and the ion, your second photon will not have sufficient energy to achieve ionisation. In this case a two-colour experiment is vital in order to provide the shorter wavelength needed to achieve ionisation with the second step.

For two- or more-photon absorption to the excited state, strong focusing of the laser onto the molecular beam is necessary to increase the photon flux sufficiently to create a high rate of photoionisation. This technique was not used in this work so is mentioned here only as an interesting demonstration of the scope of REMPI experiments.

2.1.3 ZEKE background

Zero energy kinetic electron spectroscopy builds on the foundation that REMPI has set. It studies the vibrational states of a cation by detection of the complementary electrons to provide a vibrational spectrum of the ion. ZEKE spectroscopy is also a multiphoton technique, where the first photon wavelength is selected to be resonant with a vibrational level in the excited state of the molecule and then the second photon wavelength is scanned through the vibrational states of the ion.

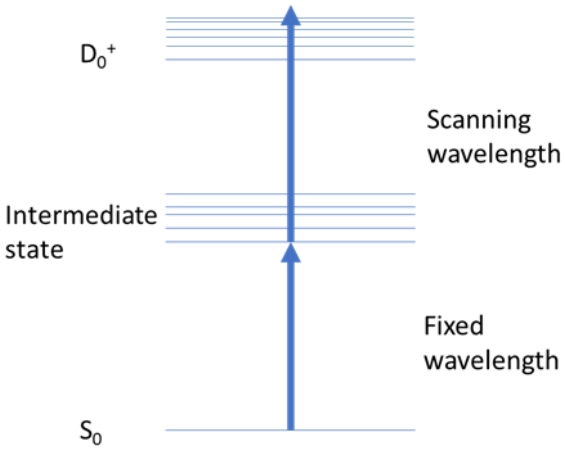

Figure 2-5: Energy levels in a ZEKE experiment.

Similarly to its less highly resolved parent technique, photoelectron spectroscopy, electrons are detected when a species is ionised. Rather than measuring the kinetic energy of a photoelectron, and thus deducing the energy of the molecular orbital it has come from (Koopmans theorem),[65] what sets the ZEKE technique apart is that only the threshold electrons, those with very low kinetic energy, (or zero-energy kinetic electrons, ZEKE) are detected. The low energy electrons are produced when the absorbed photon energy is resonant with a (ro)vibronic state of the cation, leaving no excess energy. Higher energy electrons are produced when a photon absorbed is not resonant with a vibronic state of the cation, thus converting the excess photon energy above the ionisation limit into kinetic energy of the electron. This separation of electrons by their energy is performed through the use of pulsed electric field ionisation.

The reason we are able to discriminate the high and low energy electrons is because the so-called ZEKE electrons are actually weakly bound Rydberg electrons, occupying a high n (n > 150) Rydberg orbital in the cation, where n is the principal quantum number. Rydberg electrons have a very low penetrating character toward the nuclei, and are so far removed from the molecule that they effectively experience it as a point charge, yielding a longer lifetime than a more closely bound excited state.

This is because most decay pathways, such as autoionisation and radiative decay occur due to interactions between the excited electron and the core. By spending less time close to the core electrons and nuclei, these pathways occur at a much slower rate. Rydberg states with electrons inhabiting orbitals of n=100-200 can have measurable lifetimes on the nanosecond timescale.[66, 67] Meanwhile, from the moment of photoabsorption, the ionised electrons with excess energy will travel away in all directions, leaving behind weakly bound Rydberg electrons without excess energy. These electrons lie just below the ionisation threshold and can therefore be field

ionized after a short delay by a pulsed negative electric field, giving a burst of electrons that reach the detector a delayed time after the initial free ionised electrons.[68] The field-ionized electrons can therefore be distinguished from the non-resonant ionised electrons by their different flight times before reaching the detector after the laser pulse.[69]

The Rydberg character of these states increases their lifetimes, but not enough, however, that we should see meaningful amounts of field ionised electrons after the delay, which is on the order of one microsecond. The further inflated stability of the Rydberg states is due to stray electric fields and the Stark effect.

This effect was discovered in 1913 independently by Johannes Stark and Antonino Lo Surdo, for which the former was awarded the Nobel Prize for physics in 1919. It is the phenomenon of the splitting of spectral lines upon exposure to an external electric field, analogous to the Zeeman effect, but with an applied electric field rather than magnetic. Previously degenerate energy levels will split into higher and lower energies when an electric field is applied across the atom or molecule. This effect is more pronounced for electrons occupied in an orbital with a high principal quantum number as these tend to be further away from the nucleus and therefore the difference in electric field across the diameter of their orbit is greater.

The Stark effect comes into play in the ZEKE experiment, because it extends the lifetime of the high n Rydberg states that are created, as the low angular momentum states overlap with states of higher *l*, within the same manifold. Mixing of the states occurs, resulting in a more weakly defined set of states, of higher angular momentum than the originally optically pumped state, thus lowering the time the electron spends near the nucleus and slowing down the rates of decay. This extends the lifetime of the Rydberg states until they can be field ionised.

One effect of generating a high density of ions in a small area during photoionisation is that the plasma created can trap some of the free electrons, which then go on to be collected alongside the field ionised electrons and appear at the same time of flight, artificially inflating the signal intensity. To discriminate between the prompt electrons and the field ionised ones we use a pre pulse, or discrimination pulse: a weak, pulsed electric field that appears a few hundred nanoseconds after photoabsorption. This sweeps away the unbound electrons, leaving behind only those electrons still trapped in Rydberg states. It also has the additional effect of field ionising the highest energy of the Rydberg states within the state-scrambled manifold. So long as the voltage applied is not too high, typically in the region of a few hundred millivolts, a later extraction (repeller) pulse can be used to field ionise the subsequent slice of states.[9, 70] The repeller pulse serves the dual purpose of field-ionising the remaining Rydberg electrons, and repelling them along a flight tube toward a detector.

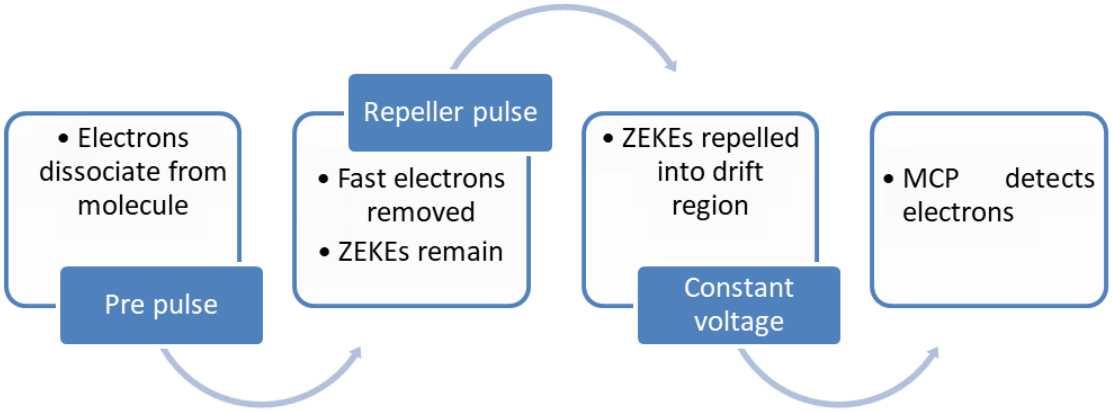

Figure 2-6: Collection of field ionised electrons in a ZEKE experiment.

The subtlety of the ZEKE technique lies in varying the intensity, duration and delay of the discrimination and repeller pulses, to sample a sufficient depth of Rydberg states, whilst avoiding collecting photoionised electrons at the same time.

2.2 Description of the experimental setup

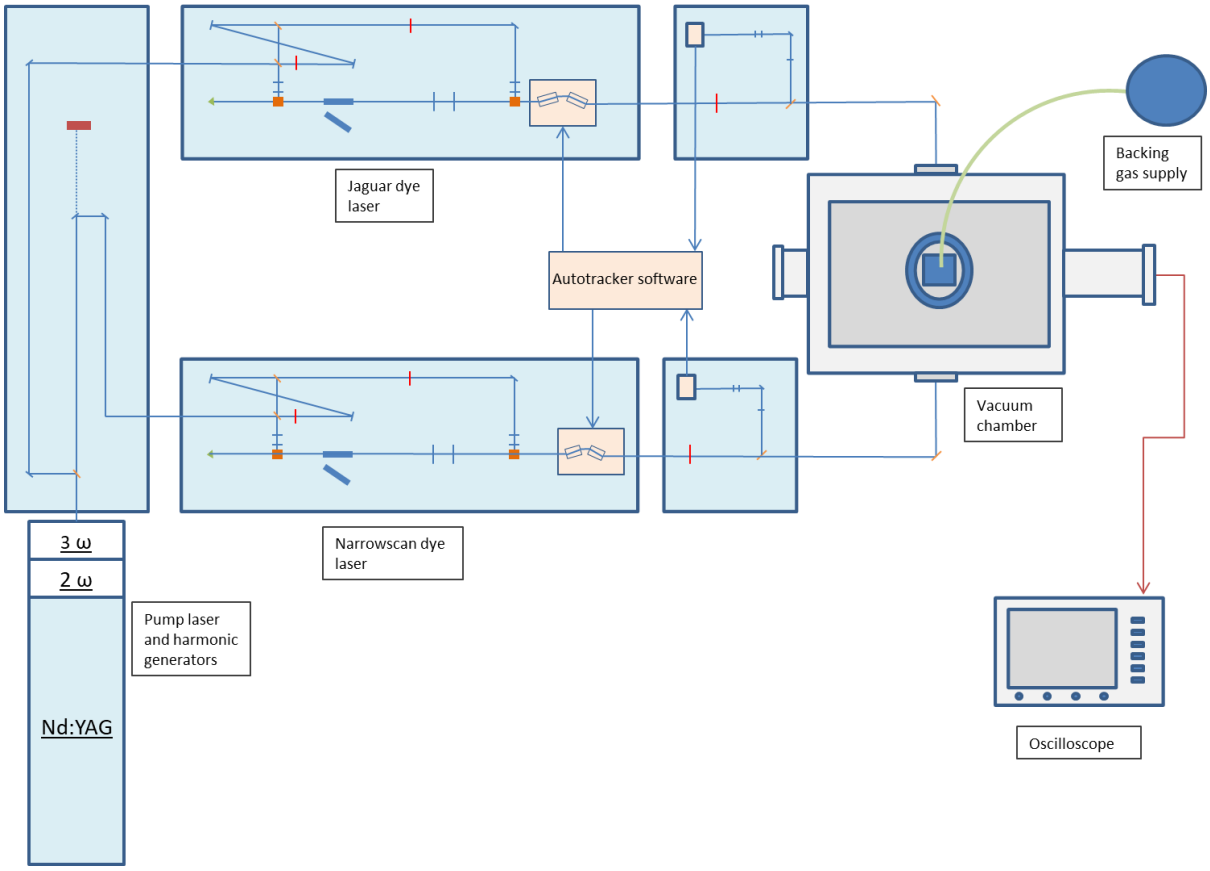

Figure 2-7: Schematic of the REMPI and ZEKE laser setup.

2.2.1 Laser system

Light for the two experiments is produced using the frequency-doubled output of two dye lasers, both optically pumped by a Quantel Q-Smart 850 Nd:YAG nanosecond pulsed laser.

Harmonic generation is the production of photons at a certain wavelength from the absorption of multiple photons at a longer wavelength. Second and third harmonic generation of the 1064 nm fundamental is achieved using potassium dihydrogen phosphate (KDP) crystals in series, the first to frequency double the fundamental to produce 532 nm light, the second to mix the second harmonic with the fundamental to produce the third harmonic, 355 nm.

These are separated downstream using hard-reflecting mirrors, chosen to remove one frequency of light and reflect it onto a separate path from the other frequencies that transmit through. In this way it is possible to pump the two dye lasers with different wavelength light from the same pump laser. If both dye lasers are required to be pumped by the same wavelength, the hard-reflecting mirrors are removed and replaced with beam splitters.

In two-colour spectroscopy both photons must coincide with the molecular beam simultaneously. This is ensured by introducing an optical delay before the closer of the two dye lasers, so that the light enters both dye lasers synchronously.

The dye laser output goes through a KDP or beta barium borate (BBO) crystal and a compensator crystal. These double the frequency of the light, and ensure that the beam path stays straight as the wavelength changes. Upon exiting the dye lasers the light passes through another beam splitter, and across to a series of prisms that adjust the route of the light through the vacuum chamber. Opposite sides of the chamber each contain a quartz window, which allows the transmittance of UV light. If correctly aligned, the two dye laser outputs will meet in the centre of the chamber, as verified by two perfectly overlapping laser pathways between the sets of prisms. If the beam intensity is too strong, then neutral density filters can be placed between the prisms and the chamber to attenuate the light.

The portion of dye laser output that was removed by the beam splitter is fed through an iris and a neutral density filter (sometimes multiple) to a photodiode with four windows. These are used in the running of the autotracker apparatus, which rotates the doubling crystal as the wavelength is scanned.

2.2.2 The autotracker

The autotracker system is newly installed based on previous components and new designs, and has been adapted for use in this experiment by myself. I shall therefore describe it in some detail here.

As the dye laser wavelength scans, the angle at which it must pass through the doubling crystal changes, due to the requirement of wavelength-dependent phase-matching at the surface of the crystal. The autotracker setup ensures the continued doubling of the light by rotating the first (BBO or KDP) crystal, whilst synchronously rotating the compensator crystal to ensure the path of the laser beam does not translate horizontally as the wavelength changes.

There are two main methods of keeping the crystals well aligned. Firstly, a curve can be plotted showing the angle of the harmonic generator against the wavelength to give the maximum power output, and then set the two crystals to follow that curve, or secondly, the crystals can be adjusted in real time, based on the output power as the wavelength changes.

The first method is flawed, as it is dependent on the quality of the curve being followed, in addition, the laser calibration may be weaker at some points than others, giving an unreliable curve gradient. The second method is employed in this experimental setup, and relies on splitting the output beam, directing it onto a photodiode and altering the angles of the KDP and compensator crystals to maximise the output intensity.

A section of the beam is diverted away from the rest of the apparatus and then passes through an iris to a photodiode. The iris is important in selecting the right section of the beam profile. The output of the dye lasers is not strictly a circular shape, but rather an elongated oval with a tapered top and bottom.

Figure 2-8: Beam profile of a dye laser.

It is important to select either the very top or bottom of the beam profile, as this is narrower than the main section of the beam and therefore is easier to track as it varies horizontally.

The photodiode has four windows, arranged as seen in Figure 2-9.

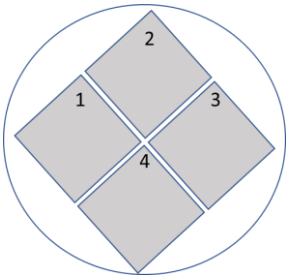

Figure 2-9: Arrangement of photodiode windows in the autotracker equipment.

These are divided into two output streams: horizontal and vertical. The horizontal output is made up of two channels, one from pane 1 and one from pane 3. The vertical output is composed of the raw outputs from pane 2 and pane 4.

Using an oscilloscope to visualise the response from the pairs of windows, the beam is aligned centrally across all four. This is done by ensuring the signal outputs are equal across all four panes, varying the beam position using a prism or mirror. Photodiodes have maximum light limits they can process before they become saturated, and therefore one or more neutral density filters can be placed between the prism and the photodiode to ensure the beam intensity is not too high. It is also critical that scattered light from the laser does not pass onto the photodiode as this will result in an incorrect laser alignment, and thus a blackout tunnel has been created and installed in front of the photodiode, only permitting light to enter from one direction (that of the prism).

Once centrally located, the beam intensity tracks left or right as the wavelength changes, this registers as a disparity between the two horizontal photodiodes, one of which will register less light hitting it, and the other more.

A laser pulse is not emitted as a square function with a simple off and on difference. The intensity of light emitted follows a Gaussian function, with a full width at half maximum (FWHM) of about 6 ns for our laser.

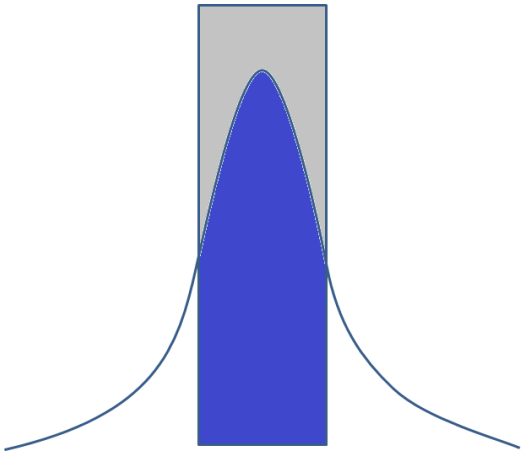

Figure 2-10: The temporal region of the laser pulse that is selected for integration.

A custom-built integration box takes a time selected slice of the output signal, and integrates that part of the laser pulse intensity. We adjust the gain of this integrated slice to make sure both horizontal channels have the same amount of background noise. Labview software, provided by Dr Fiona Whiting who used a similar set-up, then processes this signal again to vary the sensitivity of the channel differences, then monitors the intensity of light. If the difference in channels varies outside a specified range, it signals a motor to turn which then turns the second harmonic generator and compensator crystals. This ensures the beam direction stays in line at all times. Motor step size can be selected using the labview software to adjust sensitivity in response to the scan speed.

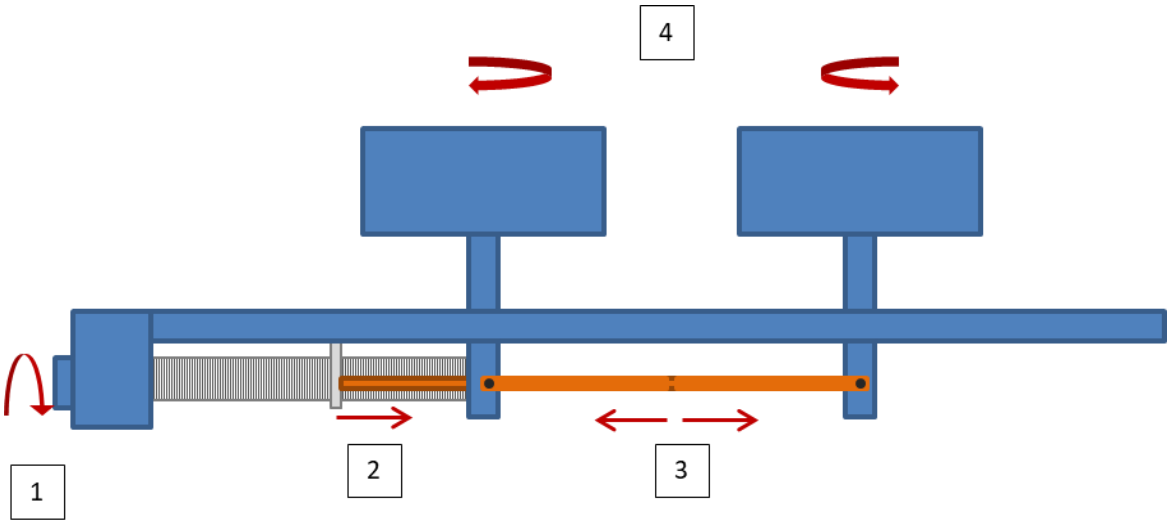

Figure 2-11: Controlling the second harmonic generation and compensator crystals.

Figure 2-11 shows the mechanism by which the harmonic generation crystals move. As the motor turns (1) it rotates a belt connected to a second cog. This is fastened to a long screw which rotates as the motor turns. As the screw turns a nut is drawn in and out along a groove in the table above (2). This tightens or loosens two copper belts that are attached to the end (3). These are attached to the posts with the crystals atop, which rotate and turn the two crystals simultaneously counter to each other (4).

2.2.3 The vacuum system

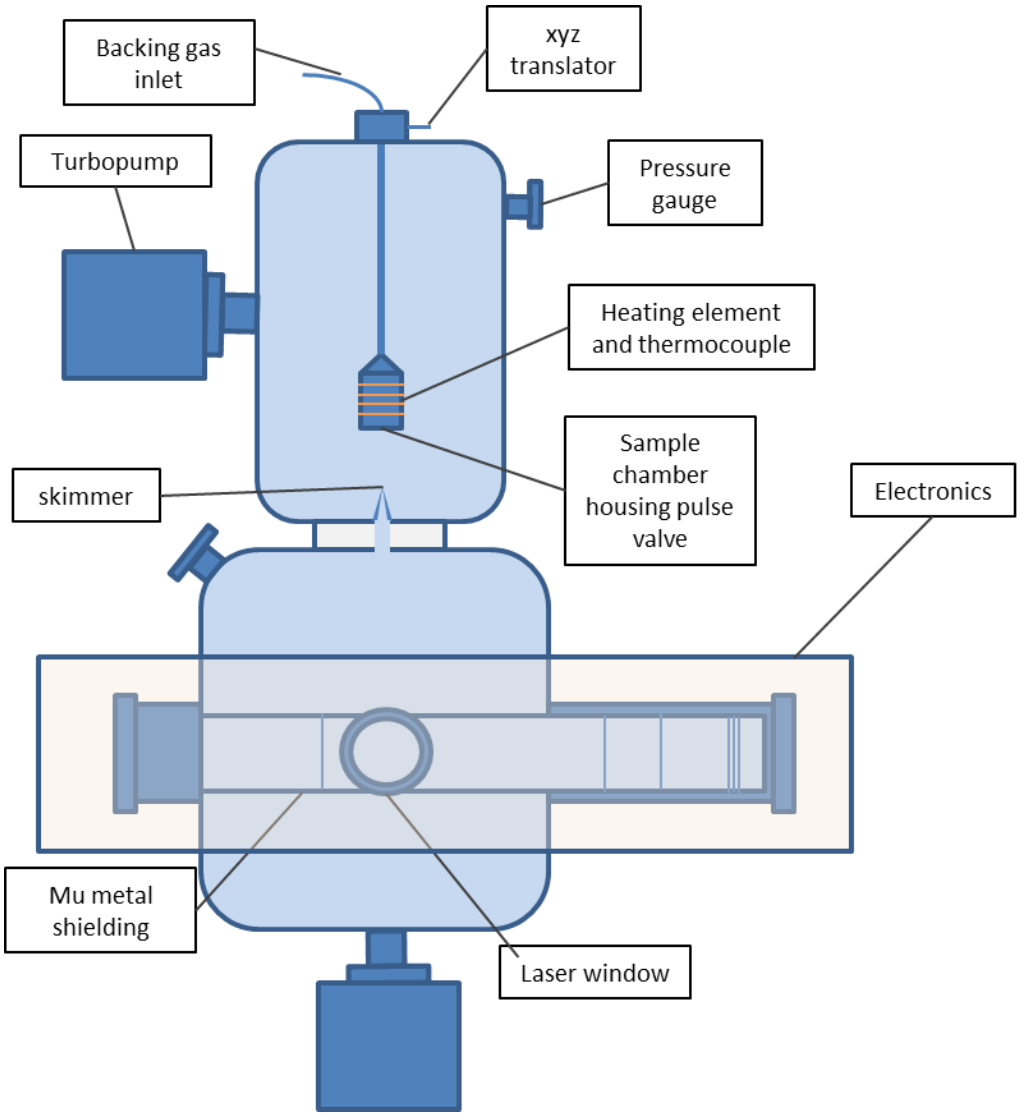

Figure 2-12: The vacuum system in the REMPI and ZEKE experiments.

Pfeiffer Hipace 700 Turbopumps differentially pump two chambers, the expansion chamber, where the supersonic expansion is emitted, and the interaction chamber,

where the skimmed molecular beam coincides with the laser. These are backed by a Pfeiffer two-stage rotary pump. This pumping system allows vacuum pressures to be kept at 1.1×10^{-7} mbar in the interaction chamber throughout the experiment.
To achieve sufficient vapour pressure of the sample within the nozzle pre-expansion, heating is often required. A sample holder is housed inside the first vacuum chamber, comprising a reservoir wrapped in high resistance wire, enclosing a Series 9 pulsed valve underneath. The nozzle is controlled by the same time delay system as the lasers and detector, which will be described later. Current limited voltage is passed across the wire to warm the ensemble, including the nozzle, with a maximum temperature of 105 °C achievable before internal components begin to fail. The temperature is monitored by a thermocouple attached to the top of the reservoir.

Samples are selected that have high enough vapour pressure to provide sufficient signal intensity within the range of temperatures achievable by the heater. Room temperature liquids are ideal, but many solid samples are also able to be studied using this technique.

A backing gas supply line is connected to the entrance of the reservoir, allowing mixing of the vapour and gas before being pulsed through the nozzle. A typical backing gas is argon or helium. The pressure of the backing gas can be varied to adjust the relative partial pressures of sample to backing gas; this has a strong effect on the vibrational temperature of the sample once ejected, and heavily impacts the formation of clusters in the molecular beam. Typically, the backing gas pressures used are between 0.1 and 2 bar.

Once emitted, the expansion passes approximately 5 cm across the first vacuum chamber and then through a 2 mm skimmer into the interaction chamber. This removes the vibrationally hot parts of the beam and ensures that the majority of sample molecules that pass through the skimmer have been cooled into their lowest vibrational and rotational states.

The skimmed beam travels 10 cm across the second chamber into a tube of mu metal shielding, which shields the following interactions from stray magnetic fields. It is then intersected by the output of the two dye lasers and photoionisation occurs.

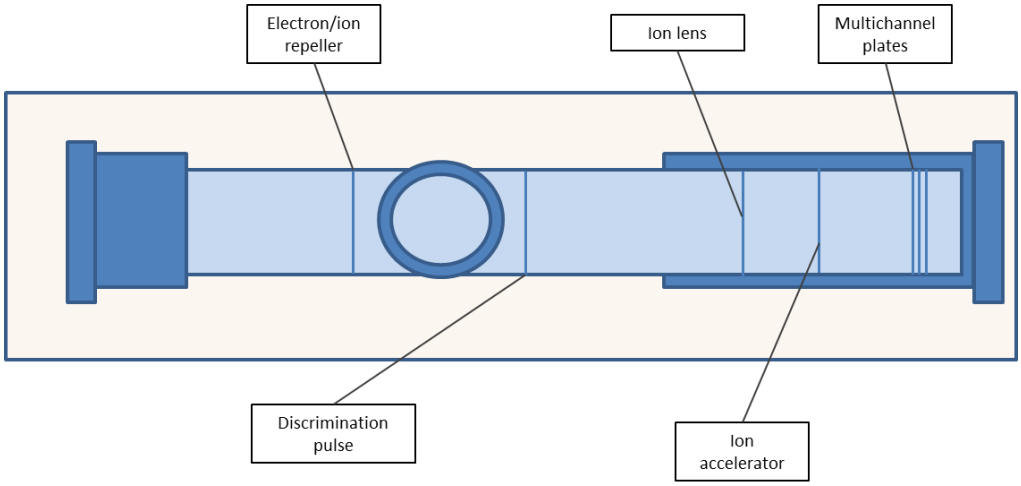

Figure 2-13: Electronics inside the vacuum chamber.

Both the ZEKE and REMPI experiment use the same detection system, which is adjusted to suit whichever of the two species is being detected.

REMPI

Upon ionisation the ion repeller has a positively charged electric field passed across it, which repels the positive species away from the ionisation region. The cations are accelerated into a drift region, held at a constant negative voltage. At this point the ions separate out by mass based on their velocity going into the drift region, with the lighter molecule being accelerated faster and then travelling through the region correspondingly quicker. At the end of the drift tube is a series of multichannel plates (MCPs). These are negatively charged, and when a cation connects with them this produces a cascade of electrons, providing a current to an anode connected to the signal output. The signal is fed into an oscilloscope which registers a series of features separated temporally into each mass being detected.

ZEKE

The ZEKE experiment uses the same apparatus as the REMPI. This time there is a pre-pulse, also called a discrimination pulse, first, where a negative voltage is passed across a mesh plate to repel the unbound electrons away.

Secondly the repeller plate has a pulsed negative voltage pass across it, to field ionise the ZEKE electrons and repel them into the drift region. The electrons then travel to the same MCPs, this time that have a positive voltage across them, and are detected in the same manner as the ions.

Timings

These various experimental components need to be linked together to work coherently. The timing of each individual component in the experiment is

coordinated using a Quantum 9520 Series Pulse Generator. This ensures that the laser pulses are timed to coincide with the sample pulses and the data acquisition timing range.

By varying the relative timings, the region of the sample jet being ionised can be controlled, leading to differently cooled properties, including the temperature of the monomers and the presence of clusters.

2.3 Computational Chemistry

2.3.1 Hartree-Fock method

Computational chemistry is built on mathematical principles that remain in constant development, with the overarching goal to be able to describe the properties of molecules, atoms, and electrons as correctly as possible.

For all but the smallest systems there are not the capabilities to deliver outright answers that are completely accurate. Instead, approximations are made that lower the computational cost of the calculations, whilst keeping the answers as close to correct as possible. The skill of a computational chemist lies in choosing the correct methods for the job at hand, understanding the limitations of each method, and understanding the effect these limitations have on the results.

The area of computational chemistry research is deeply rooted in quantum mechanics, which took off in the early 20th century. The formation of the Schrödinger equation as a resolution for the time-dependent character of a wavefunction represented a huge leap forward in our ability to understand and describe the quantum world around us. Solving this equation for more complex systems became, and still is, the ultimate goal of computational chemistry.

With the development of computers exploding in recent years it is a fast-growing discipline whose limits are constantly evolving, as the processing power of new supercomputers, the advent of artificial intelligence and the ingenuity of new chemical software increases the scope within which we can study.

To begin to build an understanding of the overarching reach of computational chemistry it is important to begin with the fundamental approximations. Calculations can fall into several categories, including *ab initio*, (methods that rely entirely on quantum mechanics, i.e. are derivable from first principles) semi-empirical (methods that incorporate empirical data into the models), and fully empirical.

Some mathematical background is needed to explain the choices in methodology used in this work. These principles have been extensively discussed elsewhere,[6, 71, 72] but I shall briefly summarise the key points, and how they relate to this work.

The simplest building block of *ab initio* methods, and the starting point for many more complex methods, is the Hartree Fock (HF) method.

To study the chemical world computationally an understanding is needed of the properties of both the nuclei and electrons in a system, to know the energy and positions of each quantum component is the goal. This is done through solving the non-relativistic time independent Schrödinger equation:

Equation 2-2

$$\hat{H}|\Psi\rangle = E|\Psi\rangle$$

Here, $\hat{H}$ is the Hamiltonian operator for both the electronic and nuclear components, E is the energy of the system, and Ψ is the wavefunction, the description of the probability of the vector coordinates of a system.

The Hamiltonian operator contains five terms: the electronic kinetic energy,$\hat{K}_e$, the nucleic kinetic energy, $\hat{K}_N$, the coulombic attraction between electrons and nuclei, $\hat{V}_{eN}$, the repulsion between electrons, $\hat{V}_{ee}$, and the repulsion between nuclei, $\hat{V}_{NN}$.

Equation 2-3

$$\hat{H} = \hat{K}_e + \hat{K}_N + \hat{V}_{eN} + \hat{V}_{ee} + \hat{V}_{NN}$$

These terms is described by the masses, m_e and m_i, and distances, r_j and R_i, concerning the electrons and nuclei respectively. In addition, Z_i refers to the nuclear charge of the nucleus, *i*.

$$\hat{K}_e = -\sum_{i}^{electrons} \frac{\hbar^2}{2m_e}\nabla_{r_i}^2$$

$$\hat{K}_N = -\sum_{i}^{nuclei} \frac{\hbar^2}{2m_i}\nabla_{R_i}^2$$

$$\hat{V}_{eN} = -\sum_{i}\sum_{j} \frac{Z_i e^2}{4\pi\varepsilon_0 |R_i - r_j|}$$

$$\hat{V}_{ee} = \sum_{i}\sum_{i<j} \frac{e^2}{4\pi\varepsilon_0 |r_i - r_j|}$$

$$\hat{V}_{NN} = \sum_{i}\sum_{j>i} \frac{Z_i Z_j e^2}{4\pi\varepsilon_0 |R_i - R_j|}$$

This gives a very complex function, computationally unsolvable for systems larger than hydrogen. As most chemists are interested in larger molecules an approximation is needed to calculate the wavefunction. This simplification is the Born-Oppenheimer approximation.

The Born-Oppenheimer approximation states that whilst both electrons and nuclei are moving freely within a system, the relative speeds at which they move are vastly different, due to their mass. Electrons move so fast about the nuclei that the nuclear

positions can be considered fixed in a moving sea of electrons. This allows us to transform the nuclear terms in the previous equations and consider them as a constant. This allows the movement of electrons to be considered spontaneous with respect to the nuclear framework. This approximation gives the electronic Hamiltonian:

Equation 2-4

$$\widehat{H}_{elec} = \widehat{K}_e(r) + \widehat{V}_{eN}(r; R_a) + \widehat{V}_{ee}(r)$$

If the electrons are assumed to not interact with each other (a very big assumption, but a fair starting point), we can combine the wavefunctions for single electrons, *x*, into a many-electron solution to the Schrödinger equation:

Equation 2-5

$$\Psi_{HP}(x_1, x_2, \dots, x_N) = \psi_1(x_1)\psi_2(x_2) \dots \psi_N(x_N)$$

Now it is important for us to consider the Pauli principle, which states that no two electrons can occupy the same quantum state within a system.

This introduces the spin requirement into quantum mechanics; rather than describing an electron with both a spatial coordinate and a spin coordinate, we use the spinorbital notation: *X*. We then invoke the antisymmetry principle.

If any two electrons are exchanged, their wavefunctions must change sign:

Equation 2-6

$$\Psi(x_1, x_2) = -\Psi(x_2, x_1)$$

And it is because of this that Slater determinants become the best, simple expression for a set of spin orbitals in a multi-particle system. These determinants describe the wavefunction of a system comprised of multiple electrons and/or nuclei.

Equation 2-7

$$\Psi(x_1, x_2, \dots, x_N) = \frac{1}{\sqrt{N!}} \begin{vmatrix} X_1(x_1) & X_2(x_1) & \cdots & X_N(x_1) \\ X_1(x_2) & X_2(x_2) & \cdots & X_N(x_2) \\ \vdots & \vdots & \ddots & \vdots \\ X_1(x_N) & X_2(x_N) & \cdots & X_N(x_N) \end{vmatrix}$$

The use of Slater determinants means that if any two electrons were attempted to be described identically, the value of the wavefunction would become zero.

Next, to find the solutions to the Schrödinger equation the variational method is used, varying the initial spin orbitals, formed from a finite set of atomic basis functions in the wavefunction to achieve the lowest possible energy.

Equation 2-8

$$\langle \Psi_0 | \hat{H} | \Psi_0 \rangle = E_0$$

To this end the electronic Hamiltonian equation is used to solve the molecular wavefunction, that is constructed as a Slater determinant to give an eigenvalue energy ε_0. Small changes in wavefunction guess are repeated, until the change in ε_0 becomes lower than a specified threshold. These cycles give rise to the name self-consistent field, (SCF) and are usually the starting step in most *ab inito* methods.

This method has some drawbacks, firstly, the neglect of relativistic effects and secondly, the lack of electron correlation.

Several methods of correcting these limitations have been developed. Post Hartree-Fock (HF) methods build on the HF principles, alongside additional calculations, to reduce the inaccuracy introduced through the previous approximations. These methods all take more computational resources than the Hartree-Fock method and therefore the choice of method used is system-dependent.

2.3.2 Møller-Plesset perturbation theory

The Schrödinger equation can only be fully solved for very small systems. However, by replacing the Hamiltonian operator, H with a simplified version H_0, we can treat this small change as a perturbation and adapt the Schrödinger equation:

Equation 2-9

$$\left(\hat{H}_0 + \lambda \hat{\mathrm{V}}\right)\Psi = E\Psi$$

Where

$$\hat{H}_0 + \lambda V = \hat{H}$$

So long as λ is less than one we can find an enhanced solution to the Schrödinger equation by a series of perturbation expansions:

Equation 2-10

$$\Psi_i = \Psi_i{}^{(0)} + \lambda \Psi_i{}^{(1)} + \lambda^2 \Psi_i{}^{(2)} + \cdots$$

That produces a set of perturbed energies:

Equation 2-11

$$\mathrm{E}_i = E_i{}^{(0)} + \lambda E_i{}^{(1)} + \lambda^2 E_i{}^{(2)} + \cdots$$

Møller-Plesset perturbation methods (MPn) use a modified Hamiltonian that is the sum of all the Fock operators for all electrons, and the HF wavefunction for the zeroth order term.[73]

Now for the sum of the zeroth and first order correction terms this gives exactly the HF answer:

Equation 2-12

$$E_i^0 = \langle \Psi_i | \widehat{H} | \Psi_i \rangle$$

However, subsequent perturbations contain a large component of correlation energy factored in, giving a more accurate energy than the HF one. More than two orders of perturbation give increasingly accurate results, but MP3 and MP4 are rarely seen in the study of anything other than very small molecules, as the computational cost renders them unfeasible for larger systems. MP2 represents the best cost to accuracy compromise for many systems.

2.3.3 Coupled cluster methods

A second post Hartree-Fock method is coupled cluster, of which there are many submethods, CCS, CCSD, CCSD(T) etc.

These methods follow on from the HF method, but the wavefunction seen in is replaced with an exponential ansatz to account for the electron correlation.

Equation 2-13

$$|\Psi\rangle = e^T |\Phi_0\rangle$$

Here Φ_0 is a reference wavefunction taken from the output of the HF calculation. T is the operator which produces the excited state determinants from the reference wavefunction.

The magnitude of the T factor varies depending on how many excitations you want to look at. It can be written in the form:

Equation 2-14

$$T = T_1 + T_2 + T_3 + \cdots$$

Where the subscript denotes the number of simultaneous excitations, 1 equals single excitations, 2 double etc. The general form of the operator can be written this way:

Equation 2-15

$$T_n = \frac{1}{(n!)^2} \sum_{i_1,i_2,\ldots,i_n} \sum_{a_1,a_2,\ldots,a_n} t_{a_1,a_2,\ldots,a_n}^{i_1,i_2,\ldots,i_n} \hat{a}^{a_1} \hat{a}^{a_2} \ldots \hat{a}^{a_n} \hat{a}_{i_n} \ldots \hat{a}_{i_2} \hat{a}_{i_1}$$

Where i represents the occupied orbitals, and a, the unoccupied orbitals.

These methods can become extremely computationally expensive when more than single and double excitations are accounted for. At this point it becomes more efficient to treat the triply excited term in a perturbative manner and add that on to the singles and doubles answer, giving CCSD(T).[74]

2.3.4 Density functional theory

There is another method, density functional theory, which is routinely used in the area of spectroscopy. DFT models the behaviour of an atom or molecule by estimating the spatial electron density within the boundaries of the system. It is a computationally cheap method that relies on the selection of specific functionals, which are functions of functions, that have been individually created to suit different computational needs. For example, some functionals are designed to better model the long-range electrostatic interactions associated with a hydrogen bonded system.[75] Without using system-specific functionals the results of DFT calculations can be patchy, although there are several "all-round" functionals, such as B3LYP[76] which are often used for initial calculations before further refinement is needed.[77] Whilst a useful tool, the arbitrariness of functional selection gives it substantial room for user error and the results cannot always be accurately compared across multiple systems.

2.3.5 Resolution of the identity: coupled cluster method

RICC2 is an adapted CCSD method, where the Hamiltonian is partitioned into a Fock operator ($\hat{F}$) and a fluctuation operator ($\hat{U}$).

Equation 2-16

$$\hat{H} = \hat{F} + \hat{U}$$

These are then separately perturbed to give results of a similar quality to MP2 calculations, but with the huge advantage of calculating excitation energies, so systems other than the ground state can be studied.[78] This is necessary for my work on photoexcitation, and it is good to have both ground and excited states calculated

using the same method, as comparisons between them are more reliable than switching methods.[79]

For the work in this thesis, the systems studied were small enough that the higher accuracy methods could be used without reaching a computationally expensive bottleneck. Rather than playing the game of chance with DFT and functional choices, I could select a method that would give more reliable results, I therefore chose the RICC2 method for the majority of my calculations.

2.3.6 Basis sets

Besides choosing a method the complexity of the spinorbitals provided into the calculations must also be considered: Mentioned before were sets of basis functions, these are known as basis sets and are integral to the quality of results we get.

A basis set is a combination of atomic orbital-like functions that we place on the coordinates of atoms in a calculation. The simplest basis set we could provide is one that describes exactly the number of atomic orbitals to contain all the electrons in a system. However, by incorporating more "virtual" orbitals we increase flexibility into the calculation, affording us more accurate results.

It is possible to further adapt the properties of these orbitals, by including basis sets with higher orders of angular momentum as polarization functions, shifting electron density away from the atomic centres and increasing the accuracy of describing delocalised electronic behaviour. Diffuse functions are also important in this work, as these are added to the basis set when describing diffuse electron behaviour is key, for instance in the study of anions, or hydrogen bonding.

A final point to consider is how basis sets can interact during the study of multiple species. Basis set superposition error (BSSE) is an artificial lowering of the total energy of a system when the basis sets on two individual monomers interact, which can increase the apparent strength of the bonding between the two. In the case of Van der Waals bound complexes this overestimation can be dramatic.[80, 81]

Boys and Bernardi developed the method of counterpoise correction to account for this, which takes separate calculations of all fragments in a system as well as the system as a whole, to ensure an accurate binding energy of the complex.[82] Many benchmarking studies have been published to assist in method and basis set choice for computational chemists.[83-85]

In this work all calculations were carried out using Turbomole 6.4[78] and Gaussian16.[86] This project was undertaken on the Viking Cluster, which is a high performance computer facility provided by the University of York.

2.3.7 Franck-Condon simulations

To aid in the analysis of the experimental data collected the optimised geometries and the frequencies of the vibrations of our target system at each of the relevant states were calculated. This is usually the ground state, S_0, first excited singlet state, S_1 and the cation ground state, D_0^+.

This gives predicted frequencies for the lines in the REMPI and ZEKE spectra, which are then processed using a multidimensional Franck-Condon analysis software, FCLAB-II to give simulated spectra with line intensities calculated based on the Franck-Condon overlap between the optimised geometries in the pairs of states we are studying, (S_0 to S_1 in REMPI, S_1 to D_0^+ in ZEKE). This software is also used to estimate the Duschinsky mixing, comparing how the vibrations in each state are well described relative to one another.[37]

Chapter 3. Anethole

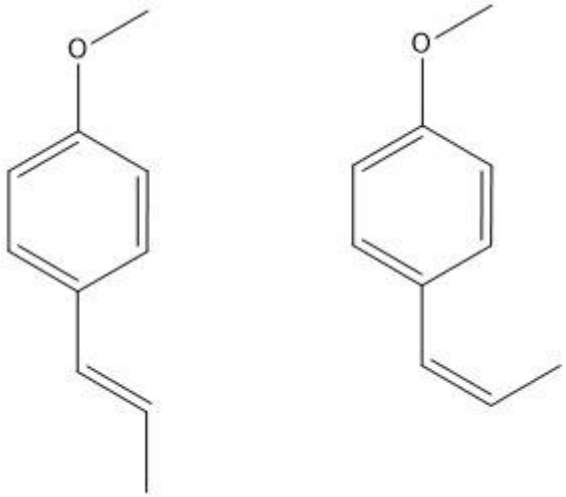

Figure 3-1: *Trans* (left) and *cis* (right) anethole

3.1 Introduction

Anethole (IUPAC name 1-methoxy-4-[(1E)-prop-1-en-1-yl]benzene), is a naturally occurring aromatic molecule, extracted from the fennel, anise and star anise plants. It occurs as either a *cis* or *trans* isomer, with the *trans* being the most naturally abundant, the most flavourful, and the exclusive isomer studied in this work.

It is a component of natural polymers, where it plays some part in the UV protection of the plant from the rays of the sun. Anethole has been included in recent work on biopolymers, whilst unable to homopolymerise, it does act as a co-polymer, where its introduction alters polymer properties such as branching frequency and the formation of cross links.[87, 88] Macromolecular properties were also affected; it is shown that the addition of anethole units to a vinyl polymer reduced the water uptake significantly.[47] As a plant-based oil, anethole shows potential as a renewable alternative to petrochemical polymers. It can be collected from the turpentine-like extracts from trees,[89] or can be synthesised using the method by Haarmann and Reimer, whereby anisole is condensed in the presence of an acid catalyst with propionaldehyde.[90]

Additional properties of anethole are anti-bacterial and insecticidal traits.[91] Despite this, it is considered non-hazardous to humans and is widely used in the food industry as a flavouring agent.[92] It has an interesting property as one of the main molecules responsible for the ouzo effect. The mechanism by which a strongly hydrophobic substance, dissolved in ethanol becomes a highly stable microemulsion upon the addition of water. This striking and spontaneous state change is often seen

in mixology as water or ice is added to an anise-flavoured liquor, such as absinthe, sambuca or its namesake, ouzo. This property makes it a molecule of interests in the study of a wide range of emulsions.[93, 94]

Anethole has been chosen for this work because of its interest as a natural product with UV-protection qualities and its potential medicinal effects. As a substituted aromatic it is well-suited for study with gas-phase techniques, and in particular holds interest as a vector for the study of weakly bound complexes. The lone pairs on the oxygen and the additional presence of a π system give ample opportunity for weakly bound clusters to form. However, this present chapter will focus on the monomer, with the following chapter exploring complexes formed between anethole and a single argon atom.

3.1.1 This work in context

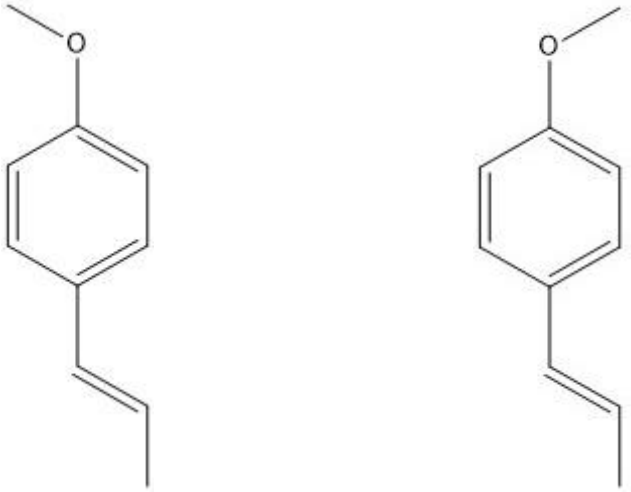

Figure 3-2: *Anti* (left) and *syn* (right) conformations of anethole.

A number of previous spectroscopic studies of *trans*-anethole have been performed: in 1989, a REMPI study of various styrene derivatives presented the first 200 cm^{-1} of the anethole REMPI spectrum.[95] Their one-colour spectrum displayed two band origins associated with the *syn* and *anti* orientations of the two substituent groups. That paper also suggested that the likely geometry of anethole in both the S_0 and S_1 states is planar.

More recently, the laser induced fluorescence (LIF) spectrum of anethole was recorded by Barber and Newby in 2013.[96] They found the *anti* conformer to be slightly lower in energy than the *syn*, (67 cm^{-1}), whilst relative intensities of the *syn* and *anti* band origins were approximately equal, with the higher energy band associated with the *syn* conformer, being the slightly stronger. This may be surprising, considering a higher population of the lower energy conformer is likely to be present in the cold molecular beam, but this feature has been attributed to different fluorescence quantum yields between the two conformers. These two papers served as the basis for this work, which plans to expand upon conformational analysis presented in the 2013 paper, as well as providing a clear picture of the vibrational structure of the cation through the ZEKE experiment.

3.2 Experimental

3.2.1 REMPI and ZEKE

Anethole was obtained from Fisher Scientific and used without further purification. It was introduced to the vacuum chamber with no additional heating, using argon backing gas at a stagnation pressure of 0.1 bar. It entered the vacuum chamber through a Parker Series 9 general pulse valve operating at 10 Hz, as a supersonic free-jet expansion. The expansion passed through a 2 mm diameter skimmer into a separate, differentially-pumped interaction chamber, where it was intersected by the perpendicular output of one or two laser beams. Upon ionisation the ions are accelerated along a 22 cm flight tube to a multi-channel plate detector. The recorded time-of-flight provides the means to determine the relative masses of the ions impacting on the detector, thereby effectively yielding a time-of-flight mass spectrum.

Two-colour REMPI spectra were recorded using the frequency-doubled output of two dye lasers, both of which were pumped by a single Nd:YAG nanosecond pulsed laser. Typical laser powers were of the order of 1-3 mJ per pulse pre doubling.

The probe (ionisation) photon was provided using DCM dye in ethanol in a Radiant Dyes Jaguar dye laser, giving a frequency-doubled output of 315 nm. The second, photon, from a frequency-doubled Radiant Dyes Narrowscan dye laser, was scanned from 310 nm to 290 nm using a 1:1 mixture of DCM and sulforhodamine B dyes in ethanol.

Once the two-colour REMPI spectrum had been obtained, a number of ZEKE spectra were recorded via a selection of different vibrational intermediate levels. In

these experiments, the Jaguar laser employed Pyridine 1 laser dye in ethanol to generate the longer wavelength light needed to access the adiabatic ionisation region.

Pulsed field ionisation was initiated using a weak (roughly 1V) discrimination pulse and a second repeller pulse shortly after. The time delay between these pulses was varied from 500 to 1500 ns.

Data was acquired using a ten-shot average of each point, scanning in 0.005 nm step sizes for both experiments. Laser wavelengths were calibrated against the optogalvanic lines of a neon lamp.

3.2.2 Computational

The *syn* and *anti* conformers of anethole were optimised in their neutral ground, first excited singlet state and cation ground state. Potential energy surfaces (PES) were constructed to estimate the barrier to rotation between the two conformers. REMPI and ZEKE simulations were produced for each conformer, and in the case of ZEKE, for each of the S_1 intermediate states that were investigated spectroscopically. All optimisation and frequency calculations were run at the RICC2/aug-cc-pVDZ level of theory using Turbomole 6.4.[78, 97, 98] PESs were constructed using Gaussian at the MP2/aug-cc-pVDZ level of theory.[97, 99] FC-LabII was used to calculate the Duschinsky mixing and to simulate spectra.[37]

3.3 Experimental Results

3.3.1 REMPI

An initial one-colour REMPI spectrum of anethole in the range 32800 to 34000 cm^{-1} is presented in Figure 3-3. The spectrum reveals a large number of vibrational features building from what appears to be two distinct band origins. An uneven baseline, symptomatic of signal saturation can be seen. Such effects can be dramatically reduced by employing greatly reduced pump laser energies in a two-colour experiment.

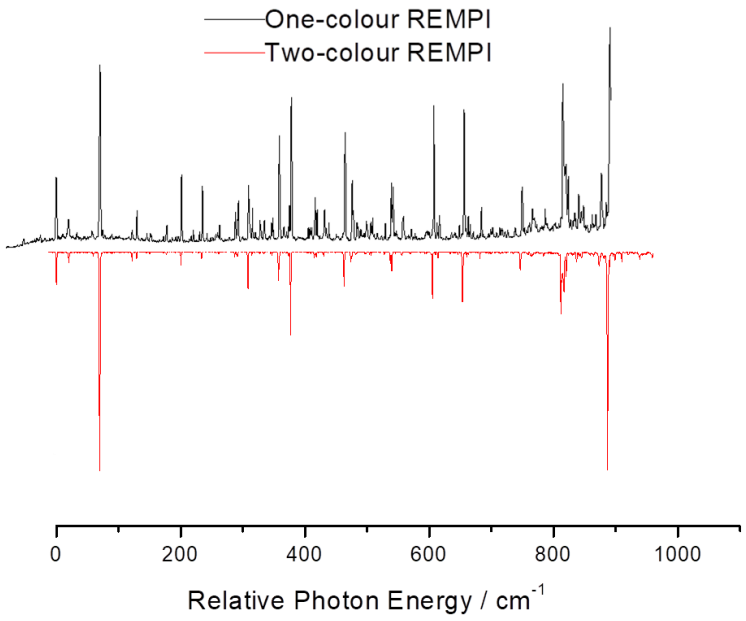

Figure 3-3: One-colour (top) and two-colour (bottom) REMPI spectra of anethole.

In the two-colour REMPI spectrum many features have disappeared into the baseline, revealing the true relative intensities of the vibronic features. Several of the disappearing bands could have been due to higher-order clusters fragmenting upon ionisation and arriving in the monomer mass channel on the time-of-flight (TOF). The overall energy imparted was reduced by providing a second colour photon of lower energy than the first colour, thus lowering the likelihood of fragmentation.

A detailed assignment of the spectrum will be given in section 3.4.2, but it is clear that the spectrum shows a doubly-repeating pattern of features separated by approximately 70 cm^{-1}, indicative of there being two conformers present in the molecular beam, as reported previously. This allows separation of the various spectral components into two distinct and mostly similar spectra, overlaid upon each other.

3.3.2 ZEKE

A number of ZEKE spectra were recorded via a selection of S_1 state intermediate levels, including the two band origins at 32889 cm^{-1} and 32959 cm^{-1}, the pair of *syn* and *anti* ν_{39} mode vibrational levels at 33197 cm^{-1} and 33265 cm^{-1}, respectively and two individual levels, the *anti* ν_{56} mode (at 33246 cm^{-1}), and the other assigned to the *anti* ν_{33} mode (at 33774 cm^{-1}).

Six intermediate states were probed, giving a vibrational spectrum of the cation following excitation to each S_1 vibronic state chosen. The ionisation energy was also found, as the sum of the pump photon and the lowest energy feature in each spectrum. This confirmed the presence of two conformers, each with a distinct ionisation energy. Unfortunately, it was not possible to measure the origin features of the final two spectra due to a poor signal to noise ratio and incomplete spectra, so definitive conformational assignment was not made.

Origin positions were seen as the lowest frequency feature in ZEKE spectra 1-4 at the following frequencies:

Table 3-1: Frequencies of the states used as intermediate points for the collection of anethole ZEKE spectra.

S_1 state assignment	**Pump frequency /cm^{-1}**	**Origin frequency / cm^{-1}**	**Ionisation energy / cm^{-1}**
***Syn* origin**	32889	27726	60615
***Anti* origin**	32959	27665	60624
***Syn* ν_{39}**	33197	27419	60616
***Anti* ν_{39}**	33265	27359	60624
***Anti* ν_{56}**	33246	Not measured	
***Anti* ν_{33}**	33774	Not measured	

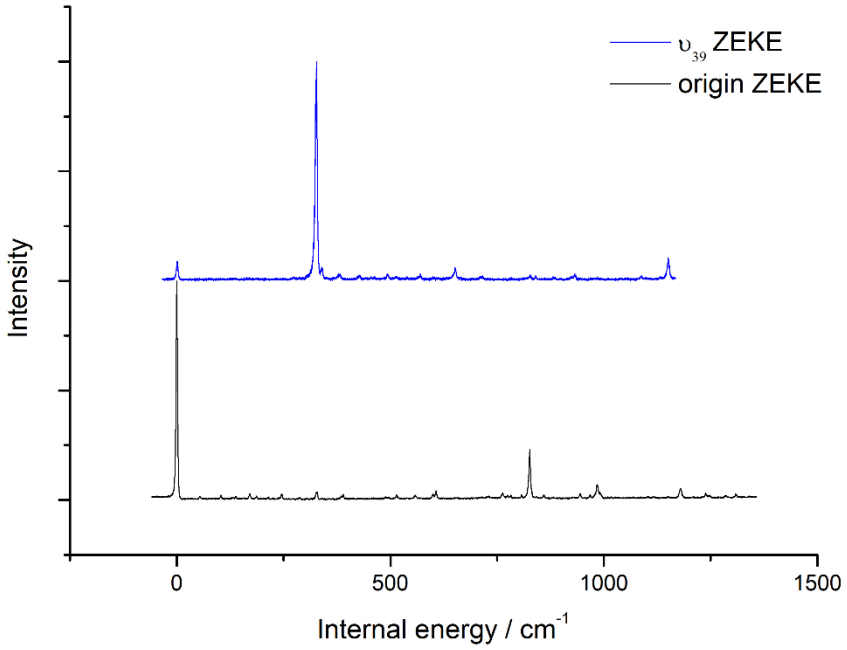

Figure 3-4: Normalised *syn* conformer ZEKE spectra using the ν_{39} (top) and origin (bottom) intermediate S_1 vibronic states. Internal energy is the excess energy above the cationic ground vibronic state.

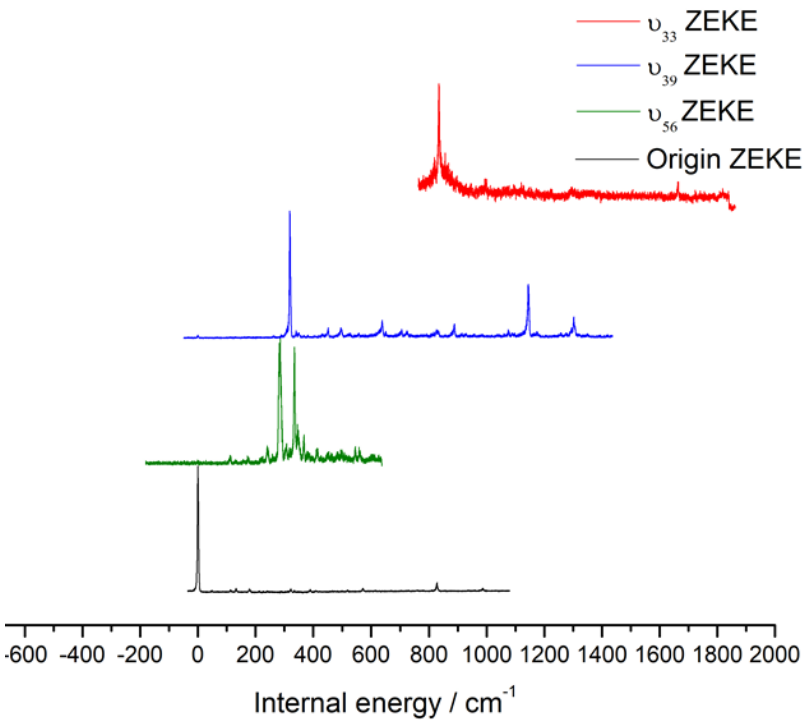

Figure 3-5: Normalised *anti* conformer ZEKE spectra using the ν_{33} (red), ν_{39} (blue), ν_{56} (green) and origin (black) intermediate S_1 vibronic states.

As seen in Figure 3-4 and Figure 3-5, each ZEKE spectrum was dominated by the $\Delta v=0$ diagonal transition, with the exception of the ν_{56} pumped spectrum which showed two strong features and a multitude of lesser peaks.

3.4 Discussion

3.4.1 Computational results and discussion

Two local minima were identified, associated with the two conformers, with the *anti* conformer found to be marginally more stable. The rotation about either the propanyl group or the methoxy group gives a molecule where the substituents are positioned facing in the same direction, *syn*, or opposite directions, *anti*, (see Figure 3-2). A relaxed potential energy surface scan was performed to reveal the barrier to rotation of the propanyl group relative to the methoxy group.

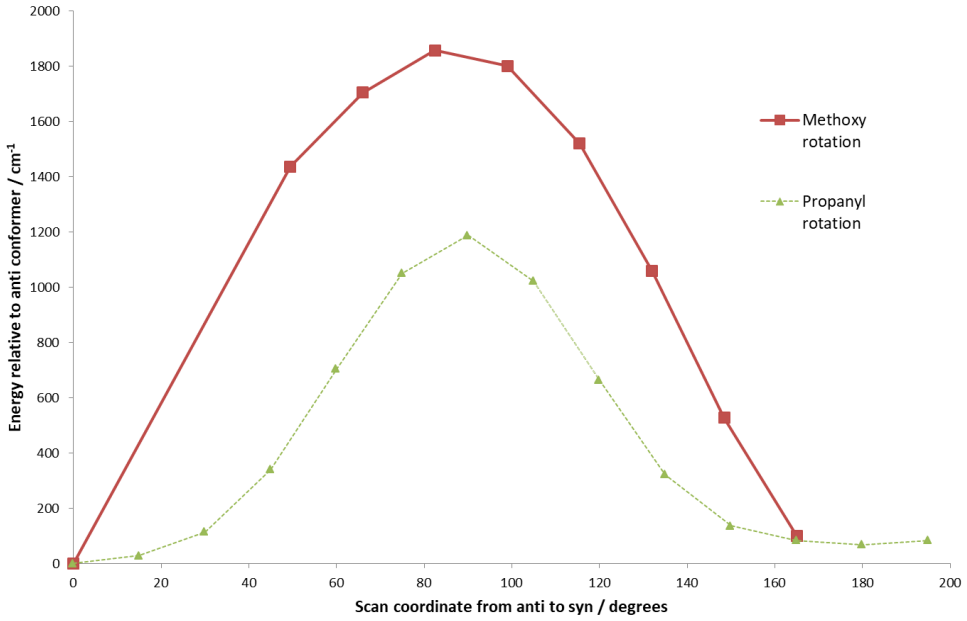

Figure 3-6: Ground state *anti* to *syn* rotation energy barrier

These calculations reveal a barrier to rotation of 1187 cm^{-1} in the ground state, for rotation of the propanyl group, and 1923 cm^{-1} for the methoxy rotation. This could be due to the shorter C-O bond that links the methoxy group to the ring compared with the C-C bond that attaches to the propanyl group, (1.36 Å compared to 1.46 Å respectively). This causes the hydrogens on the substituents to be held closer to the ring in the methoxy group, leading to increased steric hindrance upon rotation.

The energy difference of 78 cm^{-1} between the two minima favours the *anti* conformer and is likely the result of a weaker spatial overlap between the bulky ring substituents in this form. Less steric overlap results in weaker electron-electron repulsion and a lower potential energy. This is in good agreement with previously calculated energy differences, reported by Newby *et. al* to be 37cm^{-1}.[96] The cation ground state has a similar energy difference between conformers, whilst the first excited singlet state of neutral anethole displays a reversal in conformational stability, whereby the *syn* conformer becomes lower in energy than the *anti*.

Table 3-2: Conformer energies by state (zero-point corrected)

	S_0 relative energy	S_1 relative energy	Ion relative energy
Syn / cm^{-1}	69	0	62
Anti / cm^{-1}	0	228	0

A Boltzmann analysis based on the calculated energy difference, ΔE, of 69 cm^{-1} (821 J mol^{-1}) shows that at room temperature the distribution of conformers will be

fairly even, at a ratio of about 1.4:1 N_1:N_0, *anti:syn*, assuming no interaction is occurring between conformers. *R* is the universal gas constant and *T* is temperature.

Equation 3-1

$$\frac{N_1}{N_0} = e^{\frac{-\Delta E}{RT}}$$

The ratio of peak intensities of the origin band of each conformer show a 5:1 ratio of *anti*:*syn*. Assuming that the probability of the v=0 transition is roughly the same for both conformers, which we expect it is based on the later analysis, a description of the cooling process in the supersonic jet can be speculated.

As the anethole molecules are entrained into the argon buffer gas and are cooled within the supersonic free-jet expansion, the effective temperature of the molecules drops significantly, resulting in a significantly higher proportion of the lower energy conformer, the *anti*, being present. Working backwards from these ratios we can therefore estimate the temperature of the molecular beam at the time of photoabsorption to be around 70 K. This is in contrast to the other possible process that could occur in the jet, whereby collisional cooling occurs so deeply and quickly that the room temperature relative abundances of two conformers are frozen in as the jet expands. For the former process to have occurred, the energy barrier to conversion must be low enough to be overcome via the energetic collisions of the buffer gas, giving a higher proportion of the lowest energy conformer.

The S_0 to S_1 vertical excitation energies for the *syn* and *anti* conformers were calculated to be 32681 cm^{-1} and 32758 cm^{-1}, respectively. This aligns very well with their relative spectral positions which show the *syn* origin band at 32889 cm^{-1} and the *anti* origin at 32959 cm^{-1}.

The intensity of a vibronic transition in a spectrum is dependent on a number of factors, one of which is whether or not the transition is "allowed" according to various selection rules. These depend on the symmetry of the initial, ψ_v', and final, ψ_v'', vibronic states. For a transition to be allowed the integral of the wavefunctions of the initial and final vibronic states and the dipole moment operator, μ, must be non-zero:

Equation 3-2

$$\int \psi_v' \cdot \mu \cdot \psi_v'' \neq 0$$

This occurs in non-degenerate states only when the integrand of the symmetry of each component is totally symmetric:

Equation 3-3

$$\Gamma(\psi_v') \times \Gamma(\mu) \times (\psi_v'') = A$$

Anethole is calculated to be planar in all three electronic states, (S_0, S_1 and D_0^+). It belongs to the C_s point group, and all vibrations will have either A′ or A″ symmetry. The transition dipole moment is in the plane of the ring, and therefore in-plane vibrations, those with A′ symmetry will be allowed according to the electric dipole selection rule, whilst only combinations or even quanta excitations of the out-of-plane, A″ modes will be allowed, because the products of two A″ symmetries are A'.

To aid in vibrational assignment, a simulated spectrum for each conformer was produced from the results of the *ab initio* calculations described below. FClabII was used to produce a Franck-Condon simulation of a REMPI spectrum based on the calculated geometries and vibrational frequencies, produced at the RICC2/ aug-cc-pVDZ level of theory. These calculations will undergo further description and analysis in section 5.2.

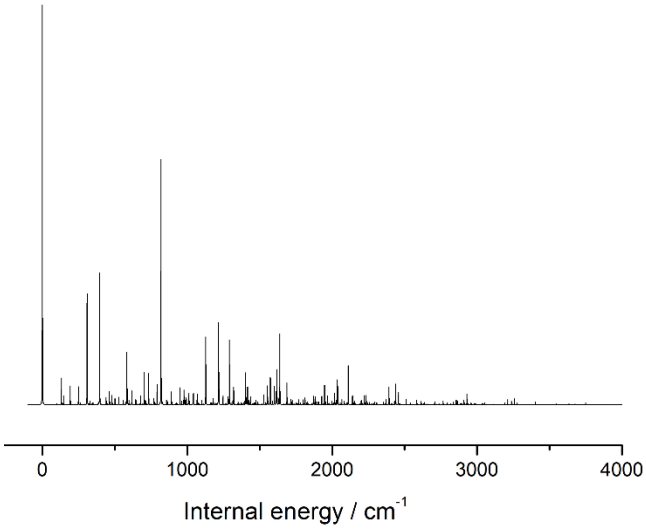

Figure 3-7: *Anti* conformer simulated REMPI spectrum

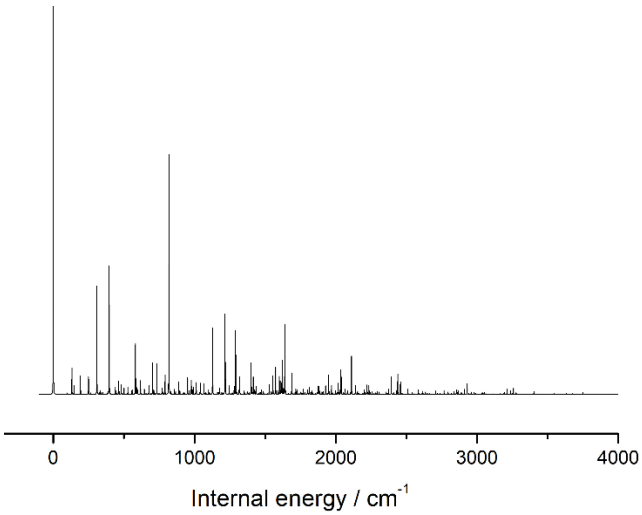

Figure 3-8: *Syn* conformer simulated REMPI spectrum.

The strongest features of the simulated REMPI spectra pictured in Figure 3-7 and Figure 3-8 were two in-plane bending and stretching motions of the substituents, ν_{39} and ν_{38}, and the ring breathing mode, ν_{33}, depicted in Figure 3-10, Figure 3-11 and Figure 3-12 below. These are predicted to occur at approximately 310 cm^{-1}, 390 cm^{-1} and 800 cm^{-1} for both conformers.

The two simulations were combined, using a weighting of 5 to 1 *anti* to *syn* intensity based on relative intensities of the two experimental origin features. This simulation gives excellent agreement with the experimental two-colour REMPI spectrum, (Figure 3-9), which suggests that the simulation provides an accurate predictive view of the region of the spectrum unexplored in the experiments described here.

ZEKE spectra were also simulated for a variety of intermediate vibronic states using this same method, where a quantum of excitation in each vibrational mode that was probed was added to the S_1 geometry starting point. These are seen in section 3.4.3.

3.4.2 REMPI

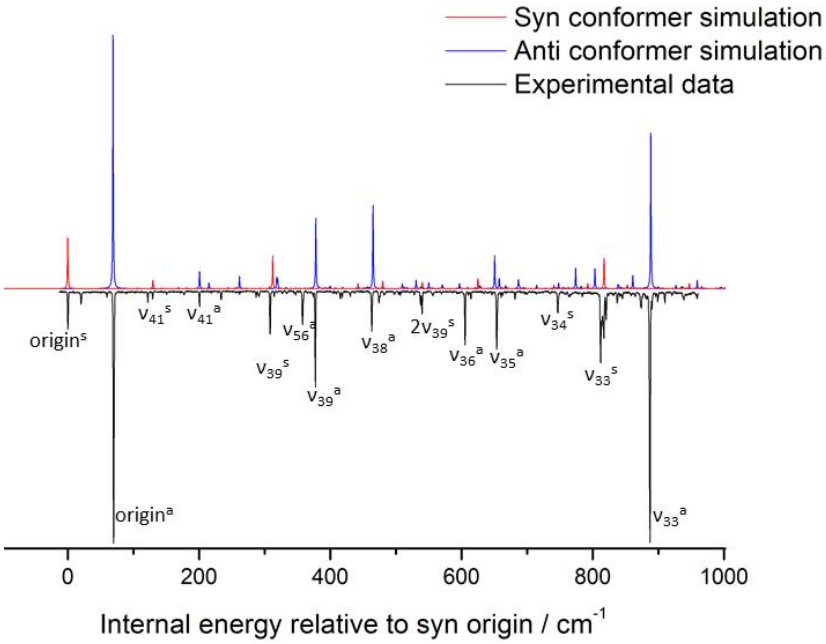

Figure 3-9: Simulated REMPI spectrum of *syn* and *anti* conformers compared to experimental data with key assignments. ^{s} refers to the *syn* conformer, ^{a} refers to the *anti* conformer.

A detailed assignment of the two-colour REMPI spectrum is shown in Table 3-3. The assignments have been made from an analysis of the S_1 and D_0^+ state vibrational frequency calculations and the outcome of the pump-probe ZEKE experiments. Mulliken vibrational mode numbering is used throughout, where $\nu_{0\text{-}41}$ are vibrations with A' (in-plane) symmetry, and $\nu_{42\text{-}63}$ have A'' (out-of-plane) symmetry.

Table 3-3: REMPI spectral assignments, vibrational frequencies are presented as their position relative to the origin of each conformer.

Vibrational assignment	*Syn*		*Anti*	
	Exp. freq.	Calculated freq.	Exp. freq.	Calculated freq.
Anethole-argon origin			-48	
Monomer origin	0	0	0	0
An-H_2O origin	60		51	
ν_{41}	129	130	130	132
$\nu_{63} + \nu_{61}$	177	181	164	146
$2\nu_{62}$			192	193
ν_{40}			244	249
ν_{56}			286	294
ν_{39}	308	312	306	309
$2\nu_{59}$			348	349
ν_{38}			397	396
ν_{37}	474	480	467	462
ν_{36}	540	540	535	529
ν_{35}			583	581
$2\nu_{39}$	614	625	615	
ν_{34}	746	741	746	735
$\nu_{39+} \nu_{37}$			767	777
$2\nu_{38}$			803	792
ν_{33}	812	817	816	819
$3\nu_{39}$	920	937		

Comparison with the previous assignments of the S_1 vibrational features by Barber and Newby from their LIF study reveals broad agreement.[96] The majority of the previous band assignments match those detailed here, albeit with the frequencies offset approximately 30 cm^{-1} to the red, likely due to a difference in laser calibration between the groups.

Some assignments of weaker features, particularly those corresponding to the low-frequency modes do differ from the LIF paper, which used TD-DFT/B3LYP calculated frequencies as a basis for assignment. The current assignments are based on vibrational calculations of the excited state using RICC2, a level of theory shown to be of higher quality than DFT for these systems, and therefore are likely to be more accurate.[100]

There is one key feature of the REMPI spectrum that was not predicted at all by the *ab initio* work: the peak at 286 cm^{-1} relative to the *anti* origin peak. This is a relatively strong feature in the spectrum, but with no predicted normal mode frequencies, nor combinations or overtones in this region, it is a difficult element to explain. It was assigned to the *anti* conformer following the ZEKE analysis, but definite finer assignment was not possible. One possibility is that it is caused by an out-of-plane symmetry-forbidden excitation whose spectral intensity has been dramatically increased by Herzberg-Teller coupling, the phenomenon by which a symmetry forbidden transition appears strongly due to "intensity borrowing" of a vibronically coupled state.[101] It has therefore been tentatively assigned as the ν_{56} out-of-plane ring distortion, but this is strongly speculative.

The strongest features present in the REMPI spectra are all from the in-plane vibrations with A' symmetry, implying good wavefunction overlap due to both ground and excited state having planar geometries. Particularly strong features include the ν_{39} modes and the ν_{33} modes for each conformer, whose vibrations are depicted below.

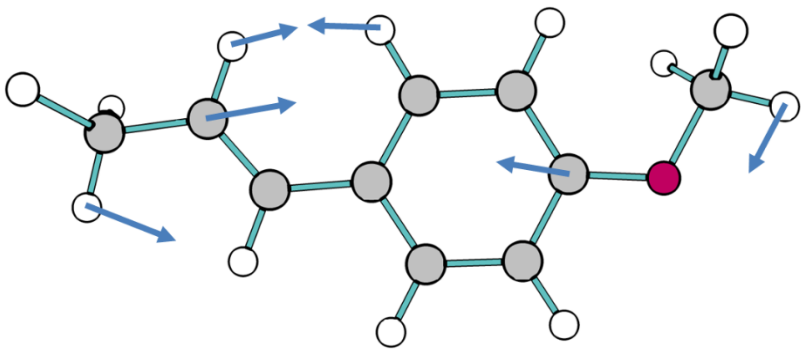

Figure 3-10: *Syn* ν_{39} mode displacement

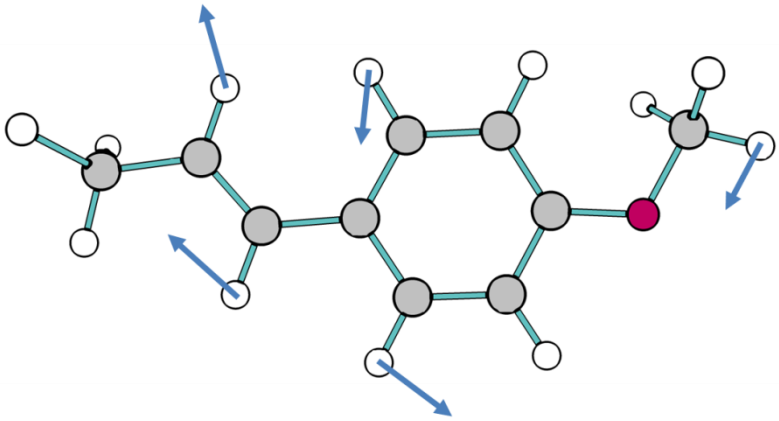

Figure 3-11: *Syn* ν_{38} mode displacement.

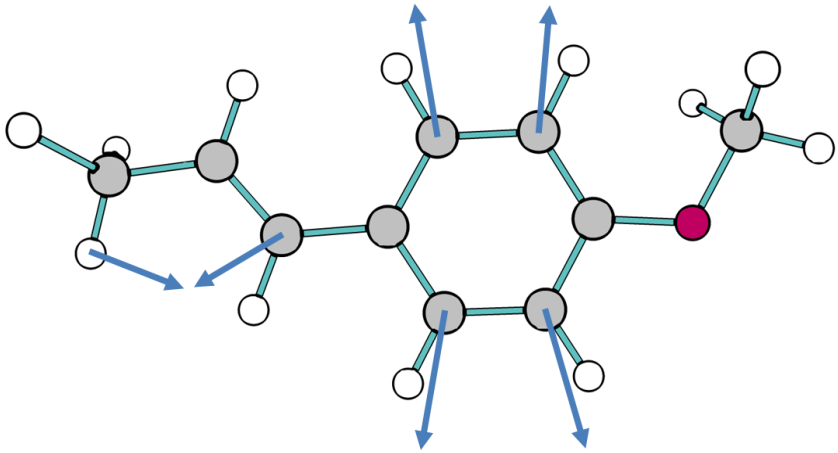

Figure 3-12: *Syn* ν_{33} mode displacement

The conformers differ spectrally, in particular, the intensity of the vibrational features relative to each conformer's origin peak are not the same. The *syn* conformer has, for the most part, stronger vibrational bands relative to its origin, indicative of a more pronounced change in geometry upon excitation along the coordinates that align with these vibrational modes.

The band assigned to the ν_{39} mode is stronger than the origin in the *syn* conformer. This suggests that *syn* anethole changes geometry more strongly along this coordinate than the *anti*, where the ν_{39} band is weaker than the origin. This has strong agreement with the simulated spectrum, which predicts a stronger ν_{39} feature in *syn* than *anti*. Now we see a difference in the conformational behaviour we must consider the excitations taking place.

The first excited state of anethole is predicted to be a ππ* state, consisting mainly of an electronic transition between the highest occupied molecular orbital (HOMO) and the lowest unoccupied molecular orbital (LUMO) π molecular orbitals.

The HOMO-LUMO excited state configuration is a larger component of the overall excited state character in the *syn* conformer compared to the *anti*, at 61 % and 48 % respectively. The majority of the remainder is made of the HOMO to the second π LUMO transition in both cases (14 % for *syn* and 24 % for *anti*).

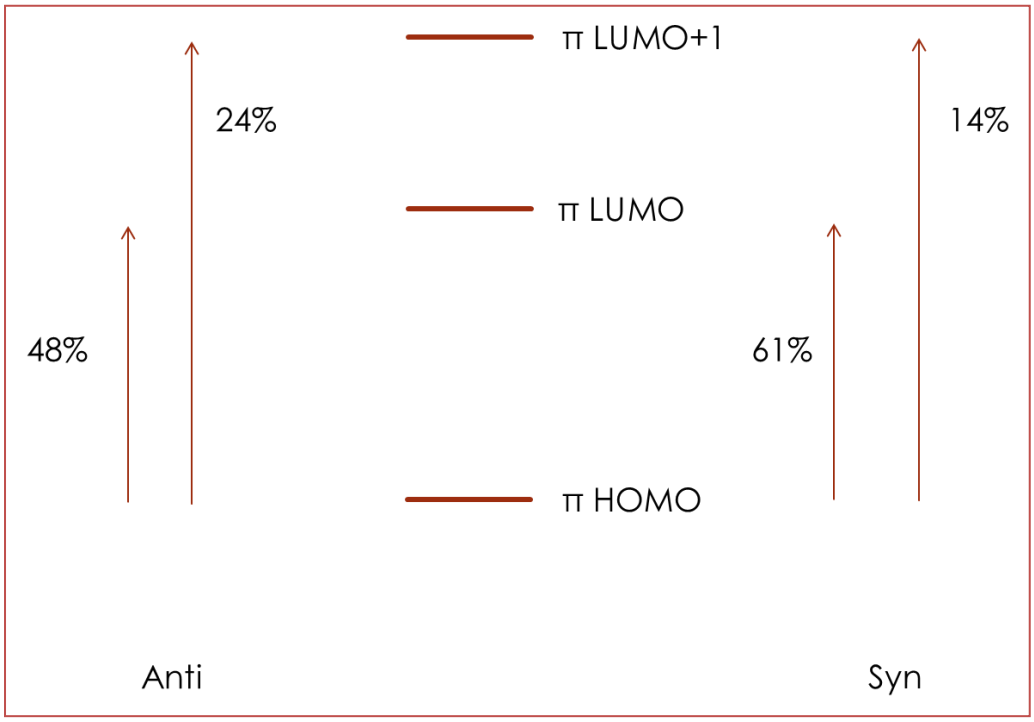

Figure 3-13: Calculated contributions to electronic excitation.

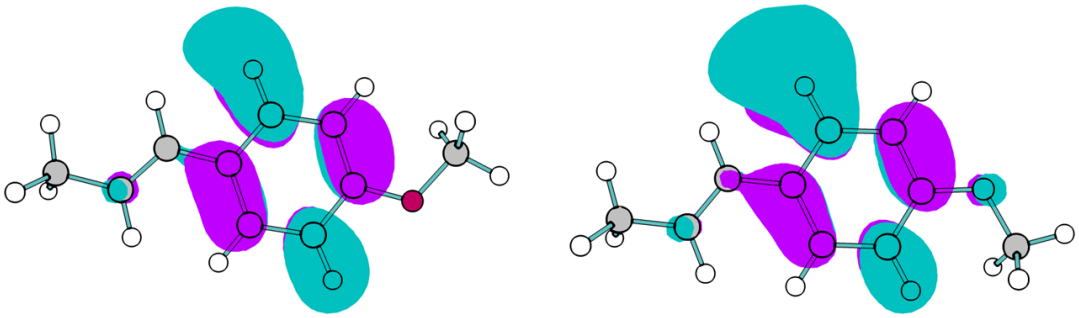

Figure 3-14:Anethole π LUMO +1 *anti* (left) and *syn* (right).

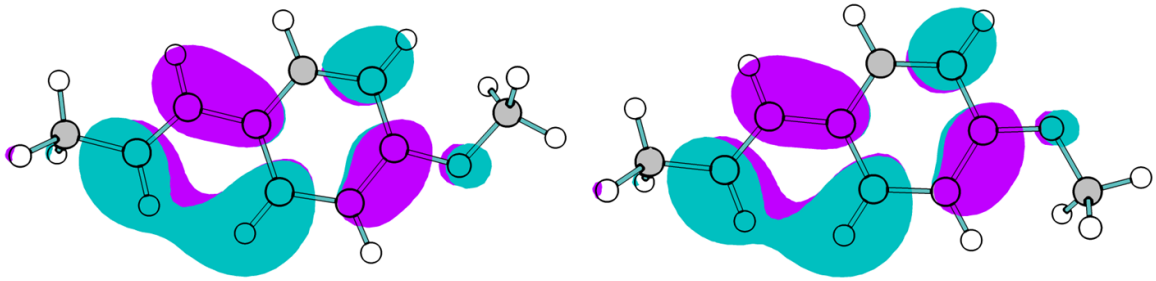

Figure 3-15:Anethole π LUMO *anti* (left) and *syn* (right).

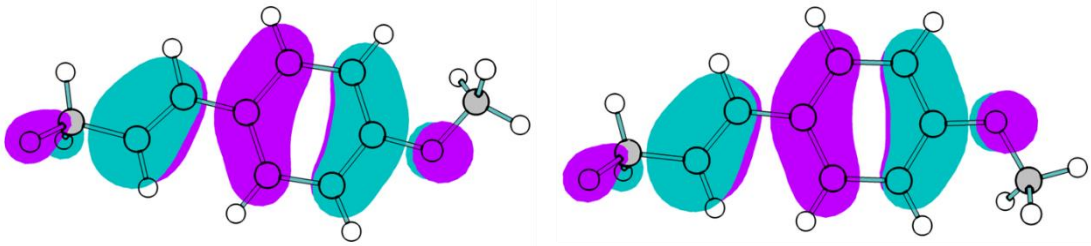

Figure 3-16:Anethole HOMO *anti* (left) and *syn* (right).

These MOs help explain the higher intensity features in the *syn* conformer, particularly from the ν_{39} mode. In essence, *syn* has greater π LUMO character in the S_1 state, which has bonding character between the propanyl group and the benzene C-H. Hence, there is stronger ring-C-H-propanyl bonding in the S_1 state and a reduction of the propanyl/benzene bond angle. This gives rise to a larger geometry change in this direction, and stronger features, particularly in the ν_{39} mode.

Both conformers show a strong vibrational progression of the ν_{39} mode, with features identifiable for the second and third overtone for the *syn* conformer, and the second for the *anti*. The spectrum ends before the expected *anti* third overtone, and the previous LIF paper did not report a third harmonic feature for the *anti* conformer,

suggesting weaker vibrational progression in the *anti*, due to less distortion in that direction.

The *anti* conformer meanwhile, shows in both the simulations and the experimental data to distort along the ν_{38} mode strongly, which the *syn* conformer does not. This could be explained for the same reason as the prevalence of the ν_{39} mode in the *syn* REMPI. ν_{38} is an antisymmetric bend of the two substituents, involving a stretch away from each other of the propanyl group and the benzene C-H. The *anti* conformer has less bonding character than the *syn* in this region as previously discussed, and hence the ν_{38} mode shows only in the REMPI of the *anti* conformer. This feature was perfectly predicted by the simulations, showing the efficacy of the RICC2 methods for these calculations.

3.4.2.1 Duschinsky mixing in anethole

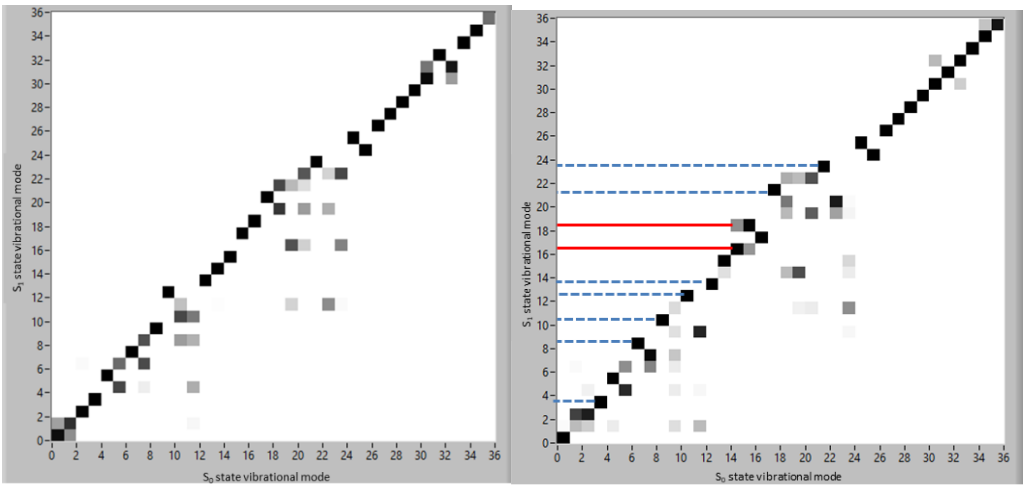

Figure 3-17: Duschinsky mixing of anethole S_1 state vibrations in the *syn* conformer (left) and *anti* conformer (right).

A Duschinsky analysis of the normal modes of the excited state shows significant mode mixing of many of the normal modes in the spectral region this work covers. Figure 3-17 shows the degree to which an S_1 vibrational mode is related to its ground state counterpart. Here, darker squares indicate a stronger correlation between modes. Pure S_1 state modes are those that contain a very similar character to a ground state analogue.

We see that many S_1 vibrations contain contributions from multiple ground state ones, as seen in rows with more than one square present. Interestingly, the normal modes that correspond to in plane vibrations, those with A′ symmetry, are in general extremely pure, as highlighted by the dotted lines. There is almost no mixing of vibrations in the *syn* conformer for these modes in the 0-1000 cm^{-1} region.

Seemingly only the lower symmetry A″ vibrations show an inclination to mix. However, due to their weak intensities in the REMPI spectrum, and therefore the lack of ZEKE analysis of these modes no further interpretation has been done.

The *anti* conformer has some differences though. There are two A′ vibrational modes that are a hybrid of two of the ground state versions: ν_{36} in the S_1 state is a 3:1 mix of ν_{36} and ν_{35} in the S_0 state. Similarly, ν_{35} in the S_1 state is a 3:1 mix of ν_{35} and ν_{36} in the ground. These are shown as normal modes 16 and 18 on the figure above, denoted by the solid red lines.

They both correspond to ring distortion vibrations and are strongly present in the REMPI spectrum. This suggests that mode mixing has no effect on the wavefunction overlap and the strength of the lines in the spectrum. What would have been interesting is to probe these modes using ZEKE spectroscopy, where we might expect to see strong features for both modes present, if the cation modes are strongly related to their neutral analogues, but unfortunately experimental time restraints rendered this unfeasible.

Overall, the results of our experiment matched very well with the calculations, giving us good confidence in our assignments and interpretations so far. RICC2 seems to be an excellent computational technique for the interpretation of excited state vibrational spectra.

3.4.3 ZEKE

3.4.3.1 ZEKE via the origin

The ZEKE spectra in Figure 3-18, recorded by pumping the respective S_1 state band origins for the two conformers, are both dominated by strong band origins corresponding to the $\Delta v=0$ transition. This suggests only a small change in geometry from the S_1 state upon ionisation.

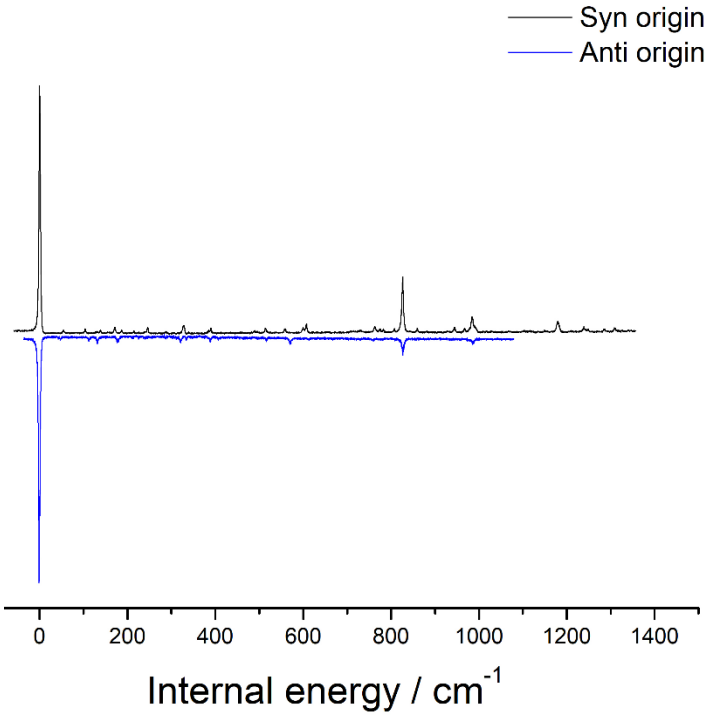

Figure 3-18: Origin pumped ZEKE spectra of both conformers.

The second strongest feature for both conformers is assigned to the vibrational mode, ν_{33}. This mode is a distorted ring breathing mode (see Figure 3-12) and it makes sense that upon ionisation, where the electron removed is from a π^* orbital, there is an increase in ring bonding strength that would be reflected in the ring contracting.

In both spectra the strongest features are all those with A' symmetry, i.e. those whose vibrations occur in the plane of the molecule, along with the overtones and combinations of vibrations with A" symmetry, whose products have A' symmetry. This in good agreement with the calculations and simulated spectra based on a planar cation.

Table 3-4: Origin pumped ZEKE assignments and RICC2 calculated vibrational frequencies

Mode	***Syn* frequencies / cm^{-1}**		***Anti* frequencies / cm^{-1}**	
	Experimental	D_0^+ calculated	Experimental	D_0^+ calculated
Origin	0	0	0	0
ν_{39}	329	328	320	283
ν_{33}	826	858	829	858
ν_{30}	984	995	985	992

The calculated vibrational frequencies of the ν_{33} mode are not as accurate as the S_1 analogues, overestimating the increase in frequency upon ionisation by about 30 cm^{-1} for each conformer. However, there is certainly some shift to a higher frequency when compared to the S_1 state, as seen in the spectra. This shift in frequency can be attributed to stronger C-C bonding in the ring in the ion state, giving a higher energy vibration of the ring expansion mode.

There are some differences in spectra between the two conformers: many modes appear with much greater intensity compared to the origin band in the *syn* spectrum, particularly the ν_{33} and ν_{30} modes. This is an indication that the *syn* conformer changes geometry more dramatically than the *anti* upon ionisation. This is to be expected as the ZEKE shows the partial reversal of S_0 to S_1 geometry changes upon removal of an electron from the antibonding π orbitals.

3.4.3.2 ZEKE *via* the S_1 ν_{39} mode

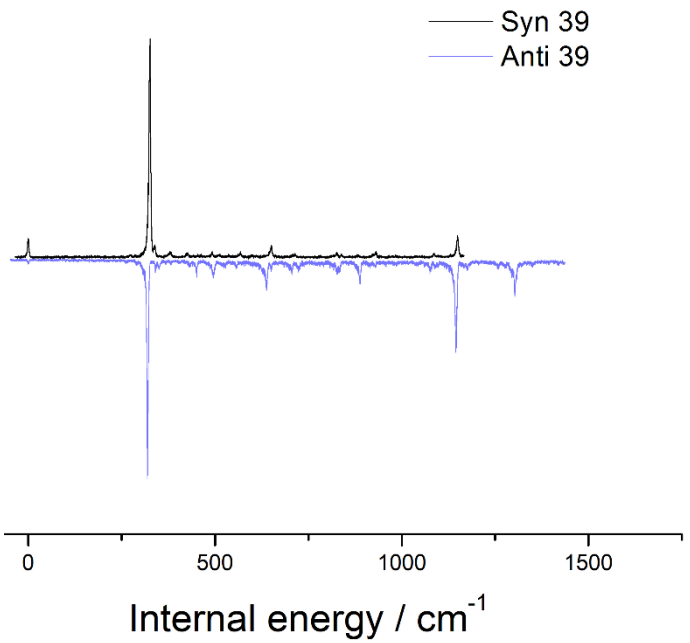

Figure 3-19: ν_{39} mode pumped ZEKE spectra.

Table 3-5: ν_{39} mode pumped ZEKE spectral assignments.

Mode	***Syn***	***Anti***
Origin	0	0
ν_{39}	325	320
$\nu_{41} + \nu_{39}$		451
$\nu_{40} + \nu_{39}$	568	557
$2\nu_{39}$	651	639
$\nu_{39} + \nu_{33}$	1150	1147
$\nu_{39} + \nu_{30}$		1302

Identification of many of the bands in the 39 mode-pumped spectra was performed by comparison with the origin pumped ZEKE. The majority of the features did not appear in the simulation, but are in fact a replica of the origin-pumped ZEKE spectrum, combined with one quanta of excitation of the ν_{39} mode. Once again, the ring breathing mode, ν_{33} is strongly present, due to the ring distorting upon ionisation.

The *anti* conformer ν_{39} mode-pumped ZEKE spectrum shows stronger intensities in the weaker features than in the origin pumped spectrum. Conversely, the *syn* conformer ν_{39} mode pumped ZEKE spectrum has a much more similar profile to its origin pumped spectrum. Only the ν_{33} feature is stronger in the ν_{39} pumped spectrum.

Interestingly, there are two clear vibrational modes appearing in the *anti* spectrum, at about 20 cm^{-1} and 30 cm^{-1} internal energy. Similarly, a feature is also present at 20 cm^{-1} in the *syn* spectrum, but no calculated vibrations appear in this region. However, if we expand the systems we are looking at a plausible explanation appears. The *syn* ν_{39} pumped spectrum uses a pump photon energy of 33229 cm^{-1}, corresponding to the ν_{39} peak in the REMPI spectrum. This almost exactly overlaps a feature on the argon-anethole cluster REMPI spectrum, which will be discussed in the next chapter. This band corresponds to the cluster version of the mysterious Herzberg-Teller peak, tentatively assigned to the *anti* ν_{56} mode in the anethole REMPI spectrum. It could be that we are simultaneously producing a *syn* ν_{39} pumped monomer ZEKE and a ν_{56} *anti*-argon cluster ZEKE. During the ZEKE experiment we lose the mass resolution we have in the REMPI, as electrons are being detected rather than ions, so the photoelectron products from different sources become indistinguishable.

The two peaks appearing in the *anti* ν_{39} ZEKE spectrum are less obviously assigned, but one speculative assignment could be that they are also due to accidental overlap of a band from either conformer or the argon complex.

Duschinsky analysis of normal modes in the ion

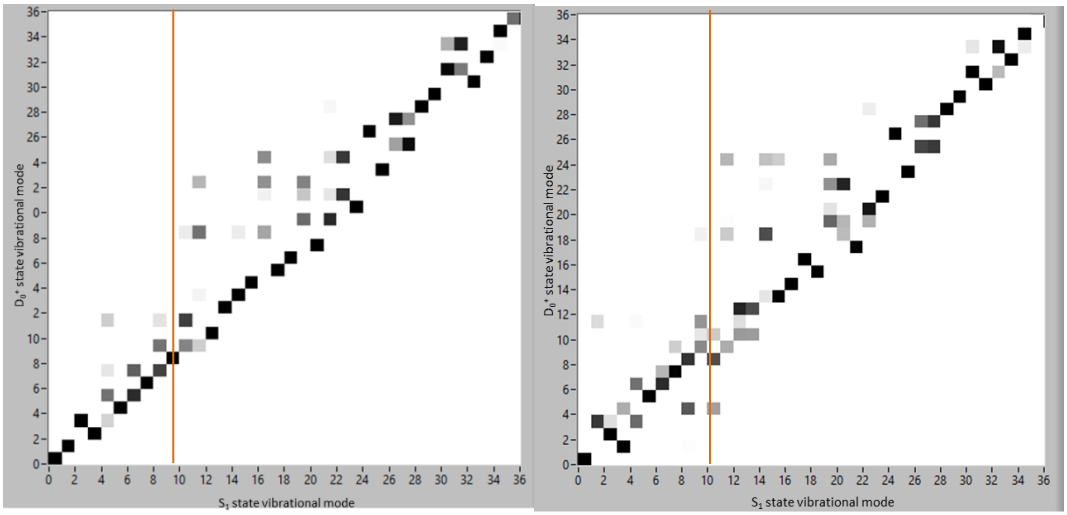

Figure 3-20: Duschinsky mixing of the *syn* (left) and *anti* (right) anethole cation vibrations.

The two conformers superficially appear to have similar levels of Duschinsky mixing as they transition from the S_1 to the D_0^+ state. However, some, small differences were present. The red line on each figure denotes the ν_{39} mode in the S_1 state. Squares that intersect with the line can be read as the equivalent modes in the cation. As can be seen, the *syn* conformer shows a straightforward, pure ν_{39} mode in the ion state. However, the *anti* conformer shows the ν_{39} mode to be a well-mixed vibration in the ion state, as seen by the many squares along the line.

The ion vibrational modes associated with the S_1 ν_{39} vibration in the *anti* conformer are represented in the figures below. The contributory modes are $\nu_{41,}$ ν_{40} and ν_{39}, which are illustrated in Figures 3-22 to 24. Peaks corresponding to the combination of ν_{39} and ν_{40}, and ν_{39} and ν_{41} are present and strong in the *anti* conformer ZEKE spectrum, so this mixing of states appears to be correct based on the experimental data.

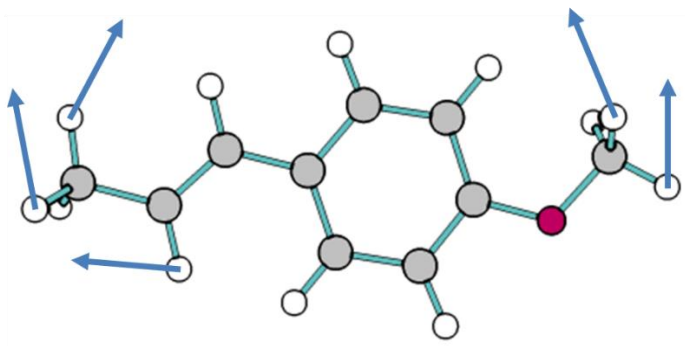

Figure 3-21: ν_{41} mode

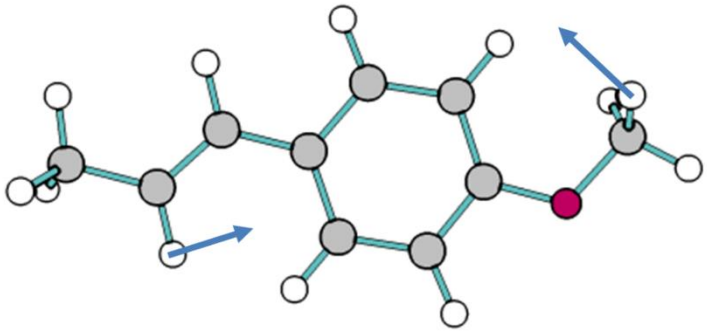

Figure 3-22: ν_{40} mode

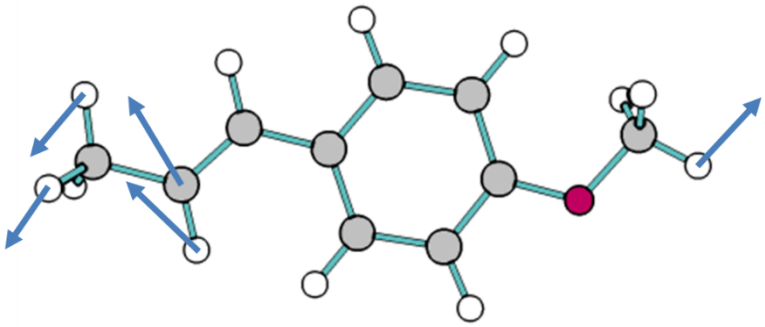

Figure 3-23: ν_{39} mode

3.4.3.3 ZEKE via the ν_{33} mode

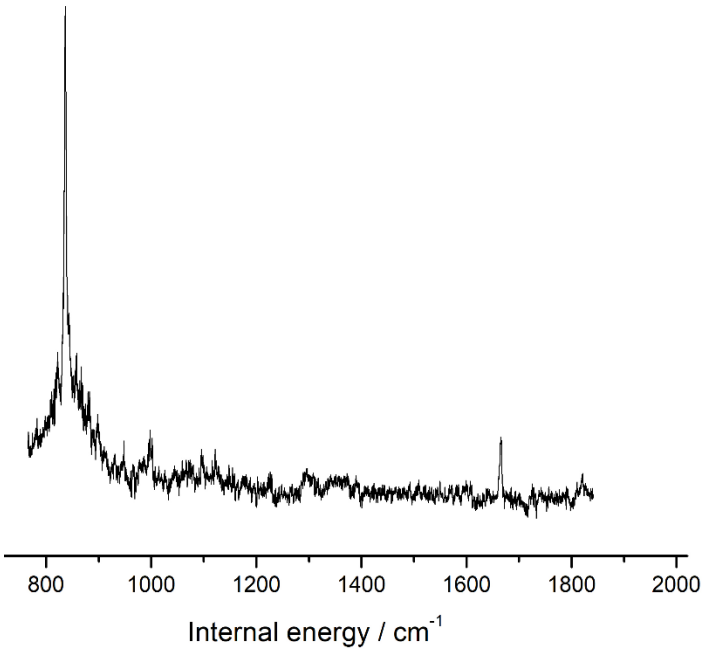

Figure 3-24: *Anti* ν_{33} mode pumped ZEKE spectrum.

Table 3-6: ν_{33} pumped ZEKE spectral assignments.

Mode	Frequency / cm^{-1}
$\Delta v = 0$	836
$\nu_{62+}\ \nu_{33}$	948
$\nu_{38+}\ \nu_{33}$	1225
$2\nu_{33}$	1664
$\nu_{30} + \nu_{33}$	1819

The ν_{33} mode pumped *anti* conformer ZEKE spectrum was recorded, but with a much poorer signal-to-noise ratio. Experimental limitations and the wide energy range needed to find the ionisation energy of such a high frequency pumped S_1 state, in addition to the interesting ZEKE features that might be expected, such as vibrational progression of the ν_{33} mode, were not overcome in a suitable time frame.

3.4.4 Geometry changes

The computational results thus far have explained well the main features of the experimental data collected. Exceptions were in accurately calculating the ion vibrational frequencies, and in the simulations of ZEKE spectra where a vibronic S_1 level was not ν=0 (shown in the appendix). Overall, the anethole system seems to be well described at the RICC2/aug-cc-pVDZ level of theory, and thus we can assume with some confidence that the remaining theoretical data is also accurate.

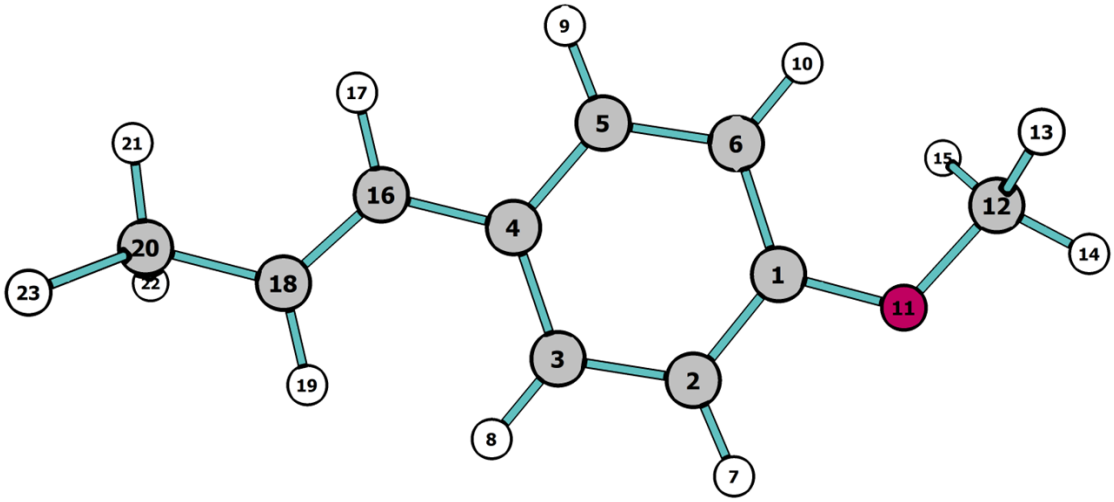

Figure 3-25: Anethole atom numbering system.

The geometries of the two conformers are here compared, as well as their differing behaviour upon excitation and ionisation. The full table of parameters is in the appendix.

Conformational differences:

S_0

In the ground state the *syn* and *anti* conformers have similar geometric parameters across most of the molecule. Bond lengths remain largely identical, but there are some slight differences in bond angles. Angle C2-C1-O11 and C6-C1-O11 see a difference of 9 ° between conformers, as the steric strain caused by the methyl group rotation expands the ring methoxy angle in the direction the methyl is pointing. This also has the effect of increasing the C1-C6-H10 and C1-C2-H7 angles by 3 ° to bend further away from the methoxy group. The same effect occurs if we view the conformational change as a propanyl torsional rotation, then the C5-C4-C16 and C3-C4-C16 angles are the ones adjusting.

S_1

Once again, the bond lengths of the two conformers remain very similar in the excited state. The difference in angles is also still very similar to the ground state

with the addition of a slight expansion of the C3-C4-C16 angle in the *syn* compared to the *anti*. This is mirrored in the smaller angle C5-C4-C16 in the *syn* conformer. This corresponds to the propanyl group moving slightly closer in towards the C5 atom in the *syn* conformer. This can be explained by looking at the molecular orbitals involved in excitation. The *syn* conformer has a higher electron density in the π LUMO, which has some bonding character between the C18-H19 and the C5-H9 groups, drawing them slightly closer together. This is the effect we saw in the strong *syn* ν_{39} mode in the REMPI spectrum. The antiphase character of the orbital across the C18-C16 bond also explains the slightly longer bond length here in *syn* compared to *anti*.

Ion

Continuing the theme, there is very little difference in bond lengths between the conformers in the cation state. The difference in the methoxy ring bond angle is more pronounced in the ion state at 9.4 °. This can be explained by looking at the HOMO. This orbital has antibonding character between the ring and the oxygen atom. When doubly occupied this results in a longer bond length, upon ionisation this bond shortens, and the ring-methoxy angle increases due to the increased steric strain of a bulky group that has now moved closer.

Electronic changes

S_0 to S_1 changes

Upon excitation there are significant geometry changes, which are manifested as prominent features in the REMPI spectrum. Foremost, there is an expansion of the ring system, a common feature of π to π* transitions, resultant of the movement of an electron from a bonding to an anti-bonding orbital. In fact, this change could be more accurately described as a stretching of the four unsubstituted carbons away from each other, with the substituted carbons slightly closing the distance between them. The internal angles of the substituted carbons increase from being fairly regular at 120 degrees in the S_0 state to 123 ° in the S_1. This is on the same level of distortion as fluorobenzene when calculated using the same level of theory.[102] Although the authors of that paper believe the change to be overestimated and a weakness in the *ab initio* work, that could be being replicated here. Whether the change is as strong as the calculations appear, it is certainly present, as seen in the strongest REMPI feature being assigned to the ring expansion ν_{33} vibrational mode.

Elsewhere, the C1-O11 bond lengthens slightly in both conformers, as an electron is removed from the anti-phase HOMO. This effect is more pronounced in the propanyl group, where C4-C16 also shortens for the same reason. The C1-O11-C12 angle also increases as the methoxy group stretches away from the ring system. Contrary to this the propanyl group bends inwards toward the ring, as the C5-C4-C16 and C4-C16-C18 angles decrease, pulling the C18 towards C5 as the bonding character between them increases.

Interestingly, there is a small, but distinct difference between conformers upon excitation to the S_1 state. The *anti* conformer loses some planarity across the benzene ring. Dihedral angles between the benzene hydrogens and the propanyl group increase from 0.01° to 0.26 °, a small, but substantial change. Comparatively, the *syn* conformer does not change planarity at all, remaining at 0.00 Å.

S_1 to ion changes

The removal of an electron from an antibonding π orbital causes the decrease in C-C bond lengths around the ring system as bonding character increases. The hexagon also become more regular, as the stretches from the S_0 to S_1 transition are reversed somewhat. All internal angles are now between 118.5 ° and 121 ° for both conformers, compared to 117.3 ° and 123 ° for *syn* S_1 and 116.5 ° and 123 ° for *anti* S_1. This explains the strong ν_{33} features we see in the origin pumped ZEKE spectra. The *anti* conformer and *syn* conformer are both entirely planar once more, with all ring dihedral angles 0.01 ° or smaller. It therefore can be assumed that the change in planarity for the *anti* conformer upon excitation is entirely due to the occupied molecular orbitals associated with the S_0 to S_1 transition.

3.5 Conclusions

The *ab initio* work performed on anethole generally agrees very favourably with the experimental data collected. We see differences in the vibrational structure between the conformers, which is clearly explained through examination of the excitations taking place. Small differences in the electronic configuration of the S_1 state between conformers had strong effects on their spectra, where we saw more significant geometry change for the *syn* conformer than the *anti*. The conformers also displayed varying levels of Duschinsky mixing, where the *syn* conformer seems to have little change in the description of the vibrations upon excitation and ionisation, compared to the ground state. Conversely, the *anti* vibrations are more frequently mixed upon excitation and ionisation, giving mixed character normal modes that are reflected in a busier ZEKE spectrum when further probed, as we see geometry changes that are reflected across multiple vectors.

Chapter 4. The anethole-argon complex

4.1 Introduction

The internal cooling that results from the seeding of a target molecule into a supersonic jet described in Chapter 2 provides the additional benefit in that it facilitates the formation of small clusters of atoms and molecules, held together by weak, non-covalent interactions. Weakly-bound complexes are a versatile and crucial area of study; understanding the ways solvents bind to and around a target molecule gives us a window into studying the initial steps in the transition from gas to solution phase, as well as insights into solvation. The conduct of such studies in the gas phase provides a means to obtaining spectra with vibrational and potentially rotational resolution, including the vibrational fine structure associated with intermolecular vibrational modes. Such finely-grained spectroscopic detail would be unavailable in any solution-phase study. The present work builds on the results of the previous chapter whose focus was on the anethole monomer. In this chapter, REMPI and ZEKE spectroscopy will be used to study how a single argon atom binds to anethole in the anethole-argon van der Waals complex and how the strength and nature of that bonding changes upon electronic excitation and ionisation.

Non-covalent interactions are notoriously difficult to study computationally, due to the relatively weak forces that hold the molecules together. However, their importance in chemistry has made them an incredibly interesting field and much work has gone into refining computational methods for their study.[25, 26, 103] As models of the initial stage of the solvation process, such clusters can provide a route to a better understanding of the behaviour of a molecule in a solvent and in particular how the growth in size of a cluster with increasing numbers of solvent species provides insight into the structure of solvation shells. The combination of computational and experimental studies additionally provides a means to benchmark computational approaches whilst also increasing our knowledge of the system being studied.[104]

The conformational flexibility of the parent anethole molecule described in the previous chapter offers an interesting prospect of observing the different binding motifs and resulting perturbations to the parent that result when solvating the different conformers with an argon atom. Previous studies have shown that even a small geometry change involving internal rotation of a substituent can have strong effects on the properties of the species, such as widely varying ionisation energies and rotational constants in the case of the n-butylbenzene molecule, previously studied with ZEKE spectroscopy.[105]

Aniline is another aromatic molecule that forms van der Waals complexes with argon as two stable conformers, differentiated by the hydrogens of the non-planar

NH_2 group angled either towards or away from the argon atom sat above the ring. It was shown by López-Tocón *et al.* that this small conformational change can alter the binding energies by 14 cm^{-1} and the binding site of the argon atom by 0.1 Å.

The anethole-argon cluster was studied using one- and two-colour REMPI and ZEKE spectroscopy. Geometry optimisations, frequencies and binding energies calculations have been performed using *ab initio* methods to assist with analysis of the results and to aid in the spectroscopic assignments. Simulated REMPI and ZEKE spectra have been computed, using FC-LABII.[102]

4.2 Experimental

4.2.1 REMPI and ZEKE

Anethole was obtained from Fisher Scientific at a purity of 99% and used without further purification. It was introduced to the vacuum chamber with no additional heating, using argon backing gas at a stagnation pressure of 0.6 bar. It entered the vacuum chamber through a Parker Series 9 general pulsed valve operating at 10 Hz, as a supersonic free-jet expansion. The expansion passed through a 2 mm diameter skimmer into the interaction chamber, whereby it was intersected by the output of two tunable, frequency-doubled, dye lasers. Vacuum pressures in the laser interaction chamber were kept at 1.1 x 10^{-7} mbar throughout the experiments using Pfeiffer Hipace 700 Turbopumps that differentially pumped the two chambers. Upon ionisation, the photoions were accelerated along a 22 cm flight tube to a multi-channel plate detector. The recorded time-of-flight provides the means to determine the relative masses of the ions impacting on the detector, thereby effectively yielding a time-of-flight mass spectrum.

The output of a frequency doubled radiant dyes narrowscan dye laser, was scanned from 306 nm to 295 nm using a 1:1 mixture of DCM and Sulforrhodamine B dyes in ethanol. The probe (ionisation) photon was generated using DCM dye in ethanol from a Continuum Jaguar dye laser, giving a frequency-doubled output of 315 nm.

Once the REMPI spectrum was obtained, selected wavelengths from the spectral peaks were used to probe the origin ($\Delta v=0$) levels as a pump point for the acquisition of ZEKE data. The peaks initially assigned to the *syn* and *anti* conformer origins at 32837 cm^{-1} and 32908 cm^{-1} were used as ZEKE pump wavelengths. The scanning photon was the frequency doubled output of a Jaguar dye laser using Pyridine 1 in ethanol.

Pulsed field ionisation was initiated using a weak discrimination pulse of negative polarity to remove the high energy electrons that have been ejected from the molecular beam upon ionisation. A repeller pulse was delivered slightly later, and the resulting ZEKE electrons were detected by MCPs.

Data was acquired using a ten-shot average of each point, scanning in 0.005 nm steps.

4.2.2 Computational

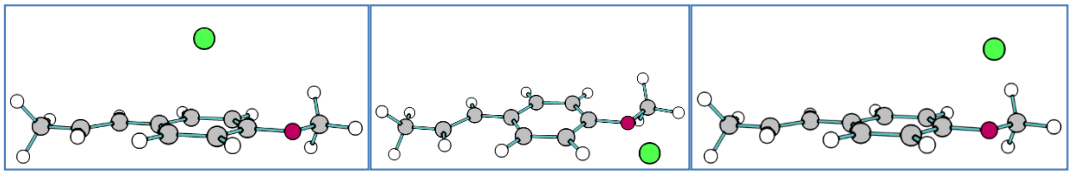

Figure 4-1: Starting geometries for optimisation of the anethole-argon complex.

The complex geometries were optimised, and their vibrational frequencies calculated in the S_0, S_1 and D_0^+ states using *ab initio* methods. Turbomole 6.4 was used at the RICC2 aug-cc-pVDZ level of theory with counterpoise correction. Several starting geometries were used to investigate various potential argon binding sites, as seen in Figure 4-1: directly above the ring (left), in the plane of the molecule, adjacent to the oxygen atom (middle), and above the oxygen of the methoxy group (right). Both *syn* and *anti* conformers were studied, as in the previous chapter. Franck-Condon calculations were conducted for transitions between the S_0 ground and S_1 excited state to simulate the REMPI spectrum, and between S_1 and D_0^+ states to simulate the ZEKE spectra, with one set of each for each conformer. FC-LabII was used to calculate the Duschinsky mixing and to simulate spectra.

The anti-anethole-argon in the cation ground state proved impossible to optimise fully at this level of theory without producing imaginary vibrational frequencies. Both conformers were therefore studied additionally using DFT with a wb97x-v functional specifically selected for its suitability at modelling van der Waals interactions, using an aug-cc-pVDZ basis set.

The breakdown of the contributions to binding in weakly bound substances was obtained from a Qchem analysis, in collaboration with Dr Cate Anstöter.[71]

Anethole is predicted to be planar in all three calculated states, (S_0, S_1 and D_0^+). As a complex the symmetry plane is removed and it belongs to the C_1 point group, with only one irreducible representation. All vibrations will therefore be allowed under the electronic selection rules as the direct product of the dipole moment operator in the x, y, or z direction will always be fully symmetric.

4.3 Results

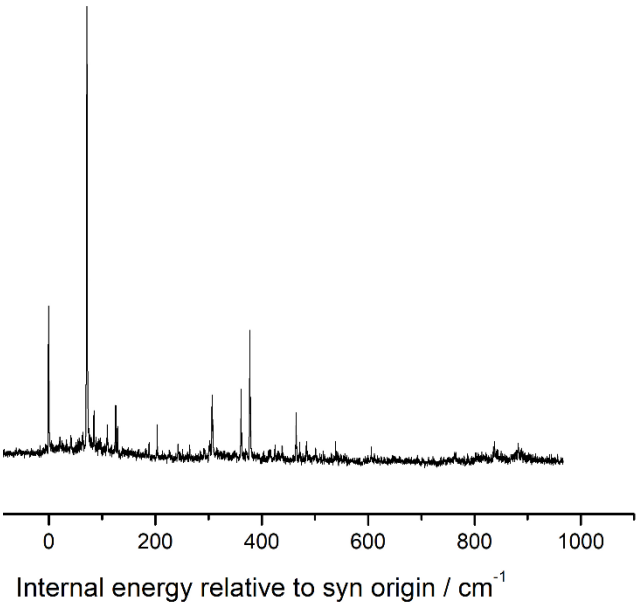

Figure 4-2: Two-colour anethole-argon REMPI spectrum.

The anethole-argon REMPI spectrum shows a now-familiar pattern of two conformational isomers, their origin peaks at 32869 cm^{-1} and 32941 cm^{-1} assigned to the *syn* and *anti* conformers respectively. There is some significant vibronic activity seen, with particularly intense features at 307 cm^{-1}, 361 cm^{-1} and 378 cm^{-1} internal energy. This is indicative of some moderate geometry change occurring upon excitation, although as the peak intensities are somewhat less than their respective origin peaks, the change is not thought to be very dramatic.

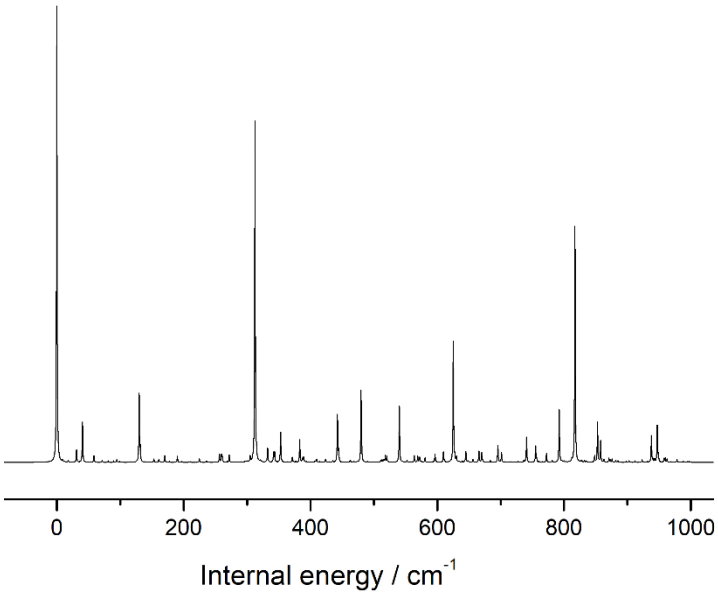

Figure 4-3: Simulated REMPI spectrum of the *syn* conformer anethole-argon complex.

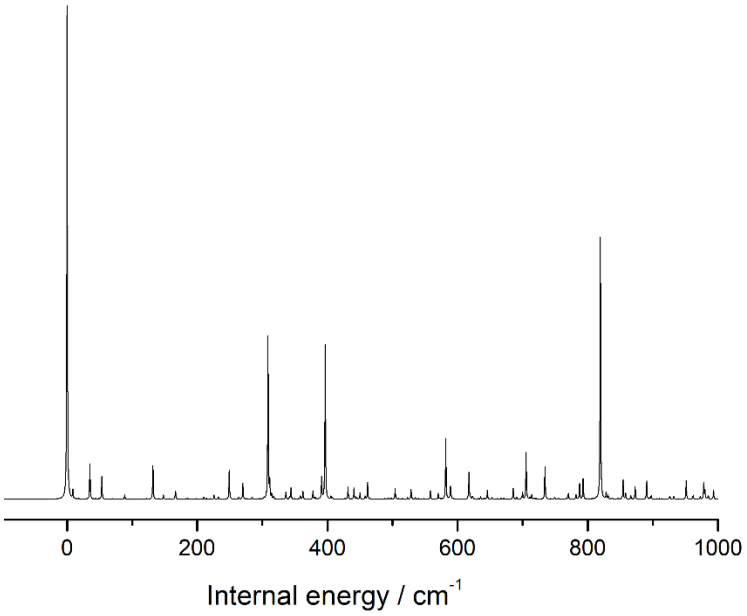

Figure 4-4: Simulated REMPI spectrum of the *anti* conformer anethole-argon complex.

Similarly to the monomer, the simulated cluster spectra in Figure 4-3 and Figure 4-4 predict several dominant lines in the REMPI spectrum, all belonging to in-plane vibrational modes. The *syn* conformer shows a strong propensity to distort along the ν_{39} vibrational coordinate, whilst the *anti* conformer is additionally expected to distort along the ν_{38} and ν_{33} modes, as the complex undergoes the $S_1 \leftarrow S_0$ transition.

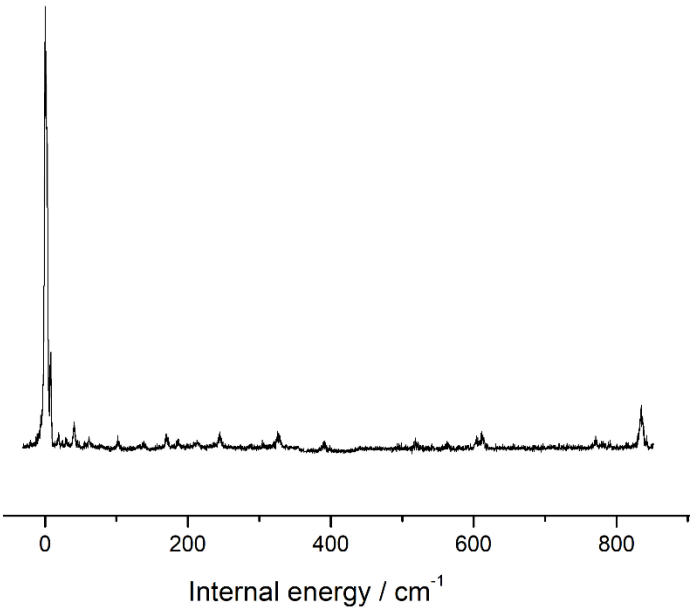

Figure 4-5: *Syn* anethole-argon complex ZEKE.

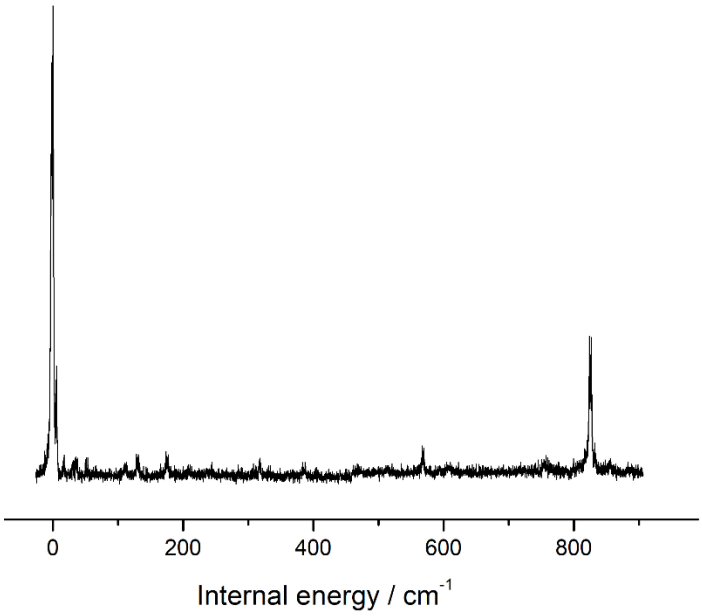

Figure 4-6: *Anti* anethole-argon complex ZEKE.

The ZEKE spectra of the anethole-argon complex show less vibrational activity than the REMPI does, suggesting a lesser amount of geometry change during the $D_0^+ \leftarrow S_1$ transition than the $S_1 \leftarrow S_0$. Both conformers are initially seen to show similar features; both show that the strongest geometry distortion occurs along the vibrational coordinate found approximately 820 cm^{-1} above the origin. A ZEKE spectrum was also simulated for the origin pumped S_1 state for the *syn* conformer only, seen in Figure 4-14 below, but the *anti* conformer could not be optimised in this state using software compatible with the simulation package, and thus no *anti* conformer ZEKE simulation is provided.

4.4 Analysis

4.4.1 REMPI spectrum

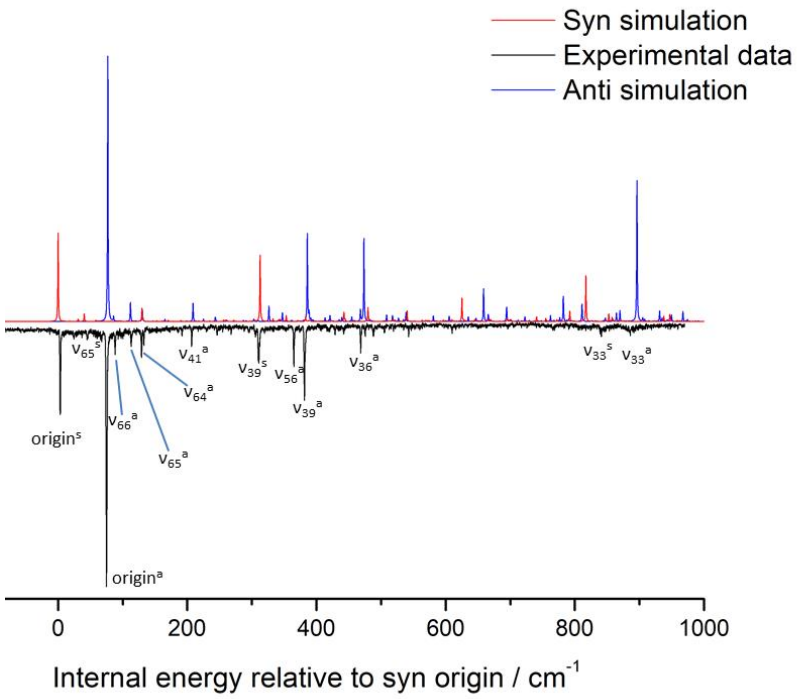

Figure 4-7: Experimental (lower) vs simulated (upper) two-colour REMPI spectrum of argon-anethole.

The simulated REMPI spectra of each conformer were combined, using a weighting of 3 to 1 *anti* to *syn* intensity based on relative intensities of the two experimental origin features. This simulation gives excellent agreement with the two-colour REMPI recorded as seen in Figure 4-7.

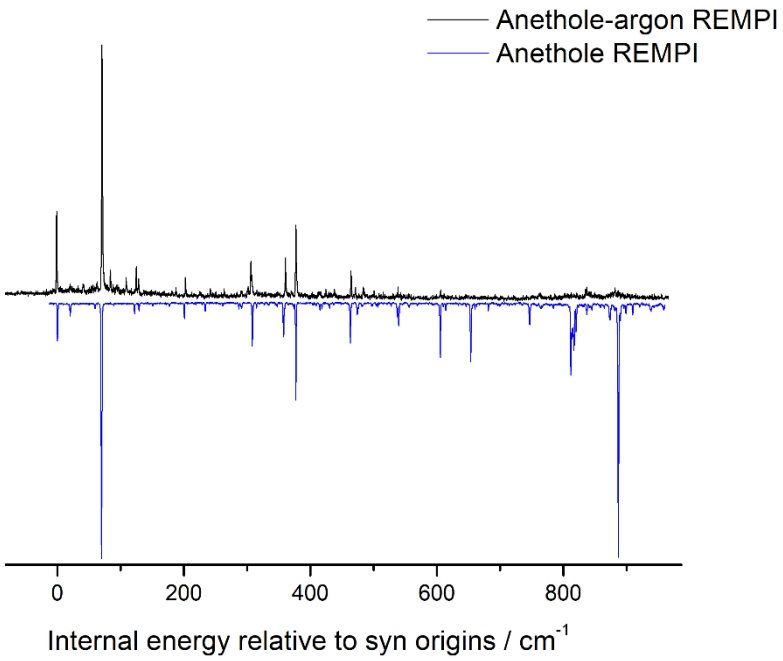

Figure 4-8: Comparison of the anethole-argon (top) and anethole monomer (bottom) REMPI spectra.

Figure 4-8 shows the REMPI spectra for both the monomer and cluster experiments. Here, they have been aligned respective to their relative *syn* origin peaks to aid comparison of monomer to complex. In fact, for the complex, both origin bands are red-shifted by 53 cm $^{-1}$ compared to the monomer. This indicates a stabilising force on the S_1 state in the presence of an argon atom, as the $\pi\pi^*$ state binds more strongly to the argon atom than the ground state does. The explanation for this is examined in the section below on excitations.

Most of the strongest features of the monomer are present in the complex REMPI spectrum. This indicates that there is no strong geometry rearrangement upon complexation, which is reasonable to expect with such an inert solvent atom. The characters of the vibrations are also extremely comparable, with the exception of ν_{38}, which is discussed below.

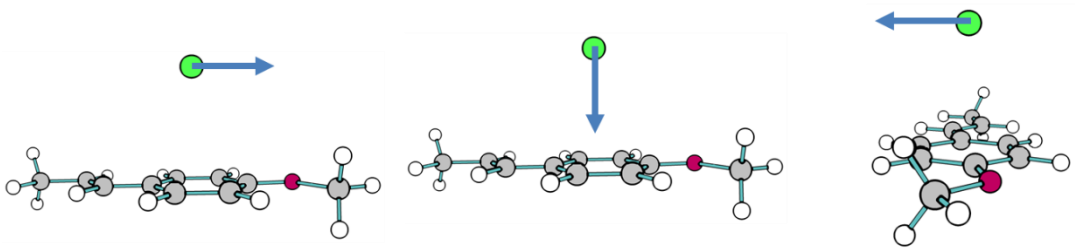

Figure 4-9: Intramolecular vibrational modes of the anethole-argon complex. From left to right: ν_{66}, ν_{65}, ν_{64}.

The clusters do however show a series of additional, low-amplitude, intermolecular modes not present in the monomer spectrum. Modes ν_{66}, ν_{65} and ν_{64} are assigned to the new vibrational features and relate to the translation of the argon atom with respect to the anethole, (ν_{66} and ν_{64}), and the intermolecular distance stretch of the argon atom, ν_{65}. The presence of these modes in the spectrum suggests a shift in the position of the fragments relative to each other upon excitation.

Besides the intermolecular modes the vibrations present in the spectrum are all in-plane. This indicates that the geometry changes occurring upon excitation can be partitioned into two categories: one that relates the two monomers spatially, and another group of in-plane distortions of the anethole molecule. There is no suggestion of a dramatic change of binding site upon excitation. Crucially, the van der Waals stretch is strong for both conformers indicating a change in intermolecular distance upon excitation, reiterating that there is a strengthening in the intermolecular interaction in the S_1 state compared to the S_0.

The two-colour REMPI spectrum of anethole-argon is of lower quality than the monomer counterpart. This is a symptom of the very concept we are studying. In the molecular beam under these experimental conditions there is an order of magnitude fewer clusters being formed than monomer particles, as seen in their relative time-of-flight signal intensities, so a correspondingly weaker signal-to-noise ratio is also to be expected. In addition, these complexes are very weakly bound and therefore are liable to fragment even with the relatively small absorption of energy supplied by two photons. We see a tailing off of signal intensity as we reach the higher energy wavelengths, this suggests that the binding energy of the complex is of the order of 500 cm^{-1}, a value that is consistent with our calculated S_1 state binding energy of 640 cm^{-1}. Above this point only the strongest features from the monomer spectrum are still visible for the cluster.

The bands have been assigned in Table 4-1 below. Whilst the addition of an out-of-plane argon atom breaks the Cs symmetry of anethole, the resulting perturbation to the forms of the intramolecular vibrations of anethole is weak and so it is reasonable to label the intramolecular modes using the same symmetry labelling as for anethole, to allow a straightforward comparison.

Table 4-1: REMPI spectral assignments of the anethole-argon cluster

	Syn		***Anti***	
	exp.	calc.	exp.	calc.
Origin	0	0	0	0
ν_{66}	6	9	13	9
ν_{65}	20	31	38	35
ν_{64}	41	59	53	40
ν_{41}	129	132	131	132
$2\nu_{60}$			289	314
ν_{39}	306	309	309	309
ν_{38}	391	383	394	396
ν_{36}	538		534	529
ν_{33}	837	817	810	819

The two colour REMPI spectrum of the anethole-argon complex shown in Figure 4-2 shows a repeating set of features indicative of both *syn* and *anti* conformer clusters being present. There are two strong origin bands and several other strong vibrational features. This suggests some meaningful change in geometry upon excitation in the direction of the normal modes associated with these features.

The lines associated with the *anti* conformer appear with greater intensity than those associated with the *syn* conformer. Although the intensity of the origin bands is less different this time than for the monomer, with the *syn* intensity around a third as strong as the *anti*, compared to a fifth for anethole. However, this could be a case of saturation in the *anti* origin peak, as suggested by an uneven baseline. I therefore believe this shows that there is not a dramatic change in conformational population upon complexation.

The strongest vibrational feature to higher energy of the band origin is that associated with the ν_{39} mode fundamental, once again more significant in the *syn* conformer than the *anti*. Looking at the excitations in the section below it is expected that this is for the same reason of increased bonding between the propanyl group and ring system for the *syn* conformer. The ν_{39} mode is a very pure version of its ground state analogue, with almost no Duschinsky mixing present, and presents in the spectra in the same manner as the monomer.

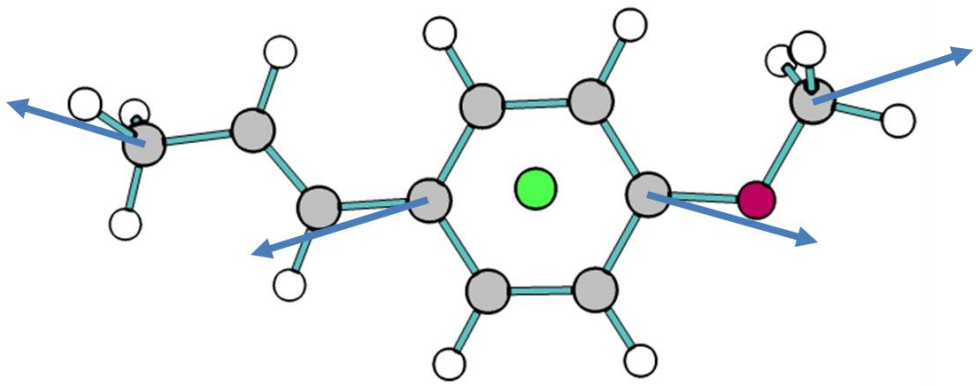

Figure 4-10: ν_{39} mode for the *syn* conformer

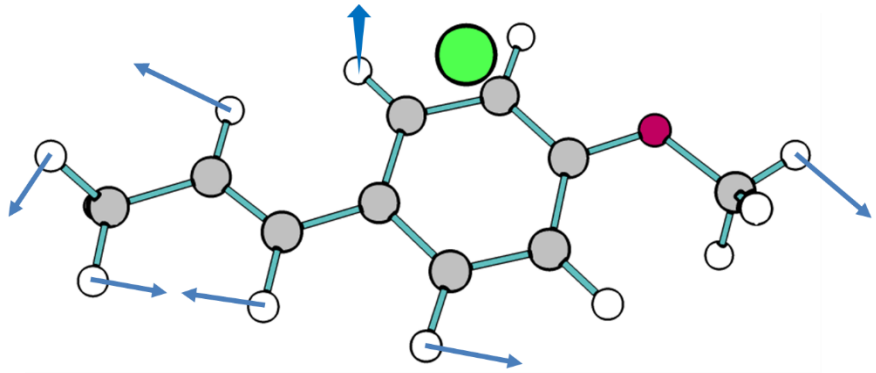

Figure 4-11: ν_{38} mode in the S_1 state for the *anti* conformer.

The ν_{38} mode is also strongly represented, but for the *anti* monomer only. There is a small amount of mixing in the S_1 state of this mode, with the out-of-plane ring distortion mode ν_{58} of the ground state contributing around 10% in both conformers in the S_1 state. The ν_{38} mode has changed quite significantly from the same mode in the anethole monomer. Calculations show an out-of-plane motion of the ring hydrogen that neighbours the propanyl group, in contrast to the in-plane movement of all the other atoms. This perpendicular motion is very strong in the argon cluster for both conformers, and present very weakly in the *anti* monomer, but, it is not at all present in the *syn* monomer. It appears the presence of an argon atom attracts the hydrogen up out of the plane, but this vibrational feature is only present for the *anti* conformer in both monomer and complex spectra. This is suggestive of a stronger change in the angle between the ring plane and the hydrogen atom in the *anti* conformer compared to the *syn*.

The ν_{33} mode is assigned to the bands at 837 cm^{-1} and 810 cm^{-1} for each conformer. Whilst very weak features in the spectrum compared to the origin, they are the only key features that are clear past 500 cm^{-1}, and I theorise that they would be stronger if the signal intensity had not dropped so substantially by this point. I expect that, as in the monomer spectrum, the ring expansion mode is still significant in terms of geometry change upon excitation.

4.4.2 ZEKE spectra

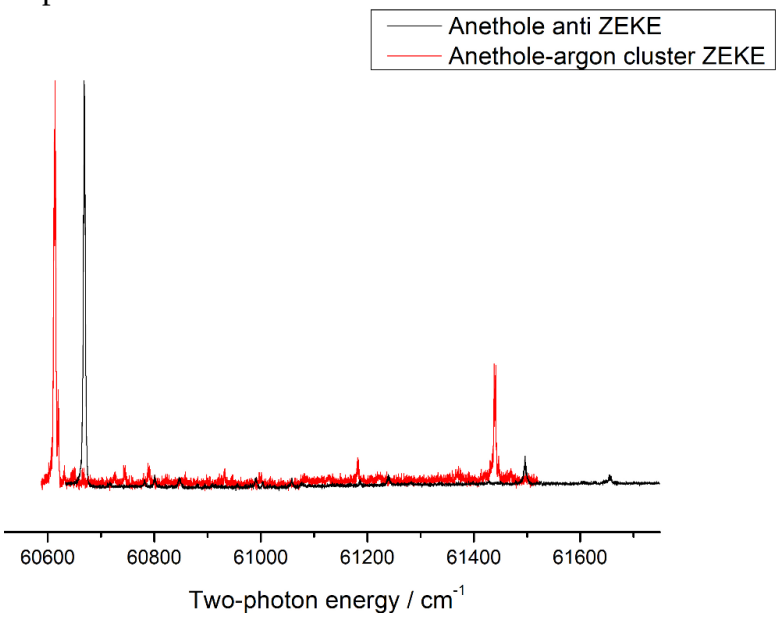

Figure 4-12: Origin pumped ZEKE spectra of *anti*-anethole and the *anti*-anethole-argon complex.

Comparing the ZEKE to the REMPI, we see clear features around ~850 cm^{-1} in the ZEKE, whereas many features in the REMPI predicted to be strong at the ~800 cm^{-1} mark are very weak. This indicates that in the ion state the argon is more strongly bound, meaning more excess energy is needed before it fragments. This is confirmed in Figure 4-12, which shows the red shift of the complex compared to the monomer. This is supported by a higher calculated binding energy in the cation complex, discussed further in section 4.4.6. This is interesting as it allows us to see the continued importance of the ν_{33} mode in the cluster.

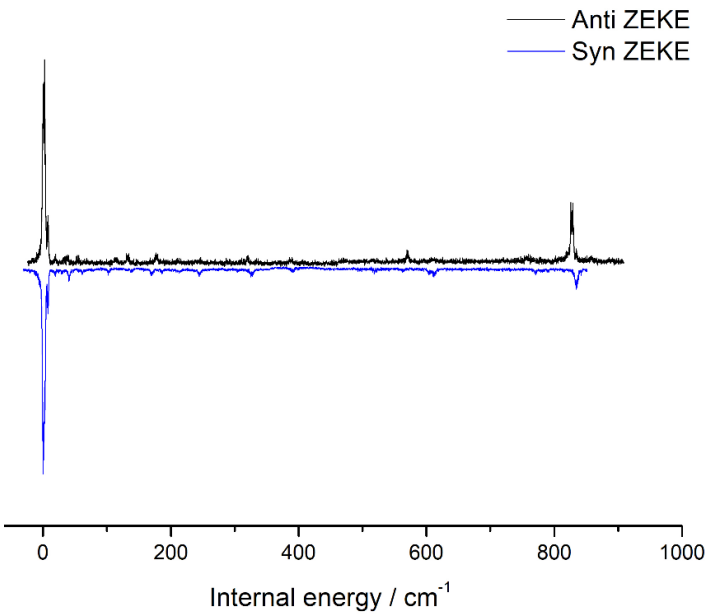

Figure 4-13: *Anti* (top) and *syn* (bottom) origin pumped ZEKE spectra of the anthole-argon complex.

The *anti* anethole-argon cluster seems to have a stronger geometry change along the ring expansion coordinate, ν_{33} upon ionisation, than the *syn*, seen in the more intense features in the origin pumped ZEKE compared to the ν=0 peak. This indicates a stronger ring contraction upon loss of the electron. The two conformers are broadly comparable elsewhere, suggesting their geometries respond in a similar fashion upon ionisation. This is different to the monomer results, where the *syn* showed more change upon ionisation. However, the raw signal intensity was much greater in the monomer data collection, due to the higher prevalence of the monomer in the molecular beam, so it could well be that we are simply missing the weaker features in the cluster spectra.

Table 4-2: Key ZEKE assignments in origin pumped modes.

Mode	***Anti* frequencies / cm^{-1}**	***Syn* frequencies / cm^{-1}**	
	Experimental	Experimental	RICC2 D_0^+
Origin	0	0	0
ν_{66}	5	8	7
ν_{65}	17	19	26
ν_{64}	40	41	52
ν_{41}	111	102	108
ν_{40}[1]	244	244	250
ν_{39}	317	326	327
ν_{38}	384	390	392
ν_{35}		611	628
ν_{34}	755	771	760
ν_{33}	827	834	850

[1] This mode is no longer a strictly in-plane mode, but a well-mixed out of plane one in the ion state.

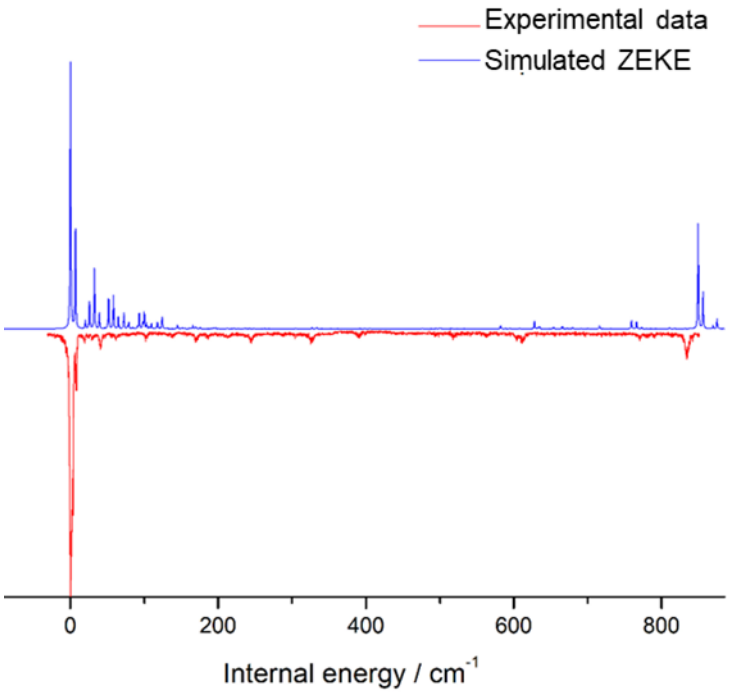

Figure 4-14: Simulated origin pumped ZEKE of *syn* conformer compared to experimental data.

For the *anti*-anethole-argon ZEKE spectral simulations, the RICC2 results with one imaginary frequency were used, due to the limited input formats available in the FCLAB-II software, but with the negative frequency changed to a positive. The literature shows the presence of imaginary frequencies in these sorts of systems to be almost inevitable in some cases, and as the geometry was strongly comparable to the true minima calculated using DFT it may be reasonably concluded that the imaginary frequency is not prohibitively worrisome.

The simulated ZEKE spectrum does not reproduce the experimental results as reliably as the monomer counterpart. Weakly bound complexes are notoriously difficult to model computationally, it was far more difficult to find a stable geometry in the ion state than any of the other systems studied, the presence of imaginary vibrational modes, indicating that transition states are being computed rather than true minima was common. Van der Waals complexes often have very shallow potential energy surfaces, which likely explains the poor predictive quality of the simulations, it is possible that the calculated geometry is not quite right, and is thus showing poor Franck-Condon terms.

4.4.3 Complexation

The spectroscopic results presented in this chapter follow on from the preceding one. Most spectral features, including the differences between the different conformers remain broadly the same. The biggest change is in the intermolecular modes now

present due to addition of the argon atom to the system. It is critical, therefore, to ascertain how and where the argon atom binds to anethole.

Where a solvent binds to an aromatic molecule depends on the shape, size, and presence of heteroatoms on the individual monomers. A typical binding site in substituted aromatics when complexing with noble gases is often above the ring in a π-bound conformation, where the delocalised π-electrons induce a dipole in a polarisable atom.[104, 106-108] Alternatively a solvent such as water may bind in the plane of the ring, localised near to a heteroatom, for instance in a hydrogen bonding type arrangement.[20] Finally, a solvent may bind localised away from the ring entirely, on a substituent that is more attractive to the solvent than the π system.

To this end starting geometries were set up that positioned the argon atom in each of these three positions, and all of them eventually converged to an above ring structure, for both *syn* and *anti* conformers of anethole, and in all three states, S_0, S_1 and D_0^+. Strong dispersion forces between the π electrons and the polarisable argon atom, and in the case of the ion, charge-induced dipole interactions, keep it anchored above the ring.

It was for this geometry that the REMPI and ZEKE simulations were conducted.

The Duschinsky analysis of the S_1 vibrational states shows similar mixing upon complexation to the monomer, as seen in Figure 4-15, particularly concerning the out of plane modes, which are thoroughly mixed throughout, and are difficult to relate to their ground state analogues.

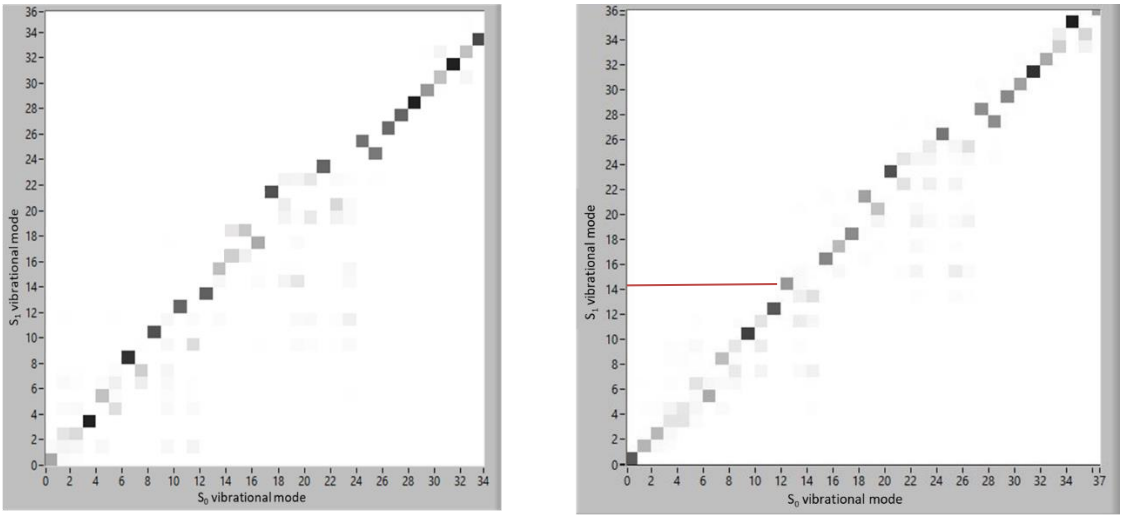

Figure 4-15: Duschinsky mixing of the normal modes in the S_0 and S_1 state of the anethole monomer (left) and anethole-argon cluster (right).

Most of the in-plane modes are once again the purest, although some mixing does manifest for ν_{38}, indicated by the red line, as a higher energy vibration from the ground state, an out-of-plane ring hydrogen wag makes up about 10% of the S_1

vibrational character. The Duschinsky mixing did not vary substantially between conformers.

4.4.4 Excitations

The first excited state of the anethole-Ar cluster is predicted to be a ππ* state, consisting mainly of an electronic transition between the HOMO and LUMO π molecular orbitals.

This configuration is a larger component of the overall excited state in the *syn* conformer compared to the *anti*. At 60 and 47 % respectively. The majority of the remainder is made up of the HOMO to the second π LUMO transition in both cases (12 % for *syn* and 23% for *anti*).

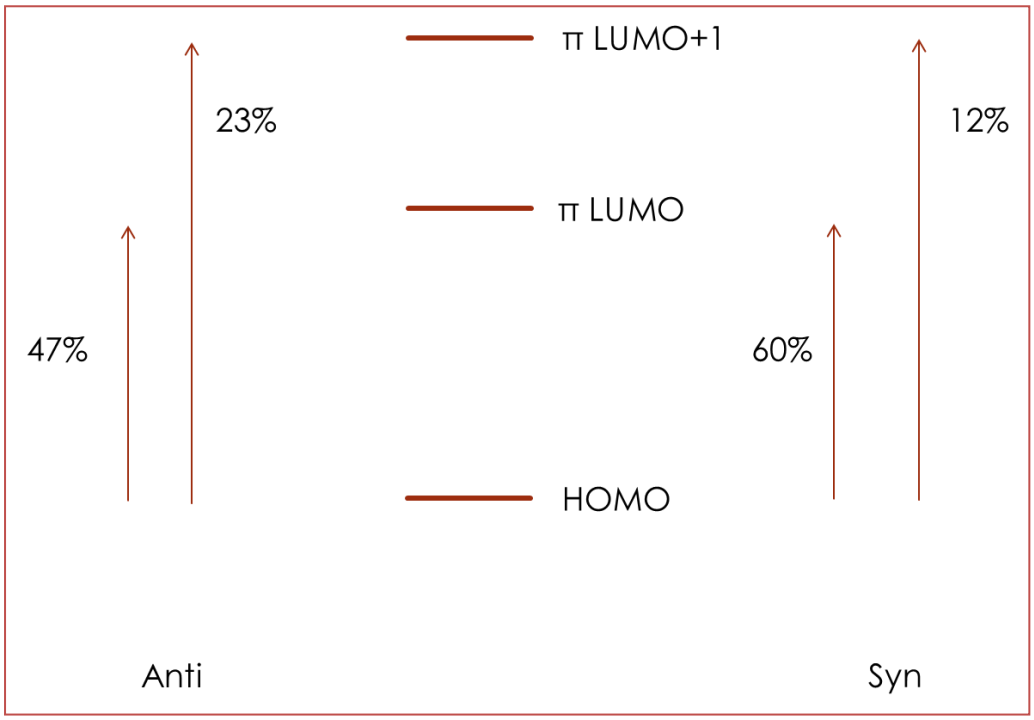

Figure 4-16: Calculated contributions to electronic excitation of the anethole-Ar complex.

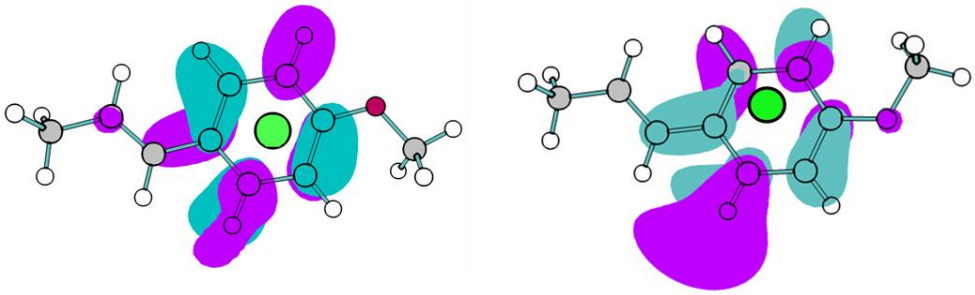

Figure 4-17: π LUMO + 1 for the *anti* (right) and *syn* (left) anethole-argon cluster.

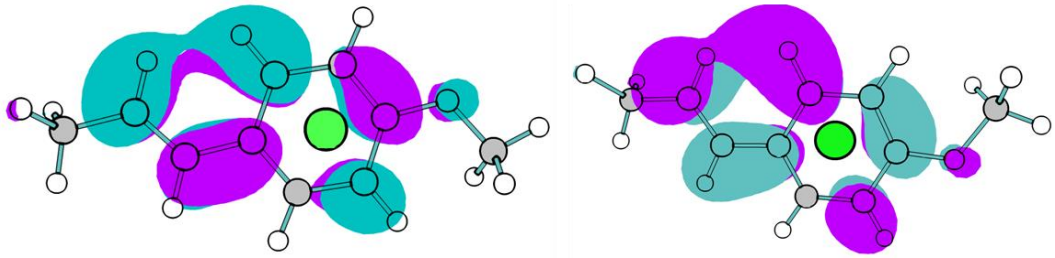

Figure 4-18: π LUMO for the *anti* (right) and *syn* (left) anethole-argon cluster.

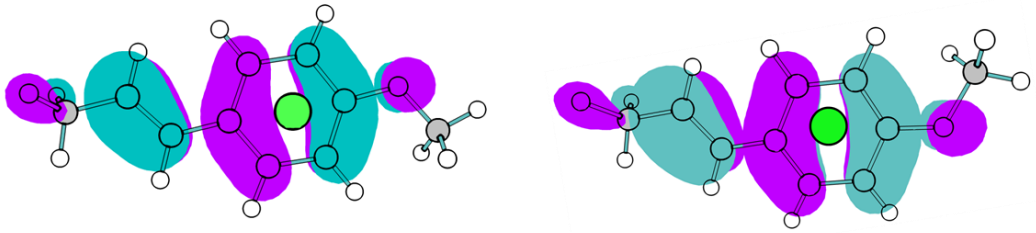

Figure 4-19: HOMO for the *anti* (right) and *syn* (left) anethole-argon cluster.

The excitation in the complex shows no marked change from the monomer electronic structure; there is less than 2% difference in the excited state electron configuration for either conformer.

Figure 4-20 shows why it is to be expected that the orbitals involved in excitation remain firmly localised on the anethole fragment, as the lowest energy orbital located on the argon atom is some 45000 cm^{-1} lower in energy than the π HOMO. Therefore, the energies needed to excite the argon-localised electrons are correspondingly higher.

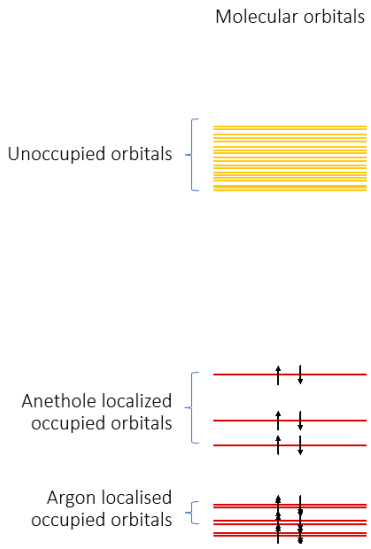

Figure 4-20: Energy levels of molecular orbitals in argon-anethole complex.

4.4.5 Geometry changes upon excitation and ionisation

As in the monomer, the *anti* conformer shows a reduction in planarity upon excitation to the S_1 state. In the complex this geometry change is more pronounced than in the monomer, with the ring hydrogens tilting up to 0.7 degrees away from the plane of the ring. This time, however, the *syn* conformer also exhibits some diversion from Cs symmetry, although still less pronounced than the *anti* counterpart, with a maximum deviation from planarity of 0.5 degrees. These changes are possibly reflected in the strong intensity of the ν_{38} mode in the *anti*-anethole-Ar REMPI spectrum, although really we should expect to see some sign of this mode in the *syn* conformer also, reflecting the geometry change along this coordinate. The increase in out of plane geometry distortion upon complexation is a reflection of how even a single weakly bound atom can influence the geometry of a larger species, showing the importance of gas-phase spectroscopy and computational modelling of only weakly "solvated" systems.

Besides the changes in planarity we see the ring expansion and then contraction upon excitation and then ionisation that is by now familiar in $\pi\pi^*$ S_1 states. The expansion is the same size in both monomer and complex, increasing opposite average carbon-carbon distances in the ring from 2.82 Å in the ground state to 2.87 Å in the S_1

Counterpoise corrected *ab inito* calculations were performed, giving zero-point energy corrected binding energies of each complex in each state in the table below. Two computational methods were used, RICC2, and DFT with a wb97x-v functional, both with aug-cc-pVDZ basis sets. These are compared to the

experimentally determined dissociation energies of a closely related anisole-Ar complex[109]:

Table 4-3: Intermolecular distances and calculated binding energies of anethole-argon across different electronic states.

	Anti	*Syn*	*Anti*	*Syn*	*Anti*	*Syn*
	S_0		**S_1**		**D_0^+**	
Intermolecular distance / Å	3.46[a]	3.46[a]	3.38[a]	3.38[a]	3.42 [b]	3.46[b] 3.30[a]
Binding energy: RICC2 / cm^{-1}	-532	-532	-638	-642	---	---
Binding energy: DFT / cm^{-1}	-558	-560	---	---	-582	-589
Anisole (exp)[109] / cm^{-1}	385		423		581	

[a] calculated using RICC2, [b] calculated using DFT.

The major intermolecular geometry change upon electronic excitation to the S_1 state is due to strengthening of the bonding between the two species. Intermolecular distances, defined as the distance between the argon atom and the plane of the ring, were identical for the two conformers in the ground and first excited state. Upon excitation we see a reduction in intermolecular distance of about 0.08 Å, as bonding between the two species strengthens, this is accompanied by a 100 cm^{-1} increase in binding energy, as calculated with counterpoise corrected RICC2.

The increased bonding upon excitation can be explained by examination of the excitation, which was similar to the monomer results. With excitation the electron density is concentrated slightly upon the benzene ring. The HOMO has quite a dispersed region of electron density which focuses toward the centre of the molecule in both LUMOs that become occupied. This is seen as a decrease in dipole moment across the molecule, (from 1.41 to 1.36 Debye in the *syn* conformer). This increase in electron density in the region closest to the argon atom will draw the solvent closer as the van der Waals bonding strengthens, as reflected in the increased binding energy upon excitation. Additionally, TDDFT studies have shown that the polarizability of aromatic molecules often increases upon electronic excitation, particularly when accompanied by a reduction in dipole moment.[110, 111] The anethole could therefore become more polarisable in the ππ* state, increasing the instantaneous dipole-induced dipole attractive force in the S_1 state.

In the cation things become a little more complicated. RICC2 proved to be a difficult method to use for weakly bound ion complexes. Convergence to a true minima was not possible for the *anti* conformer, without any imaginary vibrational frequencies

being present. The *syn* conformer did converge and showed a strong further reduction in intermolecular distance. This is likely to be at least qualitatively accurate, as the positive charge is even more attractive to the argon atom than the dipole that was there previously, as the charge induces a larger dipole in the solvent and increases the bonding strength once more.

However, the DFT optimisations predicted much larger intermolecular distances for both conformers than the RICC2 showed for the *syn*. Binding energies were calculated using DFT for both the neutral and cationic ground states, and they show an increase in binding energy upon ionisation. I therefore believe that should I have optimised the ground state neutral complexes with DFT also, this would likely have given a larger intermolecular distance in the S_0 state, which would have reduced upon ionisation. This means that either the RICC2 is underestimating the distance, or the DFT is overestimating it.

A comparison of the ground state binding energies via different methods shows that the CC2 predicts a slightly lower binding energy for both conformers, but which value is closer must be determined through the acquisition of an experimental binding energy and is a possibility for future work.

4.4.6 Binding in a weakly bound complex

In the S_0 and D_0^+ states a closer look can be taken at the computed contributions to bonding within a van der Waals complex. A breakdown of the contributions towards the binding energy of the argon atom to the anethole are shown in Table 4-4, as computed by Dr Cate Anstöter.

Table 4-4: Contributions to binding energy by conformer in the argon-anethole complex

	Electrostatic / cm^{-1}	Pauli / cm^{-1}	Dispersion / cm^{-1}	Polarisation / cm^{-1}	Charge Transfer / cm^{-1}	Total / cm^{-1}
***Anti* S_0**	-977	1410	-1050	-25	86.5	-558
***Anti* D_0^+**	-891	1310	-1040	-105	148	-582
***Syn* S_0**	-976	1400	-1050	-25	93	-560
***Syn* D_0^+**	-794	1180	991	-102	119	-589

- The electrostatic and Pauli terms are the attractive and repulsive forces, respectively, of bringing charged, or partially charged, species close together.

- The dispersion term covers the instantaneous dipole-induced-dipole forces present between all species.
- The polarisation term accounts for the lowering of energy due to relaxation of the molecular orbitals, and describes the energy change of molecular orbitals rearranging in the presence of one another.
- The charge transfer energy is another interfragment energy relaxation correction, it includes the energy lowering due to transfer of electron density from an occupied orbital on one fragment into a virtual orbital on the other, particularly present in a system with strong back bonding such as a metal ligand arrangement.

These terms are all counterpoise-corrected to account for basis set superposition error.

In the S_0 state the components of binding interaction between the two species is almost identical for both conformers, the electrostatic and dispersion terms are by far the greatest contributors to the binding energy. The Pauli energy is the biggest repelling factor, but the total energies of binding are very similar, separated by only 2 cm^{-1}. This means we should expect to see around the same proportion of complexes being formed as the conformational ratio we saw in the monomer spectra, which is close to what we do see.

In the cation ground state the polarisation energy greatly increases, and the Pauli repulsive term decreases, these effects are slightly cancelled out by decreasing electrostatic attraction, but the overall binding does increase by 20-30 cm^{-1}, which is seen in a slight decrease in intermolecular distance compared to the S_0 in the RICC2 optimised *syn* anethole-argon complex.

4.4.7 Ionisation energies:

The ionisation energy is determined to a high degree of accuracy by combining the energies of the two photons absorbed to give the origin band in the ZEKE spectrum following excitation of the origin band from the REMPI spectrum. This gives the exact transition energies to go from the S_0 state $\nu = 0$ level to the S_1 state $\nu = 0$ level to the D_0^+ $\nu = 0$ level. Consequently, upon ionisation there is no excess vibrational energy in the molecule at all.

Ionisation energies for the conformers as monomers and as part of a complex are reported in Table 4-5.

Table 4-5: Ionisation energies of anethole and anethole-argon.

	Ionisation energy /cm^{-1}	
	Syn	***Anti***
Monomer	60614.6	60624.1
Argon cluster	60545.7	60566.2

The *anti* conformer has a slightly higher ionisation energy, both as a monomer and as a complex than the *syn*. The addition of an argon atom lowers the ionisation energy, suggesting that the argon helps to stabilise the positively charged anethole. The *syn* conformer is more stabilised upon complexation than the *anti*, but on the same order of magnitude, at 69 cm^{-1} compared to 60 cm^{-1}. This result has been seen before in similarly studied systems[109, 112]: the closely related anisole-argon complex found a red shift in the ionisation energy upon complexation of 196 cm^{-1}, which is significantly more than the approximately 60-70 cm^{-1} shift that we see for the anethole complex. Anisole is a monosubstituted aromatic molecules, and therefore it could be that it is more stabilised as an ion in the presence of an argon atom than anethole, because in the anethole complex the other substituent, a propene group, already stabilised the ion substantially more than the hydrogen counterpart in anisole does. The π orbitals of the alkene can stabilise the positively charged ring system through delocalisation,[113] thus the relative stabilisation of the argon atom is diminished compared to the anisole-argon complex.

4.5 Conclusions

The REMPI and ZEKE spectroscopy of the 1:1 anethole-argon complex shows an above the ring binding site. The binding of this weakly bound complex strengthens in the first neutral excited state and then again in the cation, seen as a reduction in intermolecular distance in the calculations, and appearing spectrally as a strong feature of the intermolecular stretching vibrational mode ν_{64}. The greatest contributions to the binding are the electrostatic and dispersive effects.

Unfortunately, theoretical work on the complex was less successful than the monomer system for predicting the experimental results, but through combining both density functional theory and *ab initio* techniques, a fair interpretation was made. The argon atoms disrupts the planar nature of the anethole monomer, increasing a lowering of planarity in the excited state, this is seen particularly strongly in the *anti* conformer, which shows a clear distortion of the ring hydrogens, reflected in strong features in the REMPI spectrum along this vibrational coordinate.

Once again, the two conformers behaviour is very similar, with only small differences in calculated binding energy and spectroscopic features.

Chapter 5. Benzocaine

5.1 Introduction

Ethyl 4-aminobenzoate, commonly referred to as benzocaine is a widely used anaesthetic found in many topical ointments and throat treatments due to its numbing properties.[58] As a drug molecule benzocaine has long been the subject of intense scrutiny. It plays a key role as a pain suppressor, and has been theorised to work by disrupting the sodium ion channels in pain receptors, possibly through a van der Waals type arrangement of bonding to the receptor.[58, 59, 114] As a topical anaesthetic it is reasonable to assume that it will be exposed to the electromagnetic radiation present in sunlight, and therefore UV spectroscopy is key to understanding how the structure of the molecule, and therefore perhaps the therapeutic benefits, might change upon exposure to sunlight.

Benzocaine and a number of associated van der Waals complexes including argon, water and toluene, have been studied previously in the gas phase using a number of spectroscopic and computational techniques.[31, 57, 59, 60] Benzocaine exists as two stable conformers, and has been studied in both forms, as well as part of a variety of clusters.[30, 31, 58] In this chapter I will build on previous work to give a computational analysis of the ground, excited and cationic states, as well as providing improved REMPI and ZEKE spectra. This was also an opportunity to test the capacities of a much-adapted experiment.

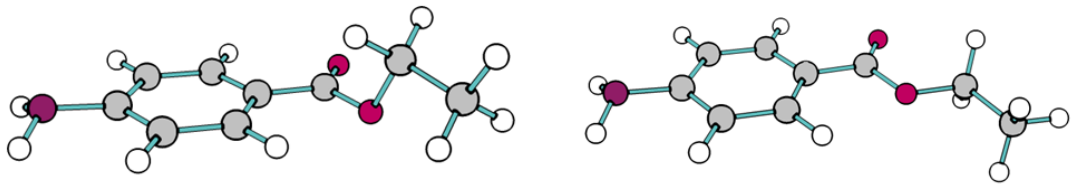

Figure 5-1: *Gauche* (left) and *trans* (right) benzocaine.

The ground state geometry of benzocaine is well understood: it exists in two conformational forms, a *gauche* and a *trans*. In the *gauche* conformer the ethyl group stands perpendicular to the plane of the ring, whereas in the *trans* conformer it lies in the plane. As in many aminobenzene molecules, the NH_2 is slightly pyramidalised with the hydrogens pointing out of the ring plane at an angle of approximately 31° due to delocalisation of the nitrogen lone pair electrons.[60]

5.2 Experimental

5.2.1 REMPI and ZEKE

Benzocaine was introduced to the vacuum chamber as a pulsed supersonic free-jet expansion in argon buffer gas at 0.1 bar. Suitable partial pressures of benzocaine were produced by the heating of the sample chamber and nozzle to 105 °C. Vacuum pressures were approximately 1.1 x 10^{-7} mbar in the laser interaction chamber throughout the experiments.

Two-colour REMPI spectra were recorded using the frequency doubled output of a Radiant Dyes Narrowscan dye laser, with a series of different dyes used to generate all necessary frequencies. The lower frequency part of the REMPI spectrum was obtained using Sulfurrhodamine B in ethanol, whilst the higher frequency measurements were obtained using a mixture of Sulforrhodamine B and Rhodamine 6G at a ratio of 1:2, and then Rhodamine 6G in isolation. This provided a wavelength range of 590 nm to 560 nm, pre-doubling. A probe (ionisation) photon of 335 nm was provided using the doubled output of Pyridine 1 dye in ethanol pumped with a Jaguar dye laser.

Once the REMPI spectrum was obtained vibronic states were selected as intermediate states for the acquisition of ZEKE spectra. In the ZEKE experiment a pump photon was provided with the Narrowscan laser using Sulphorrhodamine B in ethanol for the origin and lowest energy vibronic state, and then a mixture of Sulphorrhodamine B and Rhodamine 6G for the subsequent four higher energy vibronic states. A scanning photon was provided as the frequency doubled output of a Jaguar dye laser using Pyridine 1 in ethanol.

All spectra were obtained using a ten shot average data collection method, scanning in 0.005 nm step sizes. Laser calibration was achieved using the optogalvanic lines of an argon lamp, covering the entire spectral range used in these experiments.

5.2.2 Computational

Benzocaine was optimised in the S_0, S_1 and D_0^+ states using *ab initio* and density functional theory methods. The RICC2/aug-cc-pVDZ method was used for the ground and ground cationic states, using Turbomole 6.4, whilst a variety of basis sets and methods were used across Turbomole and Gaussian 16 for the S_1 state. A

vibrational analysis was conducted to ensure true minima were present, as verified by the lack of imaginary vibrational frequencies. In addition, the potential energy surfaces of the amino group inversion and the methyl group rotation were computed for the S_1 and D_0^+ states using Gaussian 16.

Simulated REMPI and ZEKE spectra were generated from the calculated vibrations using FCLABII.[37]

5.3 Experimental results

5.3.1 REMPI spectrum

The two-colour REMPI spectrum of benzocaine is shown in Figure 5-2: Two-colour REMPI spectrum of benzocaine. * refers to modes further studied with ZEKE.Figure 5-2. Rather than previous REMPI studies which showed the presence of two conformers, the presence of only a single origin feature shows that the backing gas pressures have been sufficient in reducing the effective temperature of the molecular beam to drive the population into the lowest energy conformer, the *trans*. This matches previous works, who reduced the population of the *gauche* conformer by increasing the argon to helium ratio of their backing gas.[57, 115, 116] If present, the *gauche* conformer should have been seen as a second origin feature, a few wavenumbers to the blue of the *trans* origin. [32, 116]

The REMPI spectrum shows a multitude of features, many as strong or stronger than the origin band. This is indicative of substantial geometry change upon excitation and allowed many opportunities for further exploration with ZEKE spectroscopy.

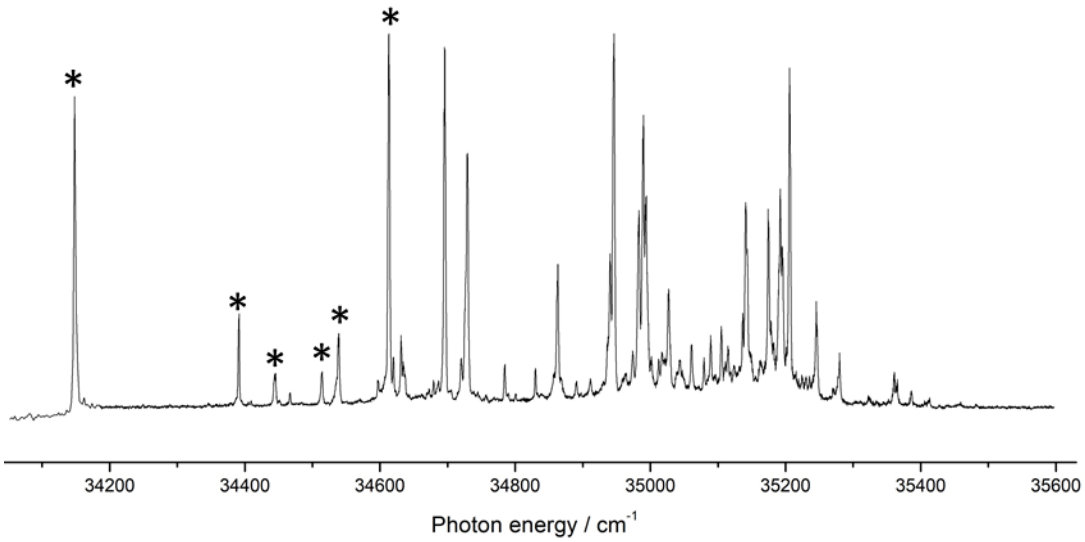

Figure 5-2: Two-colour REMPI spectrum of benzocaine. * refers to modes further studied with ZEKE.

Vibronic states selected for further ZEKE analysis are shown in Figure 5-2. Modes were selected for a variety of reasons. Some ZEKE work has been published previously, and this work was not intended to duplicate their results, so in general different intermediate states were selected to give new insight into the spectroscopy of benzocaine. Secondly, due to the spectral range this work covered, it was inconvenient to choose intermediate states of particularly high frequency, as this would have necessitated multiple dye changes that would disrupt the spectra collected. Therefore, the lower frequency vibronic states were chosen as intermediates for the ZEKE work.

5.3.2 ZEKE spectra

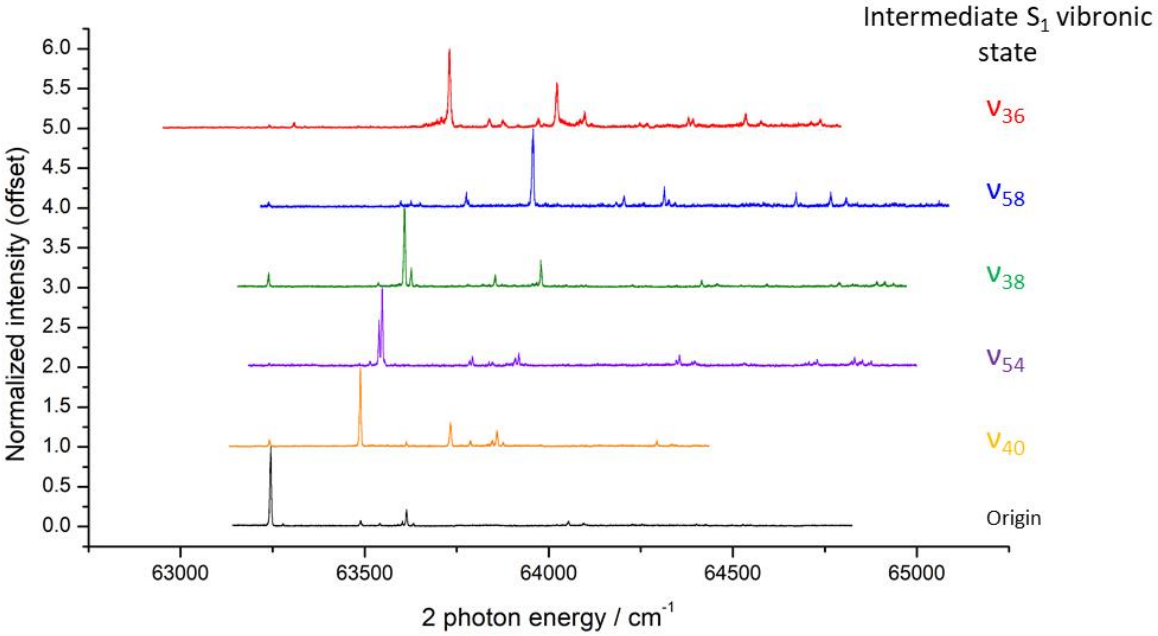

Figure 5-3: ZEKE spectra recorded via the origin and five different vibronic states.

The origin pumped ZEKE spectrum is far less congested than the REMPI. Only a few, low-intensity, features accompany the origin peak. For the other ZEKE spectra the dominant transition is always the one corresponding to $\Delta v=0$, and for many of them a strong series of progressions for the intermediate state vibration is also recorded. The ZEKE spectra acquired for $v\neq0$ intermediate vibronic states show far more features, with each spectrum holding its own features of note. These will be discussed in section 5.4.3.

The ionisation energy of benzocaine was found to be 63 245 cm^{-1}, taken as the total two photon energy of the first band in the origin pumped ZEKE spectrum.

5.3.3 Computational results

S_0 geometry

In the ground state the geometry of benzocaine was found to be a planar molecule with the exception of the amino hydrogens which point out of the plane of the ring in a pyramidal arrangement, similar to what has previously been reported for benzocaine [30, 32, 60, 116, 117] and other aminobenzene molecules.[118, 119] The NH_2 dihedral angle was 35° out of the plane of the ring for both hydrogens. Whilst the literature, both experimental and theoretical shows the presence of two S_0 conformers, only the *trans* conformer converged during the RICC2 calculations. As this was the only conformer present in the experimental results no further study of the ground-state *gauche* conformer was performed.

S_1 geometry

Several geometry optimisations of the S_1 state were performed using different methods, programmes and basis sets. The major ambiguity in the calculations were the placement of the ester group and the planarity of the NH_2. Many optimised geometries were found to have imaginary vibrational frequencies, suggestive of a shallow potential energy surface. The calculations that converged to a true minimum can be separated into three categories of geometry:

1. *Trans* planar:

- TDDFT using the ωB97xd functional and an aug-cc-pVDZ basis set converged to a completely planar geometry with the ethyl group arranged *trans* to the carbonyl.

2. *Gauche* pyramidal

- RICC2 aug-cc-pVDZ adopted the *gauche* conformation, with the ester group pointing out of the plane of the ring, and a pyramidal amino group, even with a *trans* starting structure and tight convergence criteria.

- RICC2 cc-pVDZ produced a twisted structure, with the ester group angled halfway out of the plane, with a pyramidal NH_2 group.

3. *Trans* pyramidal:

- CIS cc-pVDZ produced a planar ring structure with a pyramidal NH_2, here the amino hydrogen dihedral angles are each 18° to the plane of the ring.

- RICC2 cc-pVTZ gave a planar structure but with an imaginary frequency for the NH_2 inversion mode, suggesting that this is actually a transition state along this vibrational coordinate.

Cation geometry

The cationic ground state of benzocaine was calculated to be nearly completely planar, with no dihedral angles besides the ethyl hydrogens more than 0.03° out of the symmetry plane.

Vibrational structure of benzocaine

There are 63 normal modes of benzocaine, in the ground state, which is well-known to have a pyramidal NH_2 group and therefore be of C_1 symmetry, meaning all 63 modes would be of A symmetry. However, as symmetry increases to some degree upon excitation and completely upon ionisation benzocaine assumes a planar geometry, which gives 41 in-plane modes of A′ symmetry, and 22 out-of-plane modes with A″ symmetry. As the vibrations we are assigning in this work are based on the vibronic levels in the excited and cation states I will use the higher symmetry model. Modes ν_{63} to ν_{42} are the out-of-plane modes in order of ascending frequency, whilst ν_{41} to ν_1 are the in-plane modes in order of ascending frequency. Some shifting of frequencies take place at the different electronic configurations, thus the ordering is determined by the ground state calculations.

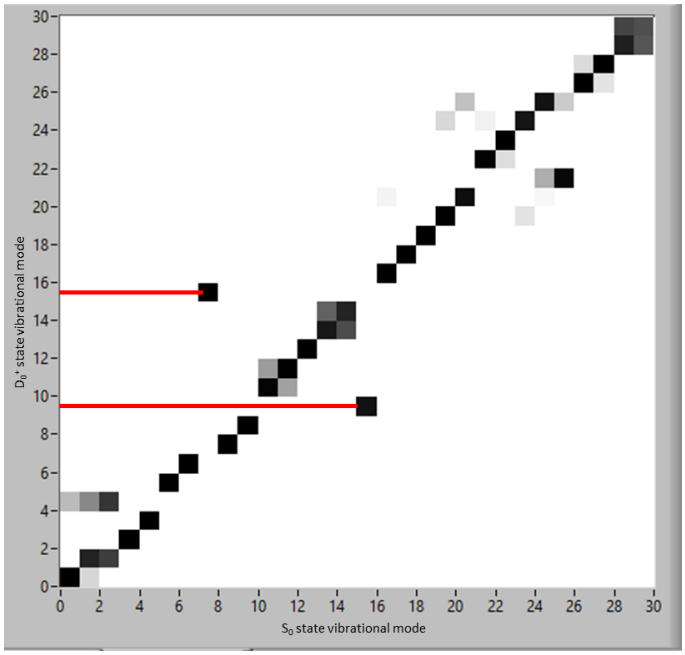

Figure 5-4: Duschinsky mixing of the normal modes of benzocaine upon ionisation.

Duschinsky analysis of many of the normal modes was undertaken. Due to the complexity of the S_1 state results, only specific instances of mixing in the electronically excited states will be reported in the discussion section. Figure 5-4 shows the mixing that occurs between the well-defined S_0 and D_0^+ states. Here it is seen that many modes retain their vibrational character as they transition to the cation state, although the large number of off-diagonal strong black features represents a fair degree of mode reordering. In particular, ν_{58} and ν_{54}, which correspond to the amino inversion and rocking out-of-plane vibrations respectively, undergo large shifts in frequency upon ionisation, highlighted in the figure above by the red lines.

5.4 Discussion

5.4.1 Structural interpretation of the REMPI spectrum

The REMPI spectrum is highly congested, making full vibrational assignments very difficult. We see a multitude of features as strong or stronger than the origin peak, suggesting significant distortion along the coordinates of several vibrational modes. This is indicative of a large change in geometry upon excitation.

Previous works[31, 57, 60, 116] have only assigned the main features of the spectra, but as there was success in freezing out the *gauche* conformer this work aimed to give a more thorough analysis, as there are now 50% fewer peaks in the spectrum. Unfortunately, however, this vibrational analysis of the benzocaine spectra is also not totally complete. The geometry of the excited state has not previously been reported in similar experimental or theoretical work, and is still not understood fully here, despite the multitude of computational methods used. Vibrational frequencies associated with each geometry varied widely, as did the Franck-Condon factors associated with each model. No S_1 state gave a convincing REMPI simulation, as shown in Figure 5-8 below, thus the vibrational assignments and predicted geometries remain strongly speculative.

Whilst the excited state geometry cannot be definitively described, all of the methods yielded a planar or at least a less pyramidal NH_2 group. Simulated REMPI spectra were produced for the majority of these geometries, with the exception of the *gauche* ester variants. These proved impossible to simulate due to the much larger geometry change leading to unresolvable difficulties in rationalising the coordinate systems in our multidimensional Franck-Condon calculations.

In any case, it seems unlikely that the *trans* to *gauche* rearrangement is occurring, as this would be a very significant geometry change indeed, in fact the movement of an entire C_2H_5 group out of the plane of the ring would likely be such a strong

distortion that the Franck-Condon factor associated with the origin feature would be very small. However, we do see a strong origin peak present, corresponding to the $\Delta v=0$ transition, suggesting that the essential structure of the carbon backbone of the molecule retains its ground state conformation.

In addition, compelling evidence in the form of a comparison to another amino-substituted benzene convinces us that the ethyl group probably retains planarity upon excitation. Para-amino benzoic acid, PABA, is a simpler para-substituted amino-containing aromatic molecule, which has been studied previously with REMPI and ZEKE spectroscopy, by Kong et al.[118]

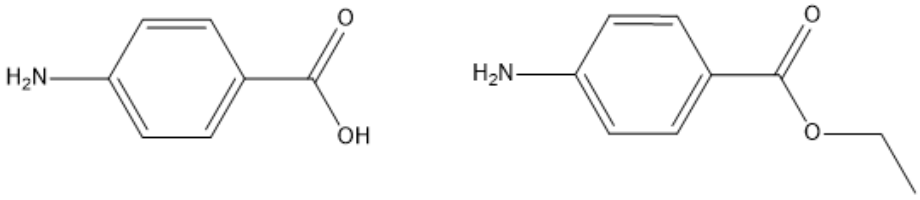

Figure 5-5: Structures of para-amino benzoic acid (left) and benzocaine (right).

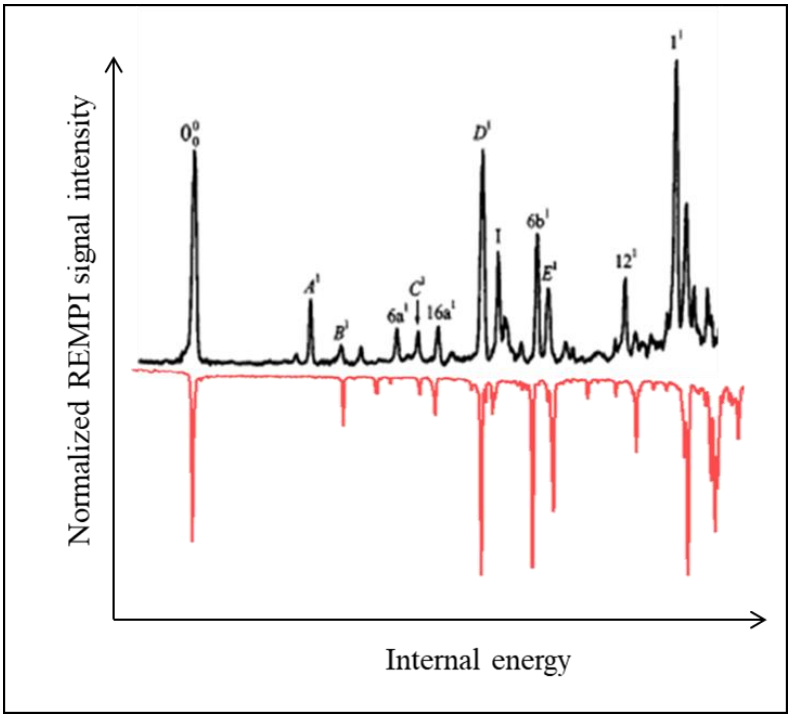

Figure 5-6: REMPI spectrum of para-amino benzoic acid reproduced from the work by the Kong group[118] (top) compared with the related 0-1000 cm^{-1} section of the benzocaine REMPI spectrum (bottom).

The overall appearance of the two REMPI spectra are very similar, suggesting that the features we see are mostly due to vibrations affecting the amino group, ring system and the COO group. There appear to be minimal vibrational contributions from the ethyl group, suggesting either that the associated geometry changes are small or that these modes appear at higher frequencies than the region covered in Figure 5-6. This also provides further compelling evidence that the S_1 state retains the *trans* structure of the electronic ground state. The relative intensities of the vibrational features compared to the origin peak suggest that a similar level of geometry distortion is occurring upon excitation between the two molecules.

The next question surrounding the geometry of the excited state concerns the amino group, and whether it retains its pyramidal arrangement in the S_1 state or adopts a planar or pseudo-planar arrangement. Some insight into this question may be provided by comparison to the behaviour of aniline. Aniline, the simplest aminobenzene analogue has been reported as having a planar.[119-121] or quasi-planar,[109, 122-125] S_1 state with a double-well potential with a barrier height significantly smaller than the zero point energy. However, another study has reported the S_1 state as fully pyramidal, with a dihedral angle between the ring plane and the amino hydrogens of more than 40°.[126] It is my opinion that the aniline work that suggests a planar or quasi-planar geometry is the more likely of the two options, based on the overwhelming majority and variety of both the theoretical and experimental literature that points to this, whereas only one experimental group has theorised a pyramidal arrangement. That being said, the Cui group who argued for a pyramidal NH_2 structure based their conclusions on some high-level (CASSCF) calculations, and some compelling photoelectron data, which should not be immediately disregarded. Evidently, there appears to still be room for speculation, and we can't make easy comparisons between the two molecules, with the simpler analogues structure also inconclusive.

Past literature of benzocaine is also unreliable as a navigator. Previous work has all focussed on ground-state vibrational analysis, the difficulties that I have faced in calculating the S_1 structure are presumably the reason why. Vibrational assignments in this work are therefore based on a mix of calculations, previous REMPI and LIF work, and also through comparison to para-amino-benzoic acid. Where deviations from past literature occur, this is rationalised on a case-by-case basis.

Ground to cation overall transition

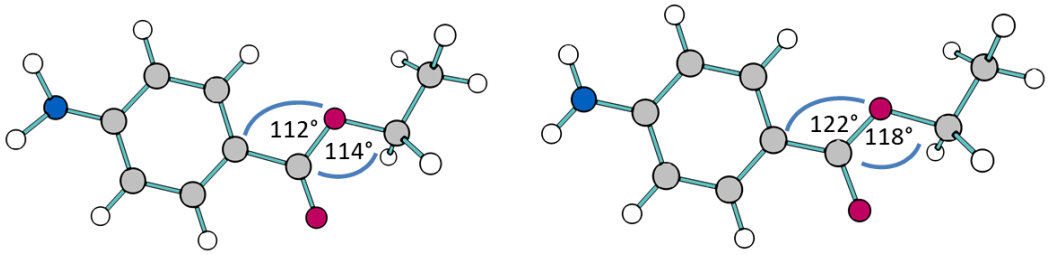

Figure 5-7: Ground (left) and cation (right) geometries.

If we consider the total transition as an S_0 to D_0^+ what overall geometry changes should we see? Looking at the calculated neutral and cation structures the biggest visual changes are the increased planarity of the amino group and an elongation of the ester as the CCO and the COC bond angles strongly increase. There is also a slight increase in ring distortion, where the CC bonds have slightly less even bond lengths around the ring, although this change is small. The planarity of the ring itself is constant throughout all the calculations.

The movement of the substituents suggests that in the cation the NH_2 group acts as an electron donating substituent, allowing the amino hydrogens to move up into the plane of the ring as the lone pair electron density shifts away. Meanwhile the COOEt group acts as an electron withdrawing substituent that destabilises the ring system, as, with less electron density on the ring upon ionisation, the ester group relaxes away from it.

If this is the total, double excitation, process that occurs, it stands to reason that we should see the features associated with these distortions in either the REMPI or the ZEKE spectra. There is no evidence of a drastically distorted S_1 state, that is highly different from both the S_0 and D_0^+ geometries, as this would be demonstrated by a congested REMPI spectrum and a congested ZEKE spectrum. Therefore, the majority of the geometry change must occur during the REMPI transition, as this is the busy spectrum, and we must interpret the strong origin feature in the origin pumped ZEKE spectrum to mean that the ion has a similar structure to the S_1.

Given all of the above, I will now present the vibrational analysis of the REMPI.

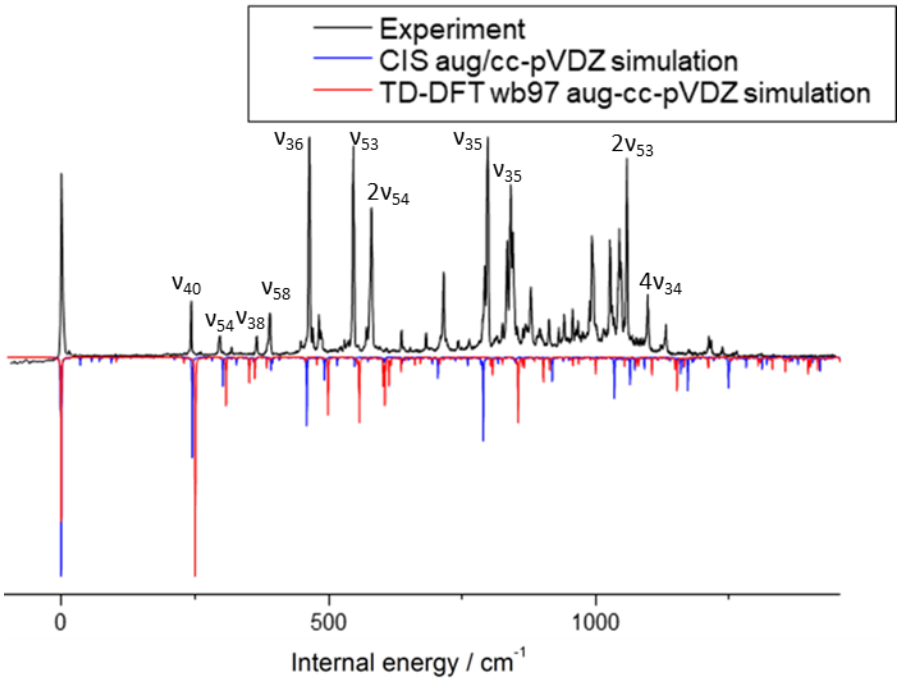

Figure 5-8: Simulated REMPI spectra based on a planar (TDDFT) and pyramidal (CIS) S_1 state.

Table 5-1: Vibrational assignments of benzocaine REMPI spectrum.

Relative frequency / cm^{-1}	TD-DFT	CIS	PABA	Assignment	Mode description
243	229	258	185	ν_{40}	In-plane substituent bend
298	332	481	483	ν_{54}	NH_2 inversion
366	363	376	366	ν_{38}	NH_2 in-plane rocking
391	352	366	388	ν_{58}	NH_2 rocking out of plane.
465	457	541	459	ν_{36}	In-plane substituent bend with ester angle opening
548		610	546	ν_{53}	NH_2 inversion with ring distortion.
581				2 ν_{54}	
683				$\nu_{54} + \nu_{58}$	
797	826	828	768	ν_{35}	Ring breathing
879	871	924		ν_{34}	Ring distortion
1098				2 ν_{53}	
1132				4 ν_{54}	

5.4.2 REMPI analysis:

Benzocaine in the S_1 state is suspected of having C_s symmetry, and therefore the in- and out-of-plane vibrations have A′ or A″ symmetry respectively. The transition dipole moment of the $S_1 \leftarrow S_0$ transition is in the plane of the ring, therefore only the excitation of in-plane or even quanta of out-of-plane vibrational modes are symmetry allowed. Franck-Condon considerations also contribute to the intensity of spectral features, and may lend intensity to symmetry forbidden transitions.[127]

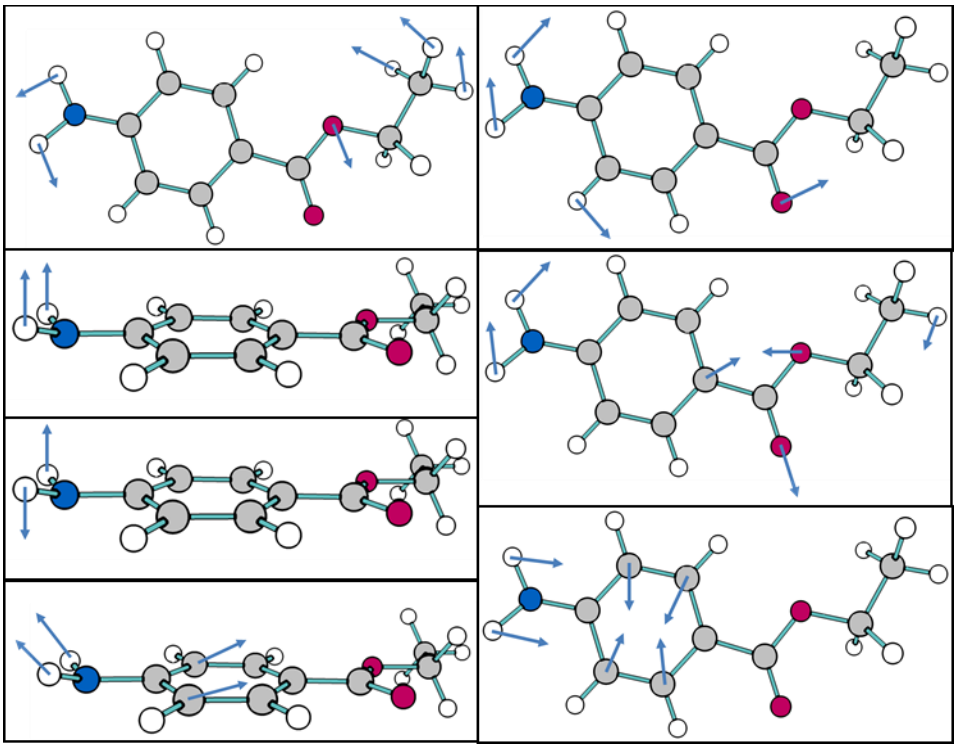

Figure 5-9: Key vibrations of the benzocaine REMPI spectrum, clockwise from top left: ν_{40}, ν_{38}, ν_{36}, ν_{35}, ν_{53}, ν_{58} and ν_{54}.

I have reassigned the peak at 298 cm^{-1} to the NH_2 inversion mode, ν_{54}; most previous literature [31, 57] assigns this band to an out-of-plane ring buckling mode, akin to the 10b mode in Wilson's nomenclature of benzene.[128] It is reassigned here based on the analysis of the ZEKE spectrum recorded via this intermediate level. In addition, the literature vibrational assignments were based on ground state vibrational frequencies. The S_0 vibrational frequency of the inversion mode calculated here is 561 cm^{-1}, which I believe is why it has never been considered previously to be assigned to the lower frequency feature at 298 cm^{-1}. However, a normal mode analysis shows that its frequency reduces significantly in the cation state to 333 cm^{-1}. The ZEKE spectrum acquired using this vibrational frequency as an intermediate exhibits a strong

diagonal ($\Delta v=0$) feature at 305 cm^{-1}, which would correlate reasonably well with the predicted cation frequency for this mode.

Considering that the inversion mode is expected to feature strongly in the REMPI spectrum, due to the predicted increase in NH_2 planarity, the peak at 298 cm^{-1} looks to be smaller than expected, based on Franck-Condon factors alone. However, the strong feature at 581 cm^{-1} is thought to be the double quanta excitation of this mode and reflects the symmetry requirements surrounding vibronic excitation. The overwhelming Franck-Condon factor associated with the inversion mode is testament to the presence of its single quanta excitation in the spectrum, and the even-quanta double excitation, which is symmetry allowed, is one of the strongest features present.

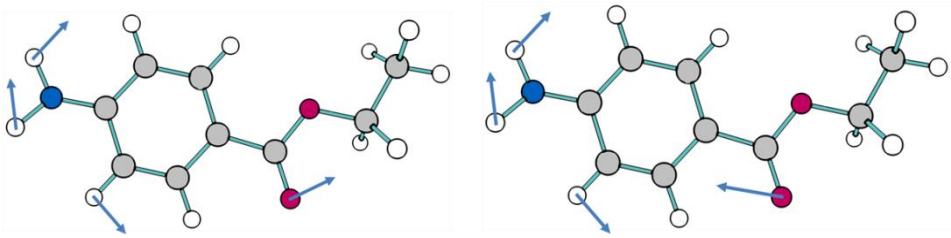

Figure 5-10: ν_{38} (left) and ν_{37} (right) normal modes.

The peak at 391 cm^{-1}, assigned here as ν_{58}, in the REMPI spectrum has previously been assigned to the antisymmetric version of ν_{38}, that is, ν_{37}.[32, 57] ν_{38}, and ν_{37} are two very similar modes that are strongly mixed in the ion state. However, the ZEKE spectra recording following excitation to the states present at 366 cm^{-1} and 391 cm^{-1} past the origin, assigned here as ν_{58} and ν_{38} are quite different, suggesting that the two intermediate vibronic states are not strongly linked, this lowers the likelihood that the previous assignments are correct. A close look at the 391 cm^{-1} REMPI feature suggests a shoulder slightly to the red, which I believe corresponds to ν_{37} in the S_1 state. I think the main body of that feature comes from a different vibration, that of the out-of-plane NH_2 rock.

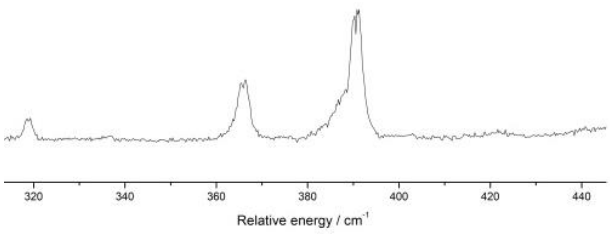

Figure 5-11: Enlarged section showing the 366 cm^{-1} and 390 cm^{-1} peaks.

Once again, this is a mode with a big change in frequency upon excitation and ionisation. The ν_{58} mode was found to be 296 cm^{-1} in the ground state, and 511 cm^{-1} in the cation. The TDDFT S_1 frequency was 352 cm^{-1}, and the CIS was 366 cm^{-1}, so it is well within the realms of probability that this could be the large component of this sloped feature we see at 391 cm^{-1}. This mode is best described as a twisting of the NH_2 group, whilst the rest of the molecule remains planar.

The largest features in the REMPI spectrum are those at 464, 547, 581, 797, 841 and 1058 cm^{-1}. These are as intense, or more intense than the origin peak, and correspond to vibrations that mirror the distortion of benzocaine upon excitation. They have been assigned to two classes of vibrations, those that involve the inversion mode of the amino group (although not that mode by itself), and in plane bends of the substituents, coupled with ring distortions. In addition, the feature at 797 cm^{-1}, the largest in the whole spectrum, is assigned to the ring breathing mode, and its presence shows there to be a large increase in ring size upon excitation, as commonly seen in $\pi\pi^*$ states, where the weakened π bonds lead to a ring expansion. The calculations performed predict an expansion of 0.1 Å between the opposite unsubstituted ring carbons, and an ever so slight contraction between the substituted carbons, of 0.004 Å.

The high intensities of features that involve in-plane movement of the ester group also correlate with our calculated structures, which showed significant distortion of the longer chained substituent. The C=O bond shortens upon excitation, suggesting a weakening in ring donation from the lone pair, whilst the OCH_2CH_3 stretches further away from the ring. Vibrations that correspond to these movements are those assigned to peaks at 465 cm^{-1} and 548 cm^{-1}.

Finally, we also see a contraction in the CN bond, which is incorporated into the ring breathing motion of the 797 cm^{-1} feature. We do not see the full extent of this geometry change in the spectra, as the pure CN stretching mode is too high in frequency to have been recorded here.

ν_{54} and ν_{58} are amino group out-of-plane vibrations, whose initial single quanta excitations are weak despite their relevance to the geometry change due to their symmetry. However, the double quanta excitations show very strong distortion in this direction, meaning that whilst there is no certainty that the S_1 state is fully planar, it certainly is less pyramidal with respect to the amino group than the ground state.

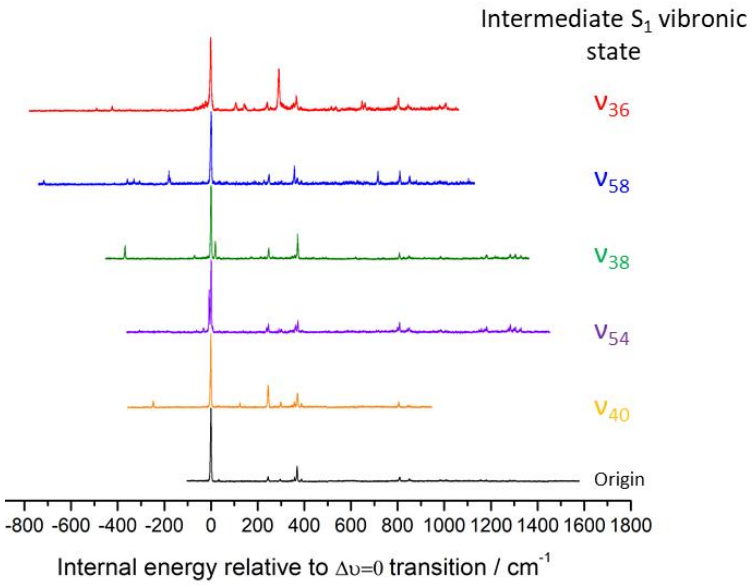

Figure 5-12: ZEKE spectra of benzocaine aligned to the Δν=0 transition.

5.4.3 ZEKE discussion

The ZEKE spectra are all fairly uncongested, compared to the REMPI spectrum, which is interpreted as benzocaine displaying a much smaller geometry change upon ionisation than excitation.

There are many interesting features to discuss, but I'll start with the origin pumped spectrum. The other ZEKE spectra all contain the same features as the origin, presented as combination bands of the origin pumped spectrum with a quanta of the mode selected as an intermediate stage, as displayed in Figure 5-12.

The vibrational coordinates most strongly distorted upon ionisation are shown to be the NH_2 and ester in plane bending motions. The bands corresponding to these features are not as strong as the origin peak in the ZEKE spectrum, but they are strong enough to show some meaningful change in this direction. There are no features that show any sort of vibrational progression.

Table 5-2: Vibrational assignments of benzocaine ZEKE spectra via different intermediate states, compared to the RICC2 cation calculated frequencies.

Intermediate pump state						Calculated frequency / cm^{-1}	Mode assignment and notes
Origin	1	2	3	4	5		
0	-248	-305	-368	-717	-491		origin
				-180	-423		
		-32	-71				
	0	-8 0	0	0	-60 to 0		$\Delta\nu = 0$
			19			335	ν_{37}
33	33		33	33	32 107	57	ν_{63} (Ethyl rotation)
	125					88	ν_{40} (In-plane ethyl bend)
245	**248**	238 246	246	248	142 240	223	ν_{40}
297	297	**292** **301**		297	289 (long progression)	333	ν_{54}
358	358	351 360	360	358	352		
369	371	364 371	**370**	371	368	378	ν_{38}
388	388	380 389		388	387	335	ν_{39} (In-plane ester bend)
					647	618	ν_{36} (Ring distortion)
					661		
		708 718		**714**		511	ν_{58}
808	804	708 808	806	810	804	797	ν_{32} (Ester CO stretch)
848	846	841 850	848	850	844	838	ν_{35}
		1150 1159	1160				

The other ZEKE spectra collected using intermediate states other than ν=0 revealed many more interesting features:

5.4.3.1 ν_{54} pumped ZEKE spectrum

The ν_{54} pumped ZEKE spectrum shows a difference from all other S_1 intermediate state ZEKE spectra recorded. The ZEKE spectrum produced from this mode shows a doubling of all vibrational features, including and following the vertical vibrational transition. The twin series of peaks are separated by 8-10 cm^{-1}, and all show the features in a 0.6:1 ratio of low frequency to high.

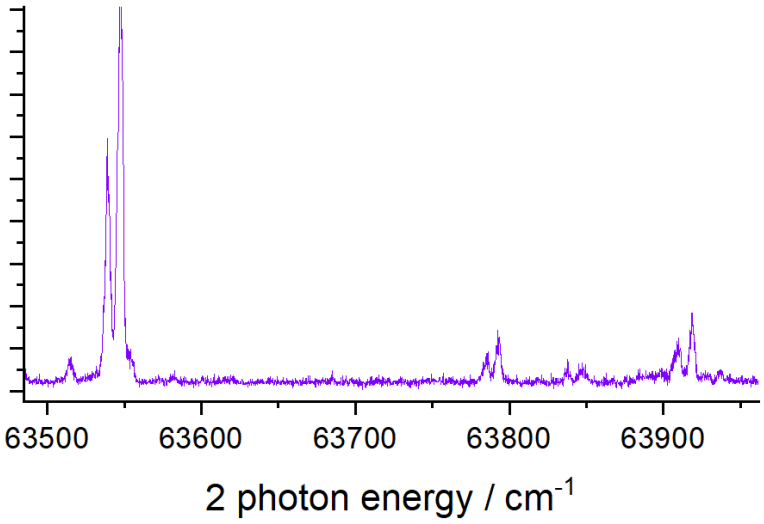

Figure 5-13: Expanded section of ν_{54} pumped ZEKE.

This could be caused by several things.

We could be exciting two different vibronic modes at once with our pump laser. If there were two very similar energy states we could be acquiring two ZEKE spectra simultaneously. However, the relative intensities of the pairs of peaks are constant and equally separated throughout. Two differently-pumped modes should give different ZEKE spectra, so this can be ruled out.

Alternatively, it's possible that the splitting is caused by quantum mechanical tunnelling, with the likely causes being either the rotation of the methyl group or inversion of the NH_2 group.[129] The methyl rotation is predicted to occur at a much lower frequency than the lines in the ZEKE spectra suggest, at 57 cm^{-1} in the cation, whereas the NH_2 inversion vibrational mode is calculated to be 333 cm^{-1} in the cation ground state. The main peaks in this ZEKE spectrum are the pair at 299 and

308 cm^{-1}, making the methyl rotational mode an unlikely source for this spectral feature.

Which group was responsible for the splitting was investigated further by calculating the potential energy surface of each vibration in both the S_1 and D_0^+ states and therefore the energy barrier that would need to be overcome by the tunnelling hydrogens.

Methyl group rotation showed a simple sine wave, with even minima for each hydrogen as they point to the lowest energy configuration, and even barriers of about 1400 cm^{-1}, for both the S_1 and the cation states, shown in Figure 5-14.

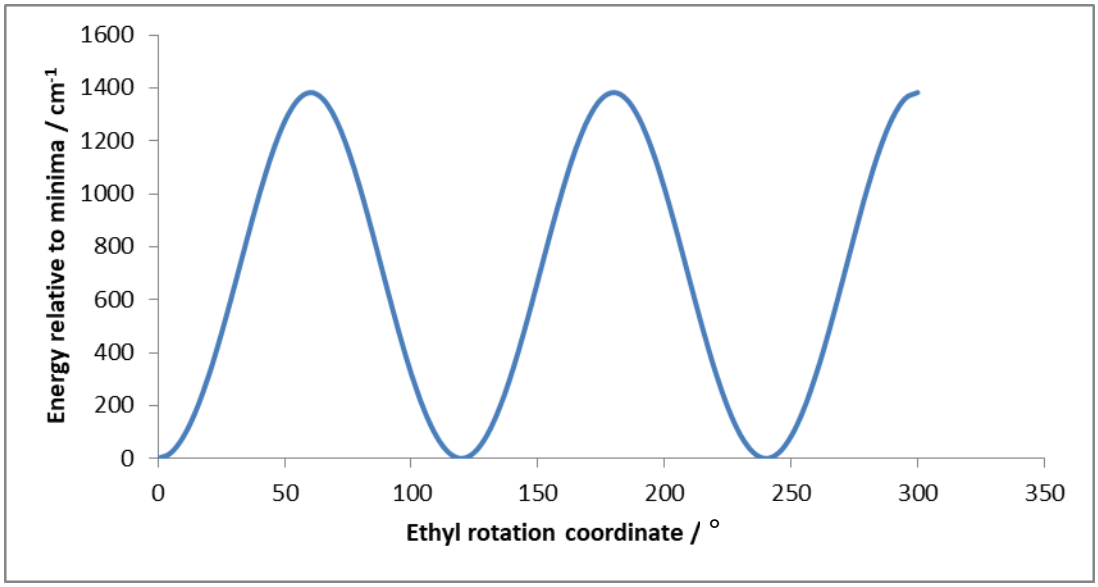

Figure 5-14: S_1 and cation state potential energy surface of the ethyl rotation coordinate.

The NH_2 inversion shows a double well potential surface, with slight asymmetry in the S_1 state. I did both CIS and TD-DFT calculations for this state and they showed two different minima of 0 and 1 cm^{-1} relative energy and 0 and 35 cm^{-1} respectively. Separated by a barrier of 236 and 524 cm^{-1} for each calculation. Important to note that these were relaxed geometry scans, and that the DFT calculation adopted the *gauche* arrangement of the ester group throughout.

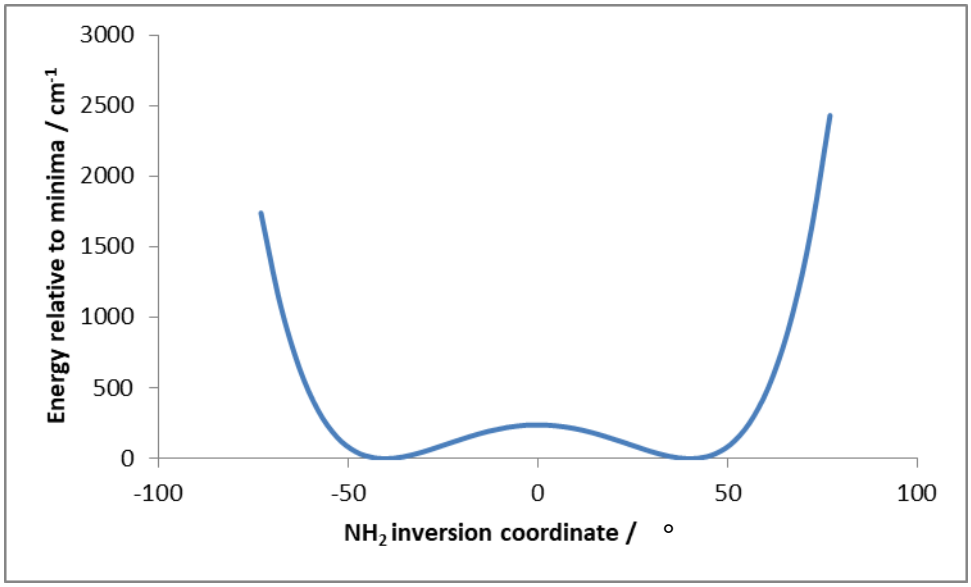

Figure 5-15: S_1 state potential energy surface of the NH_2 inversion coordinate.

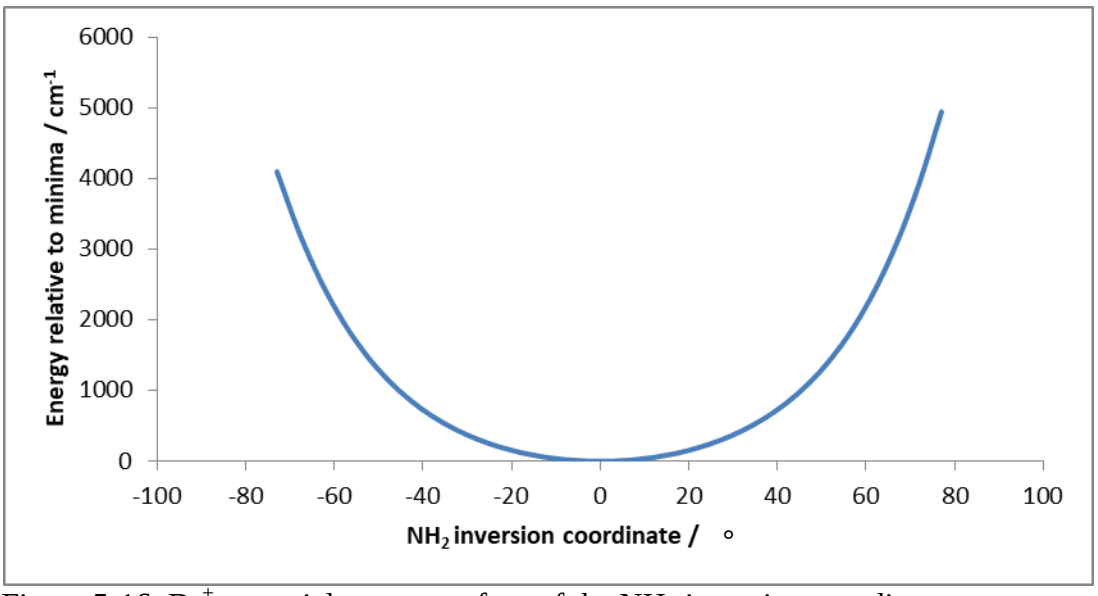

Figure 5-16: D_0^+ potential energy surface of the NH_2 inversion coordinate.

The cation showed a simple minimum of a planar NH_2.

Tunnelling can occur over a range of barrier energies, and was recorded with barriers of up 5890 cm^{-1} in tropolone, by the Zheng group.[130, 131] In general though, the larger the barrier the lower the likelihood of tunnelling occurring. For this reason, the amino inversion looks to be the more likely cause. Combined with the relative predicted frequencies of the inversion and methyl rotation vibrations and the position of the main feature in the ZEKE spectrum, I am confident in my assignment of this vibration to that of the inversion mode. I suspect that the cation planar amino group calculated is actually incorrect, and the cation state is actually quasi-planar, with two slightly different conformers forming, separated by a small energy barrier. As we

excite the inversion mode in the S_1 state we then access both conformers in the cation, leading to the two sets of peaks we see for each vibration. The asymmetrical appearance of the peaks could suggest that a slight asymmetry of the molecule, perhaps due to an out of plane substituent, would give slightly different energies depending on which side of the "planar" molecule the hydrogens are bending towards.

To definitively assign this vibrational mode the best method would be to isotopically label the amine group. A deuterated amine should show less splitting as the increased mass has a lower chance of tunnelling. If the spectra remained the same, then the same experiment can be tried with a heavier methyl group.

Previous studies of aniline have also shown this tunnelling effect.[132] In addition a very similar spectrum to this one was shown to occur in PABA, but unfortunately the authors were unable to explain it, although they also assigned the vibration that caused the splitting to inversion of the amino group. [118] These both lead me to believe it is definitely the amino group, rather than the methyl that is responsible for this effect, as neither aniline nor para-amino-benzoic acid contain an alky group that could rotate.

5.4.3.2 ν_{38} pumped ZEKE spectrum

ν_{38} is a rocking motion of the NH_2 group combined with some skeletal vibrations of the ester. Duschinsky analysis of this mode in the ion state (Figure 5-17) shows a strong mixing of ν_{38} and ν_{37}, whose motions are illustrated in Figure 5-10, predicted to occur at 335 cm^{-1} and 378 cm^{-1} respectively.

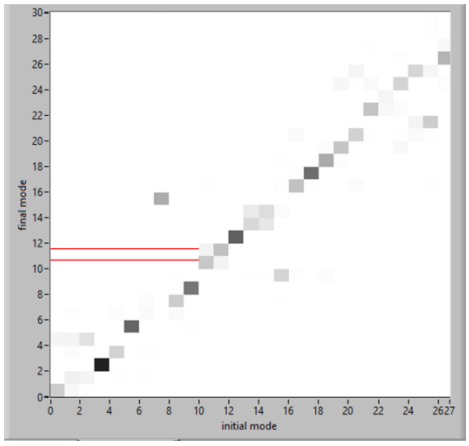

Figure 5-17: Duschinsky mixing of the vibrational modes of benzocaine between the S_0 and D_0^+ states.

This is seen in the ZEKE spectrum of the ν_{38} pumped state, as the presence of two strong features, separated by 19 cm^{-1}, which is close to the predicted gap of the two contributing modes.

5.4.3.3 ν_{58} pumped ZEKE spectrum.

This vibronic intermediate state shows an interesting divergence from the other ZEKE spectra. The vertical transition, the most prominent feature, has moved to a significantly higher frequency region than one might expect. The pump frequency for this mode was 391 cm^{-1}, whereas the highest intensity peak is at 716 cm^{-1}.

A Duschinsky analysis of the vibrational states of the S_0 and D_0^+ was performed, as seen in Figure 5-4. This highlighted one mode in particular that appears at significantly higher frequency in the ion state than the ground. The ν_{58} mode, the out-of-plane rocking motion of the amino hydrogens.

But what could cause such a dramatic frequency shift, of almost double energy? If the vibration is between groups that are much more strongly held together in the ion than the S_1 state, this could lead to a "stiffer" spring, and a higher frequency vibration.

Whilst this mode increases in frequency in the ion, the other vibrational mode to change frequency substantially upon ionisation is the NH_2 inversion, which goes from 561 cm^{-1} in the S_0 state to 333 cm^{-1} in the cation. This implies that inversion becomes an "easier" vibration upon ionisation whilst the twisting mode becomes more difficult. Apparently, the hydrogens are more "locked" into their symmetrical position with respect to the ring plane, once an electron has been removed. This is commensurate with a planar or pseudo planar state.

5.4.3.4 ν_{36} pumped ZEKE spectra

The ν_{36} pumped ZEKE spectrum has a noisier baseline than the others recorded. Castano *et al* attributed this to an intramolecular vibrational energy redistribution process occurring,[57] and found that the increased background intensity grew with the frequency of the intermediate state. This is in part why I chose to focus on the lower intensity, but also lower frequency vibrational intermediate modes. Interestingly, there is no vibrational progression of this mode past the $\Delta v=0$ peak.

5.4.3.5 Ionisation energy

The ionisation energy, I.E, was experimentally found to be 63 245 cm^{-1}. A comparison to other published ionisation energies of amino benzenes we see a destabilisation of the cation upon substitution. Aniline has an I.E of 62 395 cm^{-1},[124, 126] and PABA 64 540 cm^{-1}.[118] The HOMO of benzocaine is a π orbital with significant delocalisation of the nitrogen lone pair electrons. The carboxylic acid, in the case of PABA, and the ethyl ester in the case of benzocaine appear to be acting as electron-withdrawing substituents which raise the relative energy of the cation, particularly once the electron-donating character of the amino group is reduced upon ionisation.

5.5 Conclusions

The majority of the geometry change upon two photon ionisation of benzocaine occurs during the initial excitation step to the S_1 state. This includes strong distortion along two main coordinates: the hydrogens of the amino group move from a pyramidal orientation towards the plane of the ring. The degree of planarity in the S_1 state is still inconclusive as different levels of theory and computational methods gave conflicting results, which were not definitively proved by the experimental results. Secondly, there was a relaxation of the ester group, bending away from the ring system, and indicating a decrease in ring delocalisation upon excitation and ionisation.

The ZEKE spectra collected from a variety of pumped S_1 vibronic states showed strong Duschinsky mixing of the vibrations upon ionisation, seen as the presence of multiple strong features. Many vibrational frequencies shifting dramatically, particularly those associated with the amino group, suggesting that the nitrogen lone pair is heavily involved in the electronic transitions taking place, leading to large changes in bond strength seen as vibrational frequency shifts. Other interesting features arose, including the suspected quantum tunnelling of the amino hydrogens in the cation state, indicative of a slightly non-planar cation, contrary to the calculations. It seems that adding a quantum of vibrational energy to any normal mode in the intermediate state contributes to a far more interesting ZEKE spectrum. Each spectrum collected has turned up unique pieces of information, that could all be the basis for further study.

There is still so much to discover about this critical medicinal molecule, it's geometries in the excited and ion states are far from perfectly understood, and as a molecule often used as a topical anaesthetic, within the reach of sunlight that could easily make these electronic levels accessible, this is surely something that should continue to be explored. Much work has been done on benzocaine as a component of

weakly bound complexes in the past.[30, 31, 58] Whilst the time-constraints of this project meant that I was unable to perform the cluster experiments that were planned, an ammonia study would fit wonderfully into current gaps in the literature. It would likely be a highly interesting project, drawing together the exciting spectroscopy of benzocaine with the opportunity for excellent hydrogen bonding to the amino group or the ester group to further investigate weak interactions in the gas phase.

Chapter 6. Concluding remarks

This work has enhanced our understanding of the electronic and vibrational activity of two molecules: anethole and benzocaine.

The study of anethole was detailed and relatively complete. The work produced in this thesis serves as an excellent foundation to understanding the conformational differences of the *syn* and *anti* conformers, in particular, their responses to subtly different electronic changes upon initial photoexcitation. A future, complementary, study would be to focus on the relaxation dynamics of the S_1 state, *via* a time-resolved study, to observe any conformational variations there. A pump-probe experiment wherein a time delay is introduced between the first and second absorbed photon would track the lifetimes of the excited state for each conformer.

An additional area for exploration is a continuation of the van der Waals study. A possible first step would be the study of the water-anethole cluster, which was detected on our mass spectrometer during this work, showing the ease with which it could be formed, but was not studied within the scope of this project. Study of the increasingly large water clusters would act as a bridge toward solution-phase understanding of this molecule.

The work on benzocaine described in Chapter 5 has many more avenues for further investigation. Each ZEKE spectra recorded contained new vibrational assignments, large changes in vibrational activity upon photoexcitation and ionisation or most surprisingly the presence of apparent quantum tunnelling. The appearance of suspected quantum tunnelling of the amino hydrogens was a surprising result that warrants much further investigation. A potential experiment to further explore this would be to study the deuterated analogues of benzocaine, by observing how the splitting changes with heavier hydrogens attached to the nitrogen atom, the amino group could be confirmed as the cause of the splitting.

Another area that warrants further study is the relationship between different vibrational modes, which is presently far from well-understood. The Duschinsky analysis presented here does start to find some links between modes, but these could be reinforced by the acquisition of additional ZEKE spectra. Ideally these could be acquired using a different laser set-up, using an optical parametric oscillator (OPO) which would allow a greater continuous wavelength range to be covered, although at the cost of much lower laser power. Of particular interest are the higher intensity features present in the REMPI spectrum, including that assigned to a double quanta excitation of the inversion mode at 581 cm^{-1}. Taking a ZEKE spectrum using this vibronic level as an intermediate state would confirm the accuracy of the REMPI vibrational reassignments. To accompany the further ZEKE experiments a deeper look into the computational work would be incredibly helpful. Both the nucleic and electronic structure of the excited state are still not well described by the

calculations, nor is the exact geometry of the cation, which, due to the splitting seen, is now suspected of being quasi-planar. A better computational study would hopefully yield more accurate simulated REMPI and ZEKE spectra, to make the arguments presented in this work more convincing.

Beyond expanding on the pure benzocaine studies, as with anethole it would be very interesting to examine other weakly-bound clusters that are not yet covered by the literature. The ammonia-benzocaine cluster would be the major interest, as the potential for strong hydrogen bonds to form between the solvent and the amino group could lead to an in-plane solvation site. This would be interesting to study due to the uncertainty regarding the planarity of the excited and cationic states, an in-plane bound ammonia would likely have distinctive spectral features seen as the planarity of the host molecule does, or does not, change upon photoabsorption.

This underlines the importance of further study of van der Waals clusters in the gas phase. The use of a probe molecule to track changes in a larger target molecule is an excellent technique for gas-phase spectroscopists, which I'm sure will continue to yield extraordinary results for many years to come.

Chapter 7. References

1. S. Hashimoto and H. Akimoto, *Journal of Physical Chemistry*, 1989, **93**, 571-577.
2. C. Int Agcy Res, *Iarc Monographs on the Evaluation of Carcinogenic Risks to Humans, Vol 55: Solar and Ultraviolet Radiation*, 1992, **55**, 217-228.
3. J. D'Orazio, S. Jarrett, A. Amaro-Ortiz and T. Scott, *International Journal of Molecular Sciences*, 2013, **14**, 12222-12248.
4. J. Teichmann and A. Stinner, *Annals of Science*, 2014, **71**, 27-60.
5. N. Bohr, *Philosophical Magazine*, 1913, **26**, 476-502.
6. E. Schrodinger, *Physical Review*, 1926, **28**, 1049-1070.
7. J. Hecht, *Optical Engineering*, 2010, **49**.
8. S. Hufner, S. Schmidt and F. Reinert, *Nuclear Instruments & Methods in Physics Research Section a-Accelerators Spectrometers Detectors and Associated Equipment*, 2005, **547**, 8-23.
9. M. C. R. Cockett, *Chemical Society Reviews*, 2005, **34**, 935-948.
10. G. M. Sando and K. G. Spears, *Journal of Physical Chemistry A*, 2001, **105**, 5326-5333.
11. F. Duschinsky, *Acta Physicochimica Urss*, 1937, **7**, 551-566.
12. A. M. Mebel, M. Hayashi, K. K. Liang and S. H. Lin, *Journal of Physical Chemistry A*, 1999, **103**, 10674-10690.
13. K. Müller-Dethlefs and P. Hobza, *Chemical Reviews*, 2000, **100**, 143-167.
14. P. Hobza, R. Zahradník and K. Müller-Dethlefs, *Collection of Czechoslovak Chemical Communications*, 2006, **71**, 443-531.
15. E. D. Glowacki, M. Irimia-Vladu, S. Bauer and N. S. Sariciftci, *Journal of Materials Chemistry B*, 2013, **1**, 3742-3753.
16. A. M. Sweetman, S. P. Jarvis, H. Q. Sang, I. Lekkas, P. Rahe, Y. Wang, J. B. Wang, N. R. Champness, L. Kantorovich and P. Moriarty, *Nature Communications*, 2014, **5**.
17. C. B. Aakeroy and K. R. Seddon, *Chemical Society Reviews*, 1993, **22**, 397-407.
18. D. Herschlag and M. M. Pinney, *Biochemistry*, 2018, **57**, 3338-3352.
19. S. Albertini, E. Gruber, F. Zappa, S. Krasnokutskiy, F. Laimer and P. Scheier, *Mass Spectrometry Reviews*, 2022, **41**, 529-567.
20. C. E. H. Dessent and K. Muller-Dethlefs, *Chemical Reviews*, 2000, **100**, 3999-4021.
21. C. Kang and D. W. Pratt, *International Reviews in Physical Chemistry*, 2005, **24**, 1-36.
22. A. Gaber, M. Riese, F. Witte and J. Grotemeyer, *European Journal of Mass Spectrometry*, 2009, **15**, 349-359.
23. N. M. Tonge, E. C. MacMahon, I. Pugliesi and M. C. R. Cockett, *Journal of Chemical Physics*, 2007, **126**.
24. W. Kohn, Y. Meir and D. E. Makarov, *Physical Review Letters*, 1998, **80**, 4153-4156.
25. T. Thonhauser, V. R. Cooper, S. Li, A. Puzder, P. Hyldgaard and D. C. Langreth, *Physical Review B*, 2007, **76**.

26. P. Kolandaivel, D. U. Maheswari and L. Senthilkumar, *Computational and Theoretical Chemistry*, 2013, **1004**, 56-60.
27. E. Derbali, Y. Ajili, B. Mehnen, P. S. Zuchowski, D. Kedziera, M. M. Al-Mogren, N. E. Jaidane and M. Hochlaf, *Physical Chemistry Chemical Physics*, 2023.
28. Y. N. Kalugina, I. A. Buryak, Y. Ajili, A. A. Vigasin, N. E. Jaidane and M. Hochlaf, *Journal of Chemical Physics*, 2014, **140**.
29. M. B. Robin, presented in part at the Chemical Spectroscopy and Photochemistry in the Vacuum-Ultraviolet, Dordrecht, August 1974.
30. J. A. Fernandez, A. Longarte, I. Unamuno and F. Castano, *Journal of Chemical Physics*, 2000, **113**, 8531-8540.
31. I. Leon, E. Aguado, A. Lesarri, J. A. Fernandez and F. Castano, *Journal of Physical Chemistry A*, 2009, **113**, 982-988.
32. A. Longarte, J. A. Fernandez, I. Unamuno and F. Castano, *Chemical Physics*, 2000, **260**, 83-93.
33. T. Kamisuki, H. Kataoka and S. Maeda, *Spectrochimica Acta Part a-Molecular and Biomolecular Spectroscopy*, 1998, **54**, 277-284.
34. D. Jacquemin and C. Adamo, *Density-Functional Methods for Excited States*, 2016, **368**, 347-375.
35. I. Y. Zhang and A. Grüneis, *Frontiers in Materials*, 2019, **6**.
36. A. J. Kulesza, E. Titov, S. Daly, R. Wlodarczyk, J. Megow, P. Saalfrank, C. M. Choi, L. MacAleese, R. Antoine and P. Dugourd, *Chemphyschem*, 2016, **17**, 3129-3138.
37. I. Pugliesi and K. Muller-Dethlefs, *Journal of Physical Chemistry A*, 2006, **110**, 13045-13057.
38. P. Gnida, M. F. Amin, A. K. Pajak and B. Jarzabek, *Polymers*, 2022, **14**, 39.
39. T. Verbiest, S. Houbrechts, M. Kauranen, K. Clays and A. Persoons, *Journal of Materials Chemistry*, 1997, **7**, 2175-2189.
40. D. Quinonero, A. Frontera and P. M. Deya, *Computational and Theoretical Chemistry*, 2012, **998**, 51-56.
41. M. Ghasemi-Dehnoo, A. A. Safari, M. Rahimi-Madiseh, Z. Lorigooini, M. T. Moradi and H. Amini-Khoei, *Evidence-Based Complementary and Alternative Medicine*, 2022, **2022**.
42. Y. Caoa, Q. Zhonga, F. Tanga, X. Yaoa, Z. Liua and X. Zhangb, *Allergologia Et Immunopathologia*, 2022, **50**, 107-114.
43. S. M. Vastegani, S. E. Khoshnam, E. Mansouri, S. Ghafouri, N. Bakhtiari, Y. Farbood and A. Sarkaki, *Metabolic Brain Disease*, 2023, **38**, 2159-2174.
44. J. Li, Y. Mao and W. Li, *Tropical Journal of Pharmaceutical Research*, 2022, **21**, 2391-2396.
45. F. Sadeghzadeh, H. N. Haghighi, M. Ghiyamati, F. Hajizadenadaf and M. H. Tabrizi, *Cancer Nanotechnology*, 2023, **14**, 15.
46. S. Harakeh, R. Al-Raddadi, T. Alamri, S. Al-Jaouni, M. Qari, Y. Qari, A. Kumar, H. M. Tashkandi, M. Moulay, A. M. Aldahlawi, P. Slama and S. Haque, *Biomedicine & Pharmacotherapy*, 2023, **165**.
47. F. K. He, K. K. Jin, Y. Q. Wang, J. J. Wang, J. F. Zhou, J. Sun and Q. Fang, *Acs Sustainable Chemistry & Engineering*, 2017, **5**, 2578-2584.
48. S. Mukherjee, M. Choi and J. W. Yun, *Biotechnology and Bioprocess Engineering*, 2022, **27**, 938-948.
49. A. Semlali, I. Ajala, S. Beji, M. M. Al-Zharani and M. Rouabhia, *Pharmaceuticals*, 2023, **16**.

50. E. M. Teobaldo da Rocha, L. Bracht, O. H. Goncalves, F. V. Leimann, F. Q. Ames, L. C. Lauer Schneider, J. V. Duda, G. F. Esteves Cardia, C. I. Bonetti, R. K. Nakamura Cuman and C. A. Bersani-Amado, *Naunyn-Schmiedebergs Archives of Pharmacology*, 2023, **396**, 469-484.
51. Y. Tong, C. Yu, Z. Xie, X. Zhang, Z. Yang and T. Wang, *Poultry Science*, 2022, **101**.
52. Y. Tong, C. Yu, S. Chen, X. Zhang, Z. Yang and T. Wang, *Poultry Science*, 2023, **102**.
53. B. Wang, G. Zhang, M. Yang, N. Liu, Y.-X. Li, H. Ma, L. Ma, T. Sun, H. Tan and J. Yu, *Neurochemical Research*, 2018, **43**, 2404-2422.
54. N. S. Younis and M. E. Mohamed, *Pharmaceuticals*, 2023, **16**.
55. C. Yu, T. Wang and Z. Yang, *Italian Journal of Animal Science*, 2022, **21**, 729-736.
56. C. Yu, Y. Tong, Q. Li, T. Wang and Z. Yang, *Frontiers in Veterinary Science*, 2022, **9**.
57. E. Aguado, A. Longarte, E. Alejandro, J. A. Fernandez and F. Castano, *Journal of Physical Chemistry A*, 2006, **110**, 6010-6015.
58. E. Aguado, I. Leon, E. J. Cocinero, A. Lesarri, J. A. Fernandez and F. Castano, *Physical Chemistry Chemical Physics*, 2009, **11**, 11608-11616.
59. E. Aguado, I. Leon, J. Millan, E. J. Cocinero, S. Jaeqx, A. M. Rijs, A. Lesarri and J. A. Fernandez, *Journal of Physical Chemistry B*, 2013, **117**, 13472-13480.
60. K. Balci and S. Akyuz, *Vibrational Spectroscopy*, 2008, **48**, 215-228.
61. R. E. Smalley, B. L. Ramakrishna, D. H. Levy and L. Wharton, *Journal of Chemical Physics*, 1974, **61**, 4363-4364.
62. M. V. Johnston, *Trac-Trends in Analytical Chemistry*, 1984, **3**, 58-61.
63. K. Luria, W. Christen and U. Even, *Journal of Physical Chemistry A*, 2011, **115**, 7362-7367.
64. J. Koperski and M. Czajkowski, *Physical Review A*, 2000, **62**.
65. T. Koopmans, *Physica*, 1934, **1**, 104-113.
66. B. Buijsse and W. J. van der Zande, *Faraday Discussions*, 1997, **108**, 271-286.
67. M. J. J. Vrakking, *Molecular Rydberg Dynamics*, 1999, 229-232.
68. K. Takazawa, M. Fujii, T. Ebata and M. Ito, *Chemical Physics Letters*, 1992, **189**, 592-597.
69. G. Reiser, W. Habenicht and K. Mullerdethlefs, *Journal of Chemical Physics*, 1993, **98**, 8462-8468.
70. H. J. Dietrich, K. MullerDethlefs and L. Y. Baranov, *Physical Review Letters*, 1996, **76**, 3530-3533.
71. E. Epifanovsky, A. T. B. Gilbert, X. T. Feng, J. Lee, Y. Z. Mao, N. Mardirossian, P. Pokhilko, A. F. White, M. P. Coons, A. L. Dempwolff, Z. T. Gan, D. Hait, P. R. Horn, L. D. Jacobson, I. Kaliman, J. Kussmann, A. W. Lange, K. U. Lao, D. S. Levine, J. Liu, S. C. McKenzie, A. F. Morrison, K. D. Nanda, F. Plasser, D. R. Rehn, M. L. Vidal, Z. Q. You, Y. Zhu, B. Alam, B. J. Albrecht, A. Aldossary, E. Alguire, J. H. Andersen, V. Athavale, D. Barton, K. Begam, A. Behn, N. Bellonzi, Y. A. Bernard, E. J. Berquist, H. G. A. Burton, A. Carreras, K. Carter-Fenk, R. Chakraborty, A. D. Chien, K. D. Closser, V. Cofer-Shabica, S. Dasgupta, M. de Wergifosse, J. Deng, M. Diedenhofen, H. Do, S. Ehlert, P. T. Fang, S. Fatehi, Q. G. Feng, T. Friedhoff, J. Gayvert, Q. H. Ge, G. Gidofalvi, M. Goldey, J. Gomes, C. E.

Gonzalez-Espinoza, S. Gulania, A. O. Gunina, M. W. D. Hanson-Heine, P. H. P. Harbach, A. Hauser, M. F. Herbst, M. H. Vera, M. Hodecker, Z. C. Holden, S. Houck, X. K. Huang, K. Hui, B. C. Huynh, M. Ivanov, A. Jasz, H. Ji, H. J. Jiang, B. Kaduk, S. Kahler, K. Khistyaev, J. Kim, G. Kis, P. Klunzinger, Z. Koczor-Benda, J. H. Koh, D. Kosenkov, L. Koulias, T. Kowalczyk, C. M. Krauter, K. Kue, A. Kunitsa, T. Kus, I. Ladjanszki, A. Landau, K. V. Lawler, D. Lefrancois, S. Lehtola, R. R. Li, Y. P. Li, J. S. Liang, M. Liebenthal, H. H. Lin, Y. S. Lin, F. L. Liu, K. Y. Liu, M. Loipersberger, A. Luenser, A. Manjanath, P. Manohar, E. Mansoor, S. F. Manzer, S. P. Mao, A. V. Marenich, T. Markovich, S. Mason, S. A. Maurer, P. F. McLaughlin, M. Menger, J. M. Mewes, S. A. Mewes, P. Morgante, J. W. Mullinax, K. J. Oosterbaan, G. Paran, A. C. Paul, S. K. Paul, F. Pavosevic, Z. Pei, S. Prager, E. I. Proynov, A. Rak, E. Ramos-Cordoba, B. Rana, A. E. Rask, A. Rettig, R. M. Richard, F. Rob, E. Rossomme, T. Scheele, M. Scheurer, M. Schneider, N. Sergueev, S. M. Sharada, W. Skomorowski, D. W. Small, C. J. Stein, Y. C. Su, E. J. Sundstrom, Z. Tao, J. Thirman, G. J. Tornai, T. Tsuchimochi, N. M. Tubman, S. P. Veccham, O. Vydrov, J. Wenzel, J. Witte, A. Yamada, K. Yao, S. Yeganeh, S. R. Yost, A. Zech, I. Y. Zhang, X. Zhang, Y. Zhang, D. Zuev, A. Aspuru-Guzik, A. T. Bell, N. A. Besley, K. B. Bravaya, B. R. Brooks, D. Casanova, J. D. Chai, S. Coriani, C. J. Cramer, G. Cserey, A. E. DePrince, R. A. DiStasio, A. Dreuw, B. D. Dunietz, T. R. Furlani, W. A. Goddard, S. Hammes-Schiffer, T. Head-Gordon, W. J. Hehre, C. P. Hsu, T. C. Jagau, Y. S. Jung, A. Klamt, J. Kong, D. S. Lambrecht, W. Z. Liang, N. J. Mayhall, C. W. McCurdy, J. B. Neaton, C. Ochsenfeld, J. A. Parkhill, R. Peverati, V. A. Rassolov, Y. H. Shao, L. V. Slipchenko, T. Stauch, R. P. Steele, J. E. Subotnik, A. J. W. Thom, A. Tkatchenko, D. G. Truhlar, T. Van Voorhis, T. A. Wesolowski, K. B. Whaley, H. L. Woodcock, P. M. Zimmerman, S. Faraji, P. M. W. Gill, M. Head-Gordon, J. M. Herbert and A. I. Krylov, *Journal of Chemical Physics*, 2021, **155**, 59.

72. P. Deglmann, A. Schäfer and C. Lennartz, *International Journal of Quantum Chemistry*, 2015, **115**, 107-136.
73. C. Moller and M. S. Plesset, *Physical Review*, 1934, **46**, 0618-0622.
74. R. J. Bartlett and M. Musial, *Reviews of Modern Physics*, 2007, **79**, 291-352.
75. E. Valderrama, X. Fradera and J. M. Ugalde, *Journal of Chemical Physics*, 2001, **115**, 1987-1994.
76. A. D. Becke, *Journal of Chemical Physics*, 1993, **98**, 5648-5652.
77. M. Walker, A. J. A. Harvey, A. Sen and C. E. H. Dessent, *Journal of Physical Chemistry A*, 2013, **117**, 12590-12600.
78. O. Christiansen, H. Koch and P. Jorgensen, *Chemical Physics Letters*, 1995, **243**, 409-418.
79. A. P. Scott and L. Radom, *Journal of Physical Chemistry*, 1996, **100**, 16502-16513.
80. T. van Mourik, *Journal of Physical Chemistry A*, 2008, **112**, 11017-11020.
81. J. O. Baum and J. L. Finney, *Molecular Physics*, 1985, **55**, 1097-1108.
82. S. F. Boys and F. Bernardi, *Molecular Physics*, 1970, **19**, 553-558.
83. R. Krishnan, J. S. Binkley, R. Seeger and J. A. Pople, *Journal of Chemical Physics*, 1980, **72**, 650-654.
84. T. H. Dunning, *Journal of Chemical Physics*, 1989, **90**, 1007-1023.

85. F. Weigend and R. Ahlrichs, *Physical Chemistry Chemical Physics*, 2005, **7**, 3297-3305.
86. M. J. Frisch, G. W. Trucks, H. B. Schlegel, G. E. Scuseria, M. A. Robb, J. R. Cheeseman, G. Scalmani, V. Barone, G. A. Petersson, H. Nakatsuji, X. Li, M. Caricato, A. V. Marenich, J. Bloino, B. G. Janesko, R. Gomperts, B. Mennucci, H. P. Hratchian, J. V. Ortiz, A. F. Izmaylov, J. L. Sonnenberg, Williams, F. Ding, F. Lipparini, F. Egidi, J. Goings, B. Peng, A. Petrone, T. Henderson, D. Ranasinghe, V. G. Zakrzewski, J. Gao, N. Rega, G. Zheng, W. Liang, M. Hada, M. Ehara, K. Toyota, R. Fukuda, J. Hasegawa, M. Ishida, T. Nakajima, Y. Honda, O. Kitao, H. Nakai, T. Vreven, K. Throssell, J. A. Montgomery Jr., J. E. Peralta, F. Ogliaro, M. J. Bearpark, J. J. Heyd, E. N. Brothers, K. N. Kudin, V. N. Staroverov, T. A. Keith, R. Kobayashi, J. Normand, K. Raghavachari, A. P. Rendell, J. C. Burant, S. S. Iyengar, J. Tomasi, M. Cossi, J. M. Millam, M. Klene, C. Adamo, R. Cammi, J. W. Ochterski, R. L. Martin, K. Morokuma, O. Farkas, J. B. Foresman, D. J. Fox and C. Gaussian 16 Rev. C.01 Wallingford, 2016.
87. J. B. Lena, A. M. van Herk and S. Jana, *Polymer Chemistry*, 2020, **11**, 5630-5641.
88. K. Fujimori, W. S. Schiller and I. E. Craven, *Makromolekulare Chemie-Macromolecular Chemistry and Physics*, 1991, **192**, 959-966.
89. R. Javed, M. A. Hanif, M. A. Ayub and R. Rehman, *Medicinal Plants of South Asia*, Elsevier Ltd, Pakistan, 1 edn., 2020.
90. *United States Pat.* 4026951, 1974.
91. I. Kubo, K. Fujita and K. Nihei, *Journal of the Science of Food and Agriculture*, 2008, **88**, 242-247.
92. P. Newberne, R. L. Smith, J. Doull, J. I. Goodman, I. C. Munro, P. S. Portoghese, B. M. Wagner, C. S. Weil, L. A. Woods, T. B. Adams, C. D. Lucas and R. A. Ford, *Food and Chemical Toxicology*, 1999, **37**, 789-811.
93. D. Carteau, D. Bassani and I. Pianet, *Comptes Rendus Chimie*, 2008, **11**, 493-498.
94. R. Llinares, P. Ramírez, J. Carmona, F. Carrillo and J. Munñoz, *Colloids and Surfaces a-Physicochemical and Engineering Aspects*, 2018, **536**, 142-147.
95. V. H. Grassian, E. R. Bernstein, H. V. Secor and J. I. Seeman, *Journal of Physical Chemistry*, 1989, **93**, 3470-3474.
96. V. P. Barber and J. J. Newby, *Journal of Physical Chemistry A*, 2013, **117**, 12831-12841.
97. F. Weigend, A. Kohn and C. Hattig, *Journal of Chemical Physics*, 2002, **116**, 3175-3183.
98. C. Hattig and F. Weigend, *Journal of Chemical Physics*, 2000, **113**, 5154-5161.
99. M. Frisch, G. Trucks, H. Schlegel, G. Scuseria, M. Robb, J. Cheeseman, G. Scalmani, V. Barone, G. Petersson, H. Nakatsuji, X. Li, L. Caricato, A. Marenich, J. Bloino, B. Janesko, R. Gomperts, B. Mennucci, H. Hratchian, J. Ortiz, H. Izmaylov, J. Sonnenberg, J. Williams-Young, F. Ding, F. Lipparini, F. Egidi, J. Goings, B. Peng, A. Petrone, T. Henderson, B. Ranasinghe, V. Zakrzewski, J. Gao, N. Rega, G. Zheng, M. Liang, M. Hada, M. Ehara, K. Toyota, R. Fukuda, J. Hasegawa, M. Ishida, T. Nakajima, Y. Honda, O. Kitao, H. Nakai, T. Vreven, K. Throssell, J. Montgomery, J. Peralta, F. Ogliaro, M. Bearpark, J. Heyd, E. Brothers, K. Kudin, V. Staroverov, T. Keith, R. Kobayashi, J. Normand, K. Raghavachari, A. Rendell, J. Burant, S.

Iyengar, J. Tomasi, M. Cossi, J. Millam, M. Klene, C. Adamo, R. Cammi, J. Ochterski, R. Martin, K. Morokuma, O. Farkas, J. Foresman and D. Fox, 2016, **A.03**.
100. N. O. C. Winter, N. K. Graf, S. Leutwyler and C. Hattig, *Physical Chemistry Chemical Physics*, 2013, **15**, 6623-6630.
101. G. Orlandi and W. Siebrand, *Journal of Chemical Physics*, 1973, **58**, 4513-4523.
102. I. Pugliesi, N. M. Tonge and M. C. R. Cockett, *Journal of Chemical Physics*, 2008, **129**, 17.
103. R. J. Moulds, M. A. Buntine and W. D. Lawrance, *Journal of Chemical Physics*, 2004, **121**, 4635-4641.
104. K. Kimura, *Journal of the Chinese Chemical Society*, 2001, **48**, 433-438.
105. M. S. Ford, X. Tong, C. E. H. Dessent and K. Müller-Dethlefs, *Journal of Chemical Physics*, 2003, **119**, 12914-12920.
106. J. L. C. Fajin, J. L. Cacheiro, B. Fernandez and J. Makarewicz, *Journal of Chemical Physics*, 2004, **120**, 8582-8586.
107. H. Koch, B. Fernandez and O. Christiansen, *Journal of Chemical Physics*, 1998, **108**, 2784-2790.
108. H. Koch, B. Fernandez and J. Makarewicz, *Journal of Chemical Physics*, 1999, **111**, 198-204.
109. F. Mazzoni, M. Becucci, J. Rezac, D. Nachtigallova, F. Michels, P. Hobza and K. Muller-Dethlefs, *Physical Chemistry Chemical Physics*, 2015, **17**, 12530-12537.
110. E. Heid, P. A. Hunt and C. Schröder, *Physical Chemistry Chemical Physics*, 2018, **20**, 8554-8563.
111. F. C. Grozema, R. Telesca, H. T. Jonkman, L. D. A. Siebbeles and J. G. Snijders, *Journal of Chemical Physics*, 2001, **115**, 10014-10021.
112. S. Bouzon and B. Fernandez, *Journal of Physical Chemistry A*, 2009, **113**, 5212-5216.
113. G. A. Olah, *Journal of Organic Chemistry*, 2001, **66**, 5943-5957.
114. M. F. Perutz, G. Fermi, D. J. Abraham, C. Poyart and E. Bursaux, *Journal of the American Chemical Society*, 1986, **108**, 1064-1078.
115. B. D. Howells, J. McCombie, T. F. Palmer, J. P. Simons and A. Walters, *Journal of the Chemical Society-Faraday Transactions*, 1992, **88**, 2587-2594.
116. B. D. Howells, J. McCombie, T. F. Palmer, J. P. Simons and A. Walters, *Journal of the Chemical Society-Faraday Transactions*, 1992, **88**, 2595-2601.
117. R. Pereira, T. Calvo, F. Castano and M. T. Martinez, *Chemical Physics*, 1995, **201**, 433-449.
118. Y. G. He, C. Y. Wu and W. Kong, *Journal of Chemical Physics*, 2004, **121**, 3533-3539.
119. K. Pirowska, P. Kolek, J. Goclon and J. Najbar, *Chemical Physics Letters*, 2004, **387**, 165-175.
120. J. Ray and S. G. Ramesh, *Chemical Physics*, 2018, **515**, 77-87.
121. E. Drougas, J. G. Philis and A. M. Kosmas, *Journal of Molecular Structure-Theochem*, 2006, **758**, 17-20.
122. T. M. Korter, D. R. Borst, C. J. Butler and D. W. Pratt, *Journal of the American Chemical Society*, 2001, **123**, 96-99.

123. R. Montero, I. Lamas, I. Leon, J. A. Fernandez and A. Longarte, *Physical Chemistry Chemical Physics*, 2019, **21**, 3098-3105.
124. W. E. Sinclair and D. W. Pratt, *Journal of Chemical Physics*, 1996, **105**, 7942-7956.
125. M. Becucci, E. Castellucci, I. López-Tocón, G. Pietraperzia, P. R. Salvi and W. Caminati, *Journal of Physical Chemistry A*, 1999, **103**, 8946-8951.
126. Z. H. Qu, Z. B. Qin, X. F. Zheng, H. Wang, G. X. Yao, X. Y. Zhang and Z. F. Cui, *Spectrochimica Acta Part a-Molecular and Biomolecular Spectroscopy*, 2017, **173**, 432-438.
127. S. H. Lin and H. Eyring, *Proceedings of the National Academy of Sciences of the United States of America*, 1974, **71**, 3802-3804.
128. E. B. Wilson, *Physical Review*, 1934, **45**, 0706-0714.
129. H. L. Nguyen, I. Gulaczyk, M. Kreglewski and I. Kleiner, *Coordination Chemistry Reviews*, 2021, **436**.
130. Y. Guo, T. D. Sewell and D. L. Thompson, *Journal of Physical Chemistry A*, 1998, **102**, 5040-5048.
131. K. M. Pei, D. K. Wang and X. M. Zheng, *Journal of Molecular Structure-Theochem*, 2007, **805**, 33-38.
132. D. L. Howard, T. W. Robinson, A. E. Fraser and H. G. Kjaergaard, *Physical Chemistry Chemical Physics*, 2004, **6**, 719-724.

Chapter 8. Appendix

Table 8-1: Typical operating conditions of the REMPI and ZEKE experiments.

Parameter	Typical range
Argon backing pressure	0.1-2.5 bar
Nozzle open duration	200-600 μs
Experimental repetition rate	10 Hz
Data collection average	10 shot average
Laser pulse delay relative to nozzle pulse	200-500 μs
Pre pulse amplitude	500-1500 mV
Pre pulse delay	0-2000 ns
Pre pulse width	50-350 ns
Repeller pulse delay	500-2500 ns
Repeller pulse width	200-300 ns
Repeller pulse amplitude	300-2500 mV
Nozzle operating temperature	20-100 °C
Laser scan step size	0.004 nm

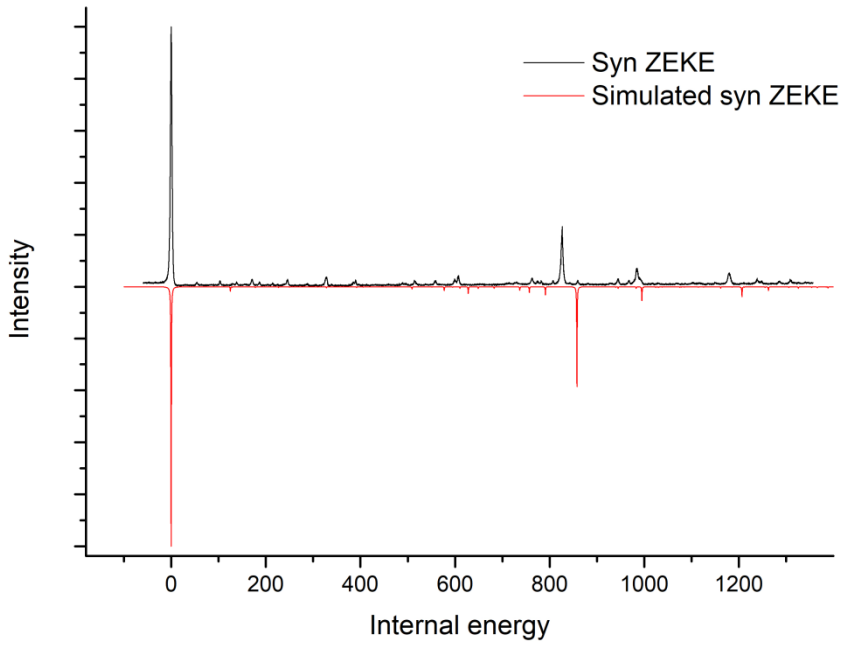

Figure 6-8-1: Simulation of the *syn* anethole origin pumped ZEKE spectrum.

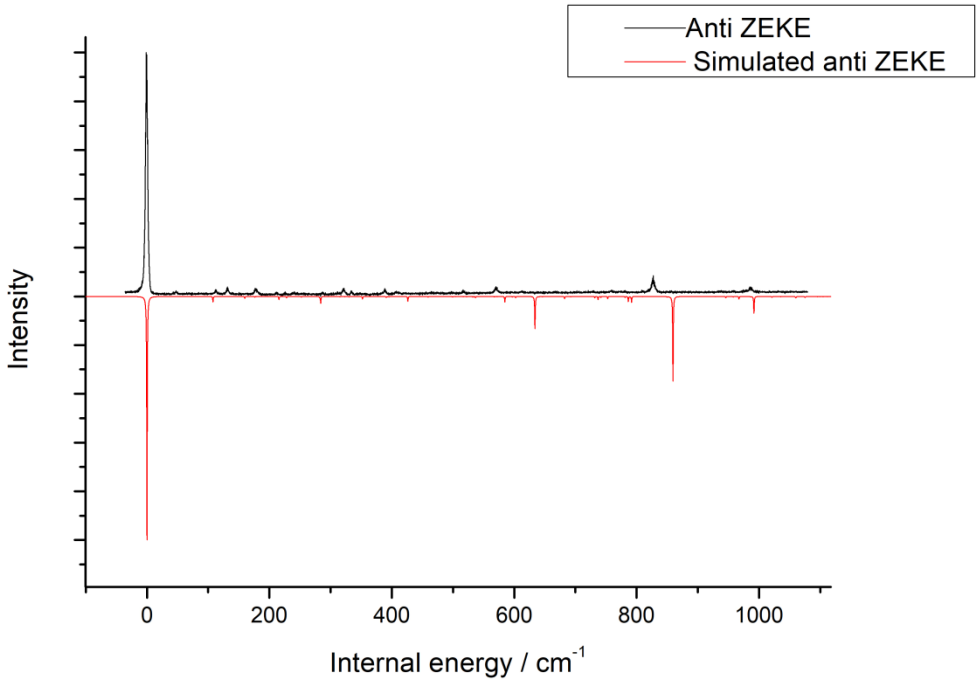

Figure 8-2: Simulation of the *anti* anethole origin pumped ZEKE spectrum.

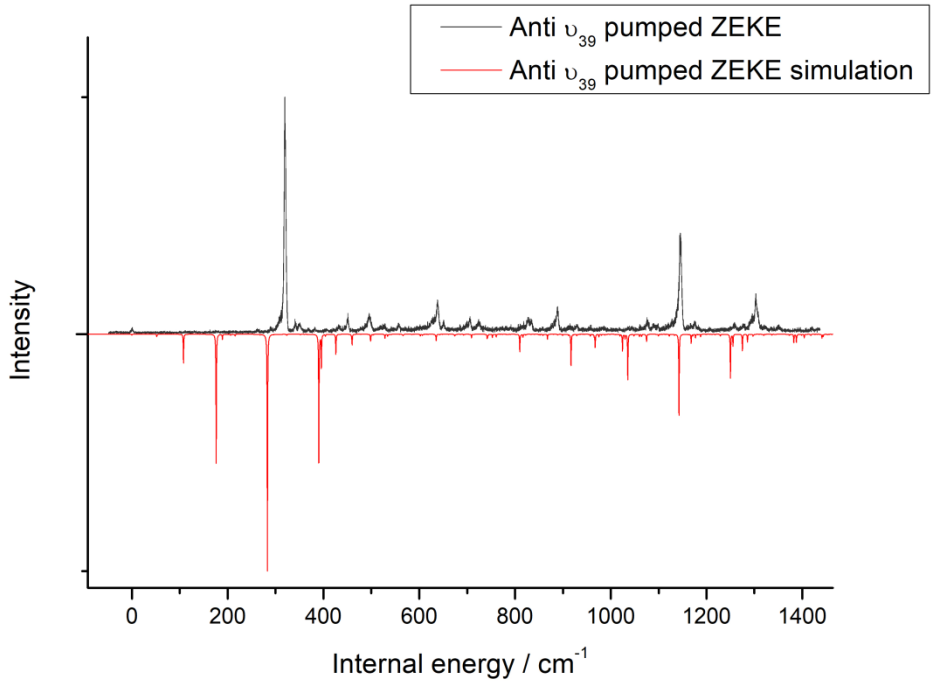

Figure 8-3: *Anti* anethole ZEKE simulation with ν_{39} intermediate state.

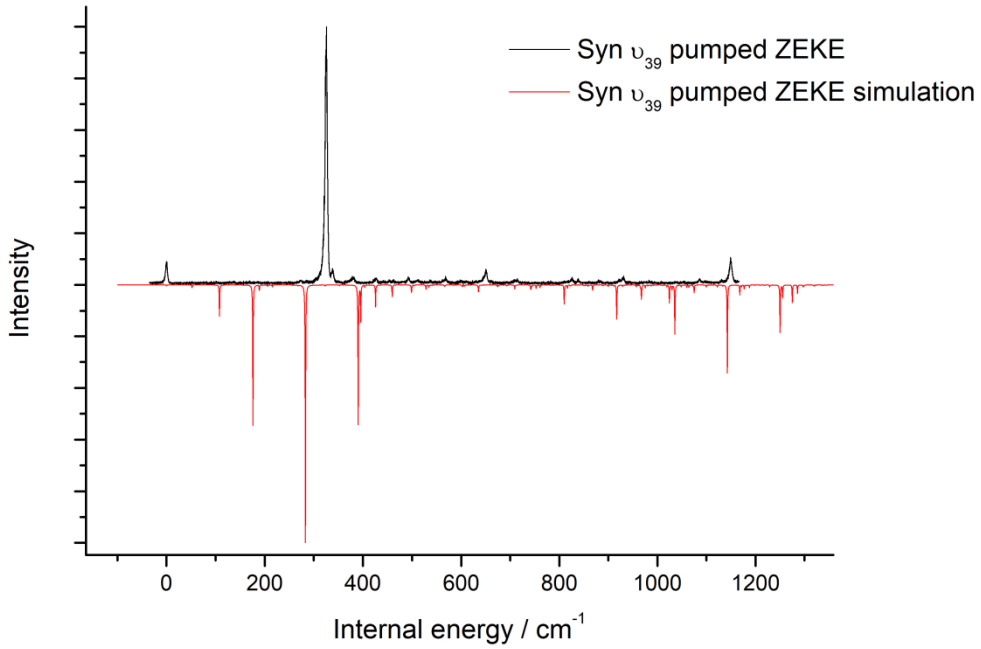

Figure 8-4: *Syn* anethole ZEKE simulation with ν_{39} intermediate state.

Table 6.1: Full assignments of the anethole monomer origin- pumped ZEKE spectra.

	Syn		*Anti*	
Mode	Exp. Freq	Calc freq	Exp. Freq	Calc freq
origin	**0**	0	**0**	0
ν_{63}	55	65	48	52
ν_{62}	105	113	113	114
ν_{41}	130	125	131	108
$\nu_{63} + \nu_{62}$	172	178	178	160
$2\nu_{62}$	214	227	211	216
ν_{40}	246	250	237	
ν_{39}	326	328	320	352
ν_{38}	390	392	388	426
$\nu_{62+} \nu_{56}$	515	509	517	585
ν_{36}	556	577	569	585
$\nu_{59+} \nu_{56}$	600	610	604	
ν_{35}	606	628	611	
$\nu_{57} + \nu_{56}$	713	737		
ν_{34}	729	757		
ν_{56}	763	791	760	
$\nu_{35} + \nu_{60}$	807	838	817	
ν_{33}	826	858	829	858
ν_{32}	945	945	935	

$\nu_{33}+\nu_{41}$	967	983	960	967
ν_{30}	984	995	985	992
ν_{25}	1179	1207		
ν_{24}	1237	1263		
ν_{23}	1286	1306		
ν_{22}	1309	1326		

Table 6.2:Full assignment of the ν_{39} mode pumped anethole ZEKE spectra.

Mode	Exp freq. *Syn*	Exp freq. *Anti*
- ν_{39}	0	0
origin	325	320
$\nu_{63}+\nu_{39}$	379	381
$\nu_{62}+\nu_{39}$	428	432
$\nu_{41}+\nu_{39}$?		451
$\nu_{63}+\nu_{62}+\nu_{39}$	491	495
$\nu_{40}+\nu_{39}$	568	557
$2\nu_{39}$	651	639
$\nu_{38}+\nu_{39}$	711	705
$\nu_{62}+\nu_{56}+\nu_{39}$	839	827
$\nu_{36}+\nu_{39}$	884	887
$\nu_{59}+\nu_{56}+\nu_{39}$	921	915
$\nu_{35}+\nu_{39}$	932	930
$\nu_{56}+\nu_{39}$	1085	1077
$\nu_{39}+\nu_{33}$	1150	1147
$\nu_{39}+\nu_{30}$		1302

Table 6-3: Calculated geometric parameters of anethole

	S_0		S_1		D_0	
Parameter	*Anti*	*Syn*	*Anti*	*Syn*	*Anti*	*Syn*
R(1-2)	1.409	1.41	1.439	1.437	1.424	1.423
R(1-6)	1.414	1.412	1.424	1.428	1.424	1.426
R(1-11)	1.377	1.377	1.362	1.359	1.347	1.346
R(2-3)	1.409	1.4	1.418	1.413	1.394	1.384
R(2-7)	1.091	1.093	1.089	1.091	1.091	1.092
R(3-4)	1.411	1.417	1.442	1.435	1.432	1.439
R(3-8)	1.095	1.095	1.095	1.095	1.093	1.093
R(4-5)	1.419	1.412	1.45	1.459	1.441	1.434
R(4-16)	1.473	1.474	1.431	1.428	1.425	1.426
R(5-6)	1.398	1.407	1.439	1.432	1.384	1.393
R(5-9)	1.093	1.094	1.09	1.09	1.092	1.092

R(6-10)	1.093	1.091	1.093	1.091	1.092	1.091
R(11-12)	1.435	1.435	1.447	1.448	1.459	1.459
R(12-13)	1.103	1.103	1.1	1.1	1.099	1.099
R(12-14)	1.096	1.096	1.095	1.095	1.094	1.094
R(12-15)	1.103	1.103	1.1	1.1	1.099	1.099
R(16-17)	1.099	1.099	1.098	1.098	1.096	1.096
R(16-18)	1.358	1.358	1.382	1.385	1.384	1.383
R(18-19)	1.097	1.097	1.096	1.095	1.095	1.095
R(18-20)	1.503	1.503	1.497	1.497	1.482	1.482
R(20-21)	1.101	1.101	1.1	1.1	1.097	1.097
R(20-22)	1.103	1.103	1.104	1.104	1.104	1.104
R(20-23)	1.103	1.103	1.104	1.104	1.104	1.104
A(2-1-6)	119.7	119.7	123.1	123	120.6	120.6
A(2-1-11)	124.8	115.7	122.7	113.7	124.5	115.1
A(1-2-3)	119.1	119.8	116.6	117.3	119.2	119.6
A(1-2-7)	121.6	118.8	122.4	119.3	121.3	118.7
A(6-1-11)	115.5	124.6	114.3	123.2	115	124.4
A(1-6-5)	120.3	119.6	120.1	119.3	120.1	119.6
A(1-6-10)	118.5	121.3	117.8	120.7	118.6	121.1
A(1-11-12)	115.8	115.9	117.6	117.8	118.1	118.3
A(3-2-7)	119.4	121.4	121	123.4	119.5	121.6
A(2-3-4)	122.2	121.7	122.1	121.6	121.1	121
A(2-3-8)	118.8	119.2	120.1	120.4	119.8	120.1
A(4-3-8)	119	119.1	117.8	118	119.1	118.9
A(3-4-5)	117.5	117.4	120.4	120.4	118.5	118.5
A(3-4-16)	119.2	119.1	116.9	117.7	118.2	117.9
A(5-4-16)	123.4	123.5	122.6	121.9	123.3	123.6
A(4-5-6)	121.2	121.8	117.8	118.3	120.5	120.7
A(4-5-9)	120.1	120	121.5	121.2	120.6	120.7
A(4-16-17)	115.3	115.2	117.2	117.2	117	116.9
A(4-16-18)	126.9	127	124.2	124.2	125.3	125.3
A(6-5-9)	118.6	118.2	120.8	120.5	118.9	118.7
A(5-6-10)	121.2	119.1	122.1	119.9	121.3	119.3
A(11-12-13)	110.8	110.8	110.2	110	109.7	109.7
A(11-12-14)	105.5	105.4	104.9	104.9	104.5	104.5
A(11-12-15)	110.8	110.8	110.2	110	109.7	109.7
A(13-12-14)	109.9	109.9	110.4	110.6	110.6	110.6
A(13-12-15)	109.8	109.9	110.7	110.7	111.5	111.5
A(14-12-15)	109.9	109.9	110.4	110.6	110.6	110.6
A(17-16-18)	117.8	117.8	118.6	118.7	117.8	117.8
A(16-18-19)	119.5	119.5	118.8	118.9	119.1	119.1

A(16-18-20)	123.9	123.9	123.7	123.6	124.1	124.1
A(19-18-20)	116.6	116.6	117.5	117.5	116.8	116.8
A(18-20-21)	111	111	111.4	111.3	112.7	112.6
A(18-20-22)	111	111	110.8	110.8	109.1	109.2
A(18-20-23)	111	111	110.8	110.8	109.1	109.2
A(21-20-22)	108.3	108.3	108.6	108.5	110	109.9
A(21-20-23)	108.3	108.3	108.6	108.5	110	109.9
A(22-20-23)	107	107	106.7	106.6	105.7	105.8

Table 6.4: Full ZEKE assignments of anethole-argon complex spectra.

Mode name ZEKE	*Anti*		*Syn*	
	Exp. freq.	Calculated freq	Exp. freq	calc
origin	0	0	0	0
ν_{66}	5		8	7
ν_{65}	17		19	26
$\nu_{66} + \nu_{65}$	30		30	33
ν_{64}	40		41	52
$\nu_{65} + \nu_{64}$	50		62	78
ν_{41}	111		102	
ν_{61}	130		138	
$\nu_{63} + \nu_{62}$	175		169	
ν_{62}	210		213	
ν_{40}	244		244	250
ν_{39}	317		326	327
ν_{38}	384		390	392
$\nu_{62+} \nu_{56}$	514		520	
ν_{36}	567		563	583
$\nu_{59+} \nu_{56}$			604	
ν_{35}			611	628
ν_{34}	755	855	771	760
ν_{56}			782	
ν_{33}	827		834	850